

IJCESEN

ISSN: 2149-9144

International

Journal of

Computational and

Experimental

Science and

ENgineering

Volume: 6 - Issue: 3 - 2020

ijcesen@gmail.com

Founder-Editor-in-Chief : **Prof.Dr. İskender AKKURT**

dergipark.org.tr/en/pub/ijcesen

Journal Info	
Web	dergipark.org.tr/en/pub/ijcesen
E-mail	ijcesen@gmail.com
ISSN	2149-9144
Frequency	March-July-November
Founded	2015
Journal Abbreviation	IJCESEN
Language	English-Turkish
Founder-Editor-in-Chief	
Prof.Dr. İskender AKKURT	Suleyman Demirel University-TURKEY
Editorial Board	
Prof.Dr. Mahmut DOGRU	Fırat University- TURKEY
Prof.Dr. Hüseyin FAKİR	Isparta Uygulamalı bilimler University- TURKEY
Prof.Dr. Erol YAŞAR	Mersin University- TURKEY
Prof.Dr. Osman SAĞDIÇ	Yıldız Teknik University- TURKEY
Dr. Nabi IBADOV	Warsaw University of Technology-POLAND
Prof.Dr. Sevil Cetinkaya GÜRER	Cumhuriyet University- TURKEY
Prof.Dr.Mitra DJAMAL	Institut Teknologi Bundung-INDONESIA
Prof.Dr. Mustafa TAVASLI	Uludağ University- TURKEY
Prof.Dr. Mohamed EL TOKHI	United Arab Emirates University-UAE
Dr. Nilgün DEMİR	Uludag University- TURKEY
Prof.Dr. Abdelmadjid RECIUI	M'Hamed Bougara University, ALGERIA
Dr. Zuhul ER	Istanbul Technical University- TURKEY
Prof.Dr. Dhafer ALHALAFI	De Montfort University, Leicester-UK
Dr. Ahmet BEYÇİOĞLU	Adana Bilim Teknoloji University- TURKEY
Dr. Tomasz PIOTROWSKI	Warsaw University of Technology-POLAND
Dr. Nurten Ayten UYANIK	Isparta Uygulamalı Bilimler University- TURKEY
Dr. Jolita JABLONSKIENE	Center for Physical Sciences and Tech. Lithuania
Dr. Yusuf CEYLAN	Selçuk University-TURKEY
Dr. Zakaria MAAMAR	Zayed University-UAE
Dr. Didem Derici YILDIRIM	Mersin University- TURKEY
Dr. Fengrui SUN	China University of Petroleum, Beijing, CHINA
Dr. Kadir GÜNOĞLU	Isparta Uygulamalı Bilimler University- TURKEY
Dr. Irida MARKJA	University of Tirana-ALBANIA
Dr. Zehra Nur KULUÖZTÜRK	Bitlis Eren University- TURKEY
Dr. Meleq BAHTIJARI	University of Pristina, Kosova
Dr. Hakan AKYILDIRIM	Suleyman Demirel University- TURKEY
Dr. Mandi ORLIĆ BACHLER	Zagreb University of Applied Sciences-CROATIA
Dr. Zeynep PARLAR	Istanbul Technical University- TURKEY
Dr. Amer AL ABDEL HAMİD	Yarmouk University-JORDAN
Prof.Dr. Nezam AMİRİ	Sharif University-IRAN
Dr. M. Fatih KULUÖZTÜRK	Bitli Eren University- TURKEY
Prof.Dr. Berin SİRVANLI	Gazi University- TURKEY

Indexing/Abstracting Databases

ASOS
indeks

INDEX  COPERNICUS
INTERNATIONAL



GENERAL IMPACT FACTOR
Universal Digital Object Information

Google Scholar



 **INTERNATIONAL**
Scientific Indexing



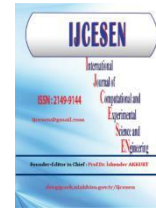
WorldCat® **ESJI** Eurasian Scientific Journal Index
www.ESJIndex.org



TOGETHER WE REACH THE GOAL

Table of Contents

Volume: 6	Issue: 3	November-2020	
Authors	Title	DOI:	Pages
Dr. Öğr. Üyesi Süleyman EKEN	Medical Data Analysis for Different Data Types	10.22399/ijcesen.780174	138-144
Uzm. Dr. Nazmiye Deniz ARSLAN, Uzm. Dr. H. Orhan KIZILKAYA, Uzm. Dr. Ayşe KUTLUHAN	Factors Affecting “Organs at Risk” Doses in 3 Dimensional Brachytherapy (3D BRT) of Cervical and Endometrium Cancers	10.22399/ijcesen.709888	145-151
Doktora Aniekan IKPE, Dr. Akanu-ibiam NDON, Dr. Promise ETİM	A Conceptual Framework for Biothermal variations in Municipal Solid Waste landfill under Mesophilic Temperature Regime	10.22399/ijcesen.737662	152-164
Doktora Ahmad ALDEEN, Dr. Yücel CAN, Prof. Dr. Murat YAZICI	Modeling Hyperelastic Materials by MATLAB	10.22399/ijcesen.662707	165-168
Prof. Dr. Fatih UCUN, Yüksek Lisans Sadun KÜÇÜK	Calculated hyperfine coupling constants of some sigma-type radicals	10.22399/ijcesen.750537	169-172
Doktora Melise KARATAY KUTMAN, Prof. Dr. Fazilet Zümrüt BİBER MÜFTÜLER, Arş. Gör. Özge KOZGUŞ GÜLDÜ, Dr. Öğr. Üyesi Coşkun HARMANŞAH	Magnetic Nanoparticles Synthesized By Green Chemistry and Investigation of Its Application in the Material Industry	10.22399/ijcesen.733423	173-175
Prof. Dr. Hatice ÖĞÜTCÜ, Yüksek Lisans Hulya AVSAR	Characterization and siderophores production of Rhizobium spp. isolated from wild legumes	10.22399/ijcesen.718084	176-179
Doç. Dr. Emre TİMUR, Prof. Dr. Coşkun SARI	Determination of Liquefaction Resistance and Allowable Bearing Capacity of Soils Based on VS (Shear wave) velocity; Case Study: Isparta Süleyman Demirel Industrial Region Waste Treatment Facility	10.22399/ijcesen.744183	180-188
Yüksek Lisans Akın ARAS, Dr. Öğr. Üyesi Murat AYAZ, Prof. Dr. Engin ÖZDEMİR, Prof. Dr. Nurettin ABUT	Virtual Reality Applications in Industrial Automation Systems: Industrial Robot Station Application	10.22399/ijcesen.764365	189-194
Anarbay KUDAYKULOV	Power Research Technique of A Thermomechanical Condition of A Rod Of Restricted Length, Variable Section At Influence Of Heterogeneous Types Of Sources Of Heat	10.22399/ijcesen.539656	195-204



Medical Data Analysis for Different Data Types

Süleyman EKEN*

Kocaeli University, Technology Faculty, Department of Information Systems Engineering, 41001, Kocaeli-Turkey

* Corresponding Author : suleyman.eken@kocaeli.edu.tr

ORCID: 0000-0001-9488-908X

Article Info:

DOI: 10.22399/ijcesen.780174

Received : 13 August 2020

Accepted : 17 September 2020

Keywords

Medical data informatics
Electronic health records
Data science
EDA
Reproducible research

Abstract:

Many discoveries and decisions in science are now being made on the basis of analyzing datasets. To gain useful information from raw medical data, data analytic uses insights to benefit the entire lifecycle of medical data. In this paper, medical data analysis notebooks are presented for collaborative and reproducible research. They provide a broad and practical introduction to medical data analysis with different data types such as images and texts. We aim to provide Jupyter notebooks to help those new to the medical data analysis field. Three exploratory coding activities including different data types are introduced: (i) Building, evaluating and interpreting deep learning models with EHR data, (ii) 2D mammogram medical imaging data analysis using CNNs for dense breasts classification, and (iii) Label recognition in radiology reports. Jupyter notebooks are useful for learning how to analyze different medical datasets and identify patterns that will improve any hospitals' and clinicians' computer-aided medical decision-making process. Leveraging advances in exploratory data analysis in healthcare requires collaboration between clinicians and data scientists

1. Introduction

In recent years, the rise in the use of social media and digitalization of social and economic activity was the source of unprecedented amounts of data, mostly in an unstructured form: weblogs, videos, speech recordings, photographs, e-mails, tweets [1, 2]. This data can be analysed to extract relevant and insightful information on business or society, and that is thanks to big data analysis tools and techniques.

This is why we believe that big data analysis and related technologies deep learning, cloud computing and scalable machine learning are a cornerstone to a medical data analysts. That being said, in addition to the benefits it offers, big data comes with many hurdles as well: (i) With continuously increasing interest from different sectors, there is also an increasing demand for skilled data experts, with colleges unable to satisfy that need, nor to incorporate big data within themselves causing millions of students to miss on such an opportunity. (ii) The available machines

can not keep up with the rate at which data is generated leading to crashes and lower quality of the analysis. And that, in turn, creates a need for more scalable systems to store and process data. (iii) The sheer size of data in itself makes it prone to mistakes and data loss, for example, think of an average establishment trying keeping records of all its thousands of students across several categories. (iv) Data safety and integrity becomes a paramount worry to both authorities and institutions. The existing security protocols are not developed with big data in mind making them unfit for it, and the nature of the data and its continuous updating make it neither easy nor cheap to manage.

With these difficulties in mind, we develop an exploratory medical data analysis notebooks, aiming at familiarizing them with the key technologies employed to store, manipulate and analyze medical data. In this work, we cover the basic tools for statistical analysis, the Python programming language, and various machine learning algorithms.

2. Material and Methods

Computational notebooks are an open-source interactive web-based application streamlining and simplifying literate programming [3, 4]. Initially, Jupyter notebooks supported only Python. Then it extended the support to different programming languages via Jupyter kernels. Notebooks combine text, code, and visualization in a single JSON document. It is parsed and displayed in a human-friendly format. The code is split into logical sections named “code cells”. So, they can be executed interactively. Another worth noting benefit of running individual code chunks is that one can choose to run some parts only once while others can be repeatedly executed. Many researchers and data analysts are rapidly adopting this new medium.

2.1. Python for Data Analysis & Visualization

Pandas is one of the most popular Python libraries that provide high-performance, easy-to-use data structures and data analysis tools [5]. Using Pandas, researchers can handle of missing data, align data automatically or explicitly, perform group-by operations, convert differently-indexed data into DataFrame objects, perform slicing, indexing, and subset of large data sets, merge and join data sets, and reshaped and pivoted of data sets. Also, Python has several visualization libraries, namely Matplotlib [6], Seaborn [7], and Folium [8] for presenting data visually.

2.2. Python for Machine Learning

Python has machine learning library named scikit-learn [9]. It has many learning algorithms such as supervised (regression, classification) and unsupervised (clustering) models. Researchers can analyze the performance of the model using different metrics and deploy methods to select between models. Also it enables users to engineer the right features for a given problem on any dataset.

2.3. Unstructured Data Analysis

We first need to understand what we are dealing with. At this point, we can divide the data structures into three main categories: structured, semi-structured and unstructured data. Any data that we can store, process and access in a relational and meaningful way can be classified as structured data. The data are stored in a relational and clean way in databases. The structure of the data and its relationship with each other is known. As an example of structured data, we can consider the

data that e-commerce sites, applications and businesses produce and store in their daily operations. Data that has no relation to each other, is unprocessed and does not have a structure or format can be called unstructured data. The data size is large and it is not easy to make the data meaningful and structured. The data can include a mix of text files, videos and images. We can describe semi-structured as a combination of structural and non-structural data. If the data can be associated and easily processed but not configured, it can be classified as a file, not on a system, or semi-structured data if on a service. Semi-structured data includes data that contains structured data properties but is not stored in traditional databases. Examples of semi-structured data are XML, text and web services [10]. Python Natural Language Toolkit (NLTK) [11] is mostly used for processing and handling text and Scikit-learn [13] includes machine learning applications so it can be used all areas where machine learning can be applied.

3. Coding Activities

This section introduces the three exploratory coding activities. Traditionally, an educational setting had a well-defined learning domain, with students as users at the receiving end, while the domain experts and teachers guide them through the learning process with the help of suitable technology prepared by them. Following sub-sections include a brief description of the laboratories.

3.1. Setup Data Analysis Environment

Here are instructions for getting their system ready to follow along with the core tools and libraries we use: Python has become the go-to programming language for data science and machine learning. So, the first step is installing Python. Anaconda is a data science distribution for Python and R. It is also a package manager and it will also help us to create environment for data science. Also, Anaconda is the recommended way to install Jupyter (IPython) Notebooks [4]. Jupyter Notebook is the interactive environment where you will be writing all your code, creating files and doing visualizations as well. Anaconda comes with a lot of required data science packages pre-installed. A new virtual environment (medical_data_analysis) is created and all the required packages are installed. After activating virtual environment, some Python packages are installed for data science which are most frequently required for other exploratory coding activities: aequitas [12], sqlite3, ipython-sql, numpy, pandas, matplotlib, seaborn, plotly, scipy, scikit-learn,

scikit-image, tensorflow, nltk, transformers, and gensim.

3.2. Building, Evaluating and Interpreting Models with EHR Data

This sub-section include interesting tools to work with EHR (Electronic Health Record) data in artificial intelligence. Firstly, we get hands-on with using Tensorflow DenseFeatures for building a simple regression model. Next, we first review some common evaluation metrics for EHR models and then learn to implement brier scores for model evaluation. Then, we conduct a demographic bias analysis and become familiar with a framework out of the University of Chicago called Aequitas [13]. We use this Aequitas for group bias and fairness disparity analysis.

In this part, we focus on just building a simple Tensorflow regression model with TF DenseFeatures on Heart Disease Data Set to predict resting blood pressure (trestbps field in the dataset). Tensorflow DenseFeatures, combining features, like those from the TensorFlow Feature Columns API, into a dense representation for the model. We can only use certain TF Feature Columns with DenseFeatures: numeric, embedding, bucketized, and indicator columns. We use the Sequential API. Replacing unknown values to NaN, dataset concatenation, dropping missing values, and selecting important features are implemented in pre-processing step. After this step, the first five columns of data are as shown in Table 1.

Table 1. An overview from data

sex	age	trestbps	thalach
male	32.0	95	127
male	34.0	115	154
male	36.0	110	125
female	38.0	105	166
female	38.0	110	156

Tensorflow feature columns can be combined into a list that can be passed to the DenseFeatures layer. Then, we add this 'dense_feature_layer' as the first layer to the model and this will handle the combining of feature inputs to the model.

The dataset was randomly divided into two independent datasets with 80% and 20% for training and testing, respectively. The batch size, epoch number, and root mean square error propability are 128, 1000, and 0.001 respectively. We evaluate the success/failure of model in terms of two measures such as Mean Absolute Error (MAE) and Mean Squared Error (MSE). Their values are 14.76 and 339.49, respectively. Table 2

shows the converted regression problem to binary classification problem. Here, score is 1 if predicted resting blood pressure is higher than 130. Also, label value is the the truth value. It consists 5 of 46 test samples. Table 3 shows performance results of binary classification.

Table 2. Five test samples of binary classification

pred	actual_value	score	Label_value
139.877350	95.0	1	0
132.572052	115.0	1	0
139.877350	170.0	1	1
132.572052	160.0	1	1
126.265846	140.0	0	1

It is important to note that bias within models can restrict or limit patient access to key medical benefits from government aid programs. Programs using machine learning algorithms to help automate approvals of key government benefits are becoming more commonplace. However, it is just as important to consider how bias can unintentionally occur. Another reason that you want to consider bias in models is that in order to create better treatments for patients we need to find better ways to select and recruit patients that represent the wider population that a drug/treatment would be targeted for.

Table 3. Performance results of binary classification

	precision	recall	f1-score	support
0	0.22	0.21	0.22	19
1	0.46	0.48	0.47	27
accuracy			0.37	46
macro avg	0.34	0.35	0.34	46
weighted avg	0.36	0.37	0.37	46

In many cases, there may be systemic biases for key groups and while this cannot always be prevented, bringing awareness of limitations and biases can give a more accurate picture of a treatment's effectiveness across different demographics. Unintended bias that is not intentional and often is not even apparent to the creator of a model and it represents the unconscious or unintentional biases that come with the artificial intelligence models. Demographic Group Bias Analysis includes selecting groups to be analyzed, preparing data, and analyzing different metrics with the groups. Here, 'score' and 'label_value' fields are used for boilerplate preprocessing input data. After this step, Table 4 shows summarized metric view for group counts and absolute ones. Opening forms of abbreviations in Table 4 are as following: tpr: true positive rate, tnr: true negative rate for :

Table 4. Summarized metric view

attribute_name	attribute_value	tpr	tnr	for	fdr	fpr	fnr	npv	precision	ppr	pprev	prev
pred	126.82-128.04	0.0	1.00	0.67	NaN	0.00	1.0	0.33	NaN	0.00	0.00	0.67
pred	128.04-134.04	1.0	0.00	NaN	0.50	1.00	0.0	NaN	0.50	0.57	1.00	0.50
pred	136.34-141.51	1.0	0.00	NaN	0.42	1.00	0.0	NaN	0.58	0.43	1.00	0.58
actual_value	120.00-134.00	0.4	0.33	0.60	0.67	0.67	0.6	0.40	0.33	0.21	0.55	0.45
actual_value	134.00-141.50	0.7	NaN	1.00	0.00	NaN	0.3	0.00	1.00	0.25	0.70	1.00
actual_value	141.50-178.00	0.5	NaN	1.00	0.00	NaN	0.5	0.00	1.00	0.21	0.50	1.00
actual_value	95.00-120.00	NaN	0.31	0.00	1.00	0.69	NaN	1.00	0.00	0.32	0.69	0.00

false omission rate, fdr: false discovery rate, fpr: false positive rate, fnr: false negative rate, npv: negative predictive value, ppr: predictive positive ratio. Figure 1 illustrates the all group metrics. Reference group information is as following: 'pred': '126.82-128.04', 'actual_value': '134.00-141.50'. Figure 2(a) shows false positive rate disparity for actual_value field. Figure 2(b) shows true positive rate disparity for pred field. Preds valued between 128.04-134.04 and 136.34-141.51 are over 10x more likely to be truly identified than reference group (preds valued

between 126.82-128.04). Figure 3 shows FPR fairness. Red bars mean false/not fair determination.

3.3. 2D Medical Imaging Data Analysis

Different clinical imaging tools are available. X-rays, computed tomography (CT), magnetic resonance imaging (MRI), and ultrasound are such technologies. X-rays down at the body from a single direction to capture a single image.

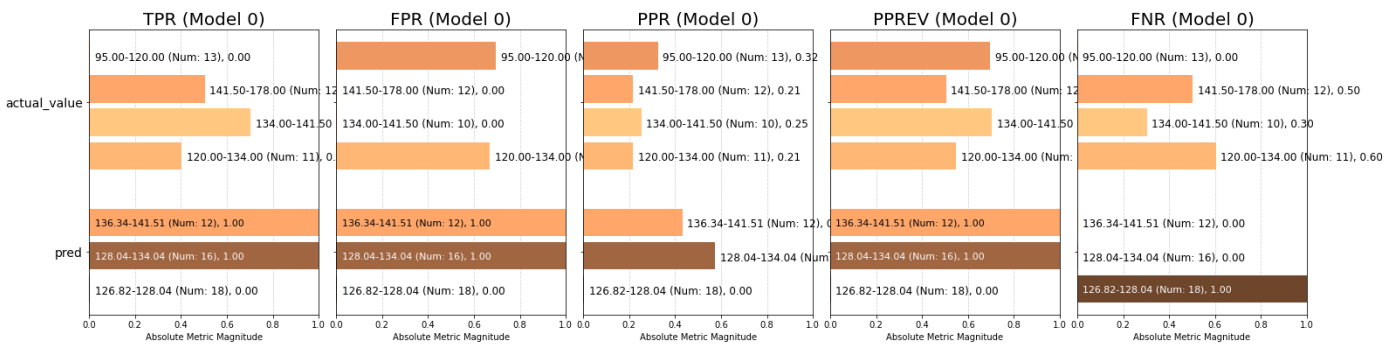


Figure 1. All group metrics plot

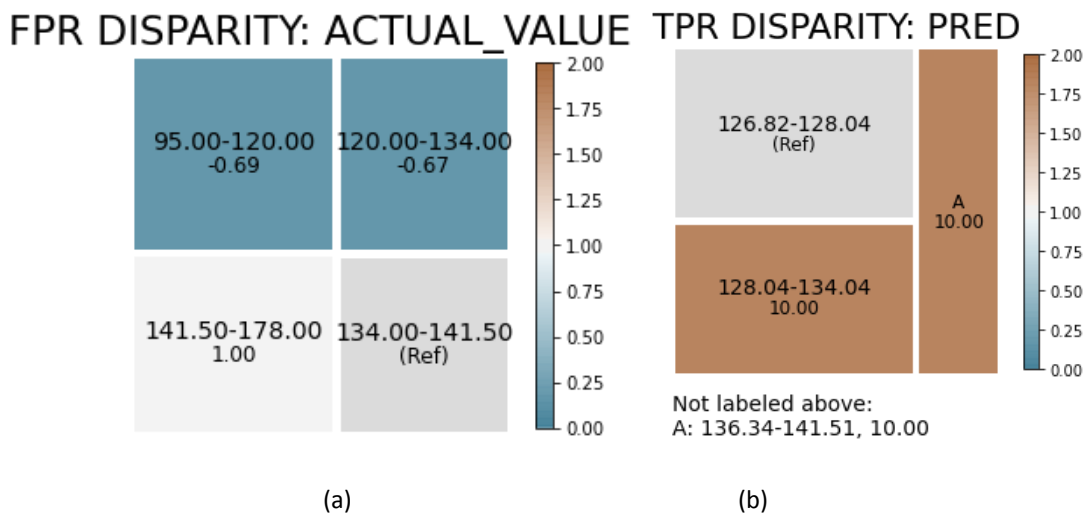


Figure 2. FPR and TPR disparity for different attributes

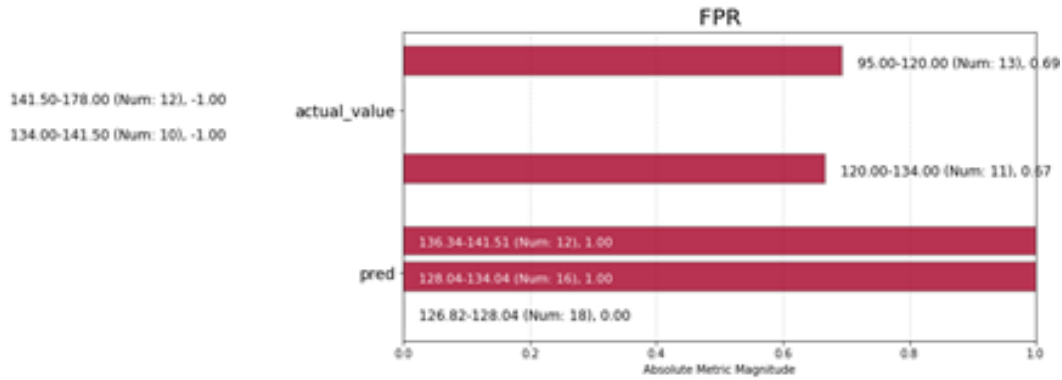


Figure 3. FPR fairness plot

CT uses x-ray, but they emit x-rays from many different angles around the human body to capture more detail from more different angles. MRI uses strong magnetic fields and radio waves to create images of areas of the body from all different angles. Ultrasound utilizes high-frequency sound waves beyond the audible limit of human hearing to generate images. Out of these different

imaging tools, x-ray and ultrasound are the only 2D imaging tool. Every imaging center and hospital have a Picture Archiving and Communication System (PACS). These systems allow for all medical imaging to be stored in the hospital's servers and transferred to different departments throughout the hospital. Classification, segmentation [14], and localization [15] the most important types of 2D imaging algorithms. A mammogram shows how dense breasts are. Women with dense breasts have a higher risk of getting breast cancer. In this part, we classify mammogram images into two classes: dense and fatty. Firstly, some preprocessing steps such as removing potential noise from images (e.g. background extraction), normalization (zero-mean, standardization), image augmentation, and resizing imaged for CNN architecture's required input. Here, image augmentation includes horizontal flip, height shift and width shift, rotation, shearing and zooming. After augmentation step, Figure 4 shows some examples of our augmented training data. We use VGG16 model [16] with pre-trained ImageNet weights. Then, fine-tuning is implemented. Layers types and other parameters of used model is given in Figure 5. Optimizer, loss function, learning rate, and epoch number are Adam(lr=1e-4), binary crossentropy, binary accuracy, and 10 respectively. Binary accuracy of the model is 0.66.

3.4. Label Recognition in Radiology Reports

In this part, we extract disease labels information

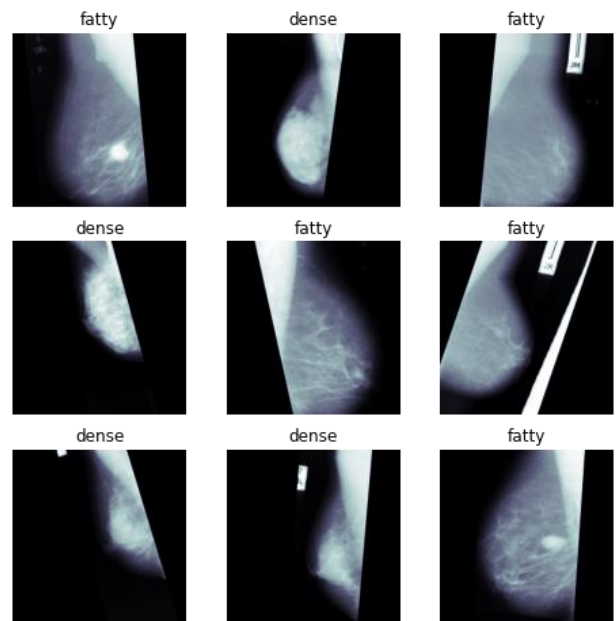


Figure 4. Manipulated data prior to training

from unstructured medical text (clinical reports) for patients [17]. We use Stanford report test document. It consists of 1,000 X-ray reports that have been manually labeled by a board certified radiologist for the presence or lack of presence of different pathologies (see Figure 6 for an example report). Figure 7 shows the first five rows of dataset. To label dataset is to search for presence of different keywords in the impression text. A list of relevant keywords for each pathology is prepared for detecting the presence of each label. For instance, related keywords for airspace opacity are: opaci, decreased translucency, increased density, airspace disease, air-space disease, air space disease, infiltrate, infiltration, interstitial marking, interstitial pattern, interstitial lung, reticular pattern, reticular marking, reticulation, parenchymal scarring, peribronchial thickening, wall thickening, scar.

Layer (type)	Output Shape	Param #
model_1 (Model)	(None, 7, 7, 512)	14714688
flatten_1 (Flatten)	(None, 25088)	0
dropout_1 (Dropout)	(None, 25088)	0
dense_1 (Dense)	(None, 1024)	25691136
dropout_2 (Dropout)	(None, 1024)	0
dense_2 (Dense)	(None, 512)	524800
dropout_3 (Dropout)	(None, 512)	0
dense_3 (Dense)	(None, 256)	131328
dense_4 (Dense)	(None, 1)	257

Total params: 41,062,209
 Trainable params: 28,707,329
 Non-trainable params: 12,354,880

Figure 5. Used CNN model architecture

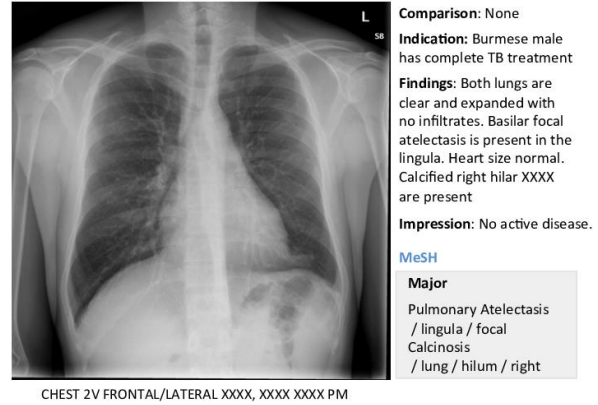


Figure 6. An example of clinical report from dataset

	Report Impression	Cardiomegaly	Lung Lesion	Airspace Opacity	Edema	Consolidation	Pneumonia	Atelectasis	Pneumothorax	Pleural Effusion	Pleural Other	Fracture
0	\n\n1.mild pulmonary edema, and cardiomegaly....	True	False	False	True	False	False	True	False	True	False	False
1	\n\n1.unremarkable cardiomeastinal silhouet...	False	False	True	False	False	False	False	False	False	False	True
2	\n1. lines and tubes are unchanged in position...	False	False	True	False	False	False	False	False	False	False	False
3	\n1. postoperative portable film with a right-...	False	False	True	True	False	False	True	True	False	False	False
4	\n\n1.single frontal view of the chest demons...	False	False	True	False	False	False	False	False	True	False	False

Figure 7. Samples from unstructured clinical reports

For impression texts, all label can be retrieved. For impression text of “Diffuse Reticular Pattern, which can be seen with an atypical infection or chronic fibrotic change. no Focal Consolidation.”, retrieved labels are Airspace Opacity, Consolidation, and Pneumonia. Performance of labeler can be evaluated with F1-score metric regarding retrieved and expected labels. Table 5 shows the labeler performance. Using some preprocessing operations such as converting pattern such as "and/or" to "or", replacing repeated whitespace with just one space, and removing redundant punctuation, performance can be improved. Also, negative mentions and dependency parsing can be used to improve the performance of labeler.

Table 5. Samples from unstructured clinical reports

Label	F1-score
Cardiomegaly	0.718
Lung Lesion	0.641
Airspace Opacity	0.923
Edema	0.708
Consolidation	0.270
Pneumonia	0.369
Atelectasis	0.646

4. Discussions

4.1. Study Limitations

Our study has several limitations. There are many types of medical imaging technologies. First, we use only mammogram images in example of 2D imaging data process. Maybe, other 2D medical images or 3D images can be used to extend this study. Second, we present three reproducible notebook activities. We aim to encourage new to the field begin their informatics projects. We plan to make more collaboration with clinicians, radiologist, pathologists, and biomedical engineering about medical diagnosis, prognosis, and treatment activities.

4.2. Study Significance

Working in multidisciplinary teams is a long championed concept to address challenges such as diabetic retinopathy, skin cancer detection from images, smoking status and medication identification from unstructured patient records for artificial intelligence research, and to increase its impact in medicine. In this context, we present three different activities with this study. As a results, multidisciplinary teams can set clear vision

for collaborative and reproducible research, create clear data inclusion and exclusion criteria for initial data draw, and insight for what natural language processing/machine learning methods might be better at addressing different clinical problems.

5. Conclusion

Exploratory notebooks specifically focused on the medical data analysis have been presented in this paper. We firstly give theoretical background information about medical data analysis using different environments/structures such as spreadsheets, SQLite, and Python based. Then, three exploratory coding activities are presented. The first one focuses on EHR data analysis using Python wrangling skills and deep learning models. The second one focuses on image processing based medical data analysis. The last one is unstructured data analysis on clinical reports. As a result, we aim to help those new to the field begin their informatics projects.

Also, we will be taking into account the clinical and industry stakeholders' requirements while presenting the notebooks. These requirements can be listed as: innovative medical data analysis applications for different purposes with different types of input, methods for pattern analysis, supporting for big data platforms that offer distributed run environments.

References

- [1] Aggarwal, A. K. (2019). Opportunities and challenges of big data in public sector. In *Web services: Concepts, methodologies, tools, and applications* (pp. 1749-1761). IGI Global. doi: 10.4018/978-1-4666-9649-5.ch016
- [2] Oussous, A., Benjelloun, F. Z., Lahcen, A. A., & Belfkih, S. (2018). Big Data technologies: A survey. *Journal of King Saud University-Computer and Information Sciences*, 30(4), 431-448. doi: 10.1016/j.jksuci.2017.06.001
- [3] Shen, H. (2014). Interactive notebooks: Sharing the code. *Nature*, 515(7525), 151-152. doi: 10.1038/515151a
- [4] Kluyver, T., Ragan-Kelley, B., Pérez, F., Granger, B. E., Bussonnier, M., Frederic, J., ... & Ivanov, P. (2016, May). Jupyter Notebooks-a publishing format for reproducible computational workflows. In *ELPUB* (pp. 87-90). doi:10.3233/978-1-61499-649-1-87
- [5] McKinney, W. (2011). pandas: a foundational Python library for data analysis and statistics. *Python for High Performance and Scientific Computing*, 14(9). doi:
- [6] Hunter, J. D. (2007). Matplotlib: A 2D graphics environment. *Computing In Science Engineering* 9, 3. 90-95. doi: 10.1109/MCSE.2007.55
- [7] Embarak, O. (2018). Data Visualization. In *Data Analysis and Visualization Using Python* (pp. 293-342). Apress, Berkeley, CA. 10.1007/978-1-4842-4109-7_7
- [8] Cuttone, A., Lehmann, S., & Larsen, J. E. (2016). geoplolib: a Python Toolbox for Visualizing Geographical Data. arXiv preprint arXiv:1608.01933.
- [9] Pedregosa, F., Varoquaux, G., Gramfort, A., Michel, V., Thirion, B., Grisel, O., ... & Vanderplas, J. (2011). Scikit-learn: Machine learning in Python. *the Journal of machine Learning research*, 12, 2825-2830.
- [10] Leung, C. K. S. (2019). Big data analysis and mining. In *Advanced Methodologies and Technologies in Network Architecture, Mobile Computing, and Data Analytics* (pp. 15-27). IGI Global. doi: 10.4018/978-1-5225-2255-3.CH030
- [11] Loper, E., & Bird, S. (2002). NLTK: the natural language toolkit. arXiv preprint cs/0205028.
- [12] Saleiro, P., Kuester, B., Hinkson, L., London, J., Stevens, A., Anisfeld, A., ... & Ghani, R. (2018). Aequitas: A bias and fairness audit toolkit. arXiv preprint arXiv:1811.05577.
- [13] Detrano, R., Janosi, A., Steinbrunn, W., Pfisterer, M., Schmid, J. J., Sandhu, S., ... & Froelicher, V. (1989). International application of a new probability algorithm for the diagnosis of coronary artery disease. *The American journal of cardiology*, 64(5), 304-310. doi: 10.1016/0002-9149(89)90524-9
- [14] Strzelecki, M., Szczypinski, P., Materka, A., & Klepaczko, A. (2013). A software tool for automatic classification and segmentation of 2D/3D medical images. *Nuclear Instruments and Methods in Physics Research Section A: Accelerators, Spectrometers, Detectors and Associated Equipment*, 702, 137-140. doi: 10.1016/j.nima.2012.09.006
- [15] de Vos, B. D., Wolterink, J. M., de Jong, P. A., Viergever, M. A., & Išgum, I. (2016, March). 2D image classification for 3D anatomy localization: employing deep convolutional neural networks. In *Medical imaging 2016: Image processing* (Vol. 9784, p. 97841Y). International Society for Optics and Photonics. doi: 10.1117/12.2216971
- [16] Simonyan, K., & Zisserman, A. (2014). Very deep convolutional networks for large-scale image recognition. arXiv preprint arXiv:1409.1556.
- [17] Irvin, J., Rajpurkar, P., Ko, M., Yu, Y., Ciurea-Ilicus, S., Chute, C., ... & Seekins, J. (2019, July). Chexpert: A large chest radiograph dataset with uncertainty labels and expert comparison. In *Proceedings of the AAAI Conference on Artificial Intelligence* (Vol. 33, pp. 590-597). 10.1609/aaai.v33i01.3301590



Factors Affecting “Organs at Risk” Doses in 3 Dimensional Brachytherapy (3D BRT) of Cervical and Endometrium Cancers

Nazmiye Deniz ARSLAN^{1*}, Hazım Orhan KIZILKAYA², Ayşe KUTLUHAN DOĞAN¹

¹Health Sciences Üniversity, Yedikule Chest Diseases And Chest Surgery Training And Research Hospital, Radiation Oncology, 34020, İstanbul-Turkey

²Health Sciences Üniversity, Şişli Hamidiye Etfal Training And Research Hospital, Radiation Oncology, 34360, İstanbul-Turkey

* Corresponding Author: denizsaracoglu@hotmail.com

ORCID: 0000-0003-0080-2284

Article Info:

DOI: 10.22399/ijcesen.799808

Received : 29 September 2020

Accepted : 26 October 2020

Keywords:

Brachytherapy
volume of bladder
cervix cancer
endometrial cancer

Abstract:

In brachytherapy, both the tumor and organ at risk may have intrafractional and interfractional anatomical differences. In this study, we aimed to investigate the factors affecting Organs at Risk (OAR) doses in adaptive 3D BRT applications. A total of 55 patients that underwent intracavitary brachytherapy with the diagnosis of a gynecological tumor between September 2012 and December 2013 were evaluated retrospectively. The effect of the surgery, applicator type, bladder, rectum and sigmoid on D_{2cc} , D_{1cc} , $D_{0.1cc}$ values were investigated. The median age was 55 years. While there was no statistically significant difference between 1st and 2nd fractions measurements, the sigmoid D_{1cc} values between the 1st and 3rd fractions were found to be statistically significant ($p = 0.004$). When the effect of the interfractional change of bladder filling on OAR doses in the first three fractions was examined, it was not statistically significant however, its effect on bladder, sigmoid and rectum D_{2cc} , D_{1cc} , $D_{0.1cc}$ values were observed in some fractions. The bladder point dose was found to be statistically significant in operated patients ($p = 0.005$). When the comparison was made according to the application type, the bladder dose was found to be statistically significant in roller applications than the other two applicator treatments ($p = 0.001$). 3D BRT provides maximum protection of healthy tissues while giving a high dose to the target as a result of adaptive planning by performing computed tomography in each fraction. The sigmoid is the OAR that makes the most distinctive interfraction. To obtain higher treatment accuracy in each fraction, routine preparation and tomographic imaging followed by adaptive planning should be done.

1. Introduction and Purpose

According to GLOBOCAN 2020 data, amongst gynecologic cancers, endometrial cancers are the most common in developed countries and cervical cancers are the most common. Following these, endometrial cancers are the second most common cancer type [1]. In our country, endometrium cancer is the most common. Although the primary treatment is surgery in endometrial cancers, Intracavitary Brachytherapy is also one of the most important complementary steps of treatment, especially in the early stages. In cervical cancers, early-stage surgery is at the forefront however, radiotherapy is the first option in advanced stage [1, 2, 3] cancers.

Intracavitary Brachytherapy, alone or together with External Radiotherapy, increases local control in both cancers [2, 4, 5]. Bladder, sigmoid and rectum toxicity rates, which are known as organs at risk in these patients, are proportional to the total doses received from External RT ± Brachytherapy. Chronic cystitis, fibrosis, and vesicovaginal fistulas might occur in the bladder, and proctitis and fistulas might occur in the rectum. It was reported that with radiotherapy, mild bladder complications were between 8-12% and serious bladder complications were between 2-6% [3]. Knowing the factors that are effective in Organs at Risk (OAR) doses allows us to predict the risk of complications, and make necessary changes in planning. In many centers, 3D

High-Dose Rapid (3D HDR) Brachytherapy is applied by using Computed Tomography (CT) in the first fraction (fr) however, treatment is applied in following fractions with the same plan as conventional graphics are obtained with a C-arm. In this practice, the effect of interfractional volume changes on target treatment volumes cannot be observed. Target volumes can be better determined with adaptive brachytherapy and the appropriate dose may thus be given, reducing OAR doses. Tumor regression and OAR movements might change the applicator placement and angle. In this case, Adaptive Intracavitary Brachytherapy is recommended with imaging in each application to see the shrinkage of the tumor and determine the exact doses of OAR [4, 5]. It is possible to increase local control with an Adaptive 3D BRT, while reducing the side effects stemming from OAR doses. In the present study, clinical factors that might be effective in OAR doses in Adaptive 3D BRT applications were investigated, and the effect of these factors on dose-volume curves was examined statistically.

2. Materials & Method

Patients who were diagnosed with gynecological tumors and who underwent Intracavitary Brachytherapy between September 2012 and December 2013 were evaluated retrospectively. A total of 55 patients diagnosed with endometrium cancer, and 32 with cervical cancer were included in the study. The ages of the patients ranged between 26 and 84, and the median age was 55. The pathological diagnosis of the cervical cancer patients were squamous-cell carcinoma in 27 patients, adenoid in 4 patients, and adenoid-squamous carcinoma in 1 patient. The pathological diagnosis of the endometrial cancer patients were adenocarcinoma in 22 patients, and serous papillary carcinoma in 1 patient. A total of 21 patients with endometrium cancer underwent TAH+BSO+PELVIC LND±PA LND (2 patients were inoperable), and 9 patients with cervical cancer were operated on. Two patients with endometrial cancer were medically inoperable, 6 patients were Stage 2, 7 patients were Stage 3, and 8 patients were stage 1. A total of 9 patients with cervical cancer were Stage 1B2; and among the inoperable patients, 15 were Stage 2B, 1 was Stage 3A, and 7 were Stage 3B. All patients diagnosed with cervical cancer underwent External Pelvic RT (50.4Gy) ± Simultaneous Chemotherapy (40 mg/m²/weekly cisplatin), and only 13 of the endometrial cancer patients underwent External Pelvic RT (45-50.4Gy).

A BRT (Nucletron, Vandaal, Netherlands) was applied to the patients by using Linear Accelerator (Trilogy™; Varian Medical Systems, Palo Alto, CA, USA- Oncor™; Siemens AG, Munich, Germany) radiotherapy devices and post-Pelvic EBRT MR/CT compatible gynecological applicators. In Postop BRT applications, the upper 1/3 of the vagina was determined as the target area by using cylinder applicators suitable for the patient's vagina size. In 30 patients with postoperative gynecological tumors (21 endometrium ca + 9 cervix ca), the cylinder applicator was used, and in patients with inoperable gynecological tumors, the Adaptive 3D HDR BRT was

performed by using 22 tandem + ring applicators (22 cervix ca) and 3 cylinder + tandem applicator (2 endometrium ca + 1 cervix ca). The effects of operation presence, applicator type, OAR volumes on the D_{2 cc}, D_{1cc}, D_{0.1cc} values of the bladder, rectum and sigmoid were investigated.

Brachytherapy

The patients were informed about the application before the treatment. All abdominal MRI and gynecological examinations of each patient were performed before the BRT. In the examinations, size of the vagina, size and position of the uterus, localization, dimensions and diffusion of tumors, and the type of applicators to be used were determined. All patients were given pre-brachytherapy bowel cleansing training (Enema Application in the 12th hour and 3rd hour before the treatment). The patients were rested in the gynecological examination position at the special treatment desk. The balloon was inflated by administering a bladder probe (2-way Foley probe, Beybi®, Turkey) and 7 cc Radio-opaque Substance (Omnipaque 350 mg/mL; GE Healthcare, Little Chalfont, UK) to the patients. Then, CT/MR compliant applicators were placed and fixed, and the planning CTs were performed by administering 20 cc contrast Normal Saline (NS) to the bladder. Cylinder applicators were used for postop patients, a Ring + Tandem Applicator was used for inoperable patients, and a Cylinder + Tandem Applicators were used for only 3 patients. The endometrium lumen lengths of the patients were measured with a Hysterometer, and the appropriate tandem length was determined (min 2-max 6 cm). In postop patients, the appropriate cylinder diameter was determined according to the size of the vagina that was measured during vaginal examination (min 2-max 3.5 cm).

Planning

In each fraction, Pelvic CTs (Toshiba Alexion, 16-slice, Japan) were performed with 3mm sections in the supine position approximately 15 minutes after the applicator in the brachytherapy unit (by applying general anesthesia when necessary). The CT images were transferred to the Oncentra Treatment Planning System (TPS) (Oncentra version 4.5.3.30, Nucletron, Vandaal, Netherlands), and High-Risk Clinical Target Volume (HR CTV) and OAR (bladder, rectum and sigmoid) volumes were contoured for patients with cervical cancer. The CTV (vaginal cuff), PTV (CTV+0.5mm margin) and OAR volumes were contoured for patients with endometrium cancer in line with the rules specified in the GEC ESTOAR and ICRU 38 report. The HR CTV, PTV, bladder D_{2 cc} (the dose taken as maximum 2 cm³ of the tissue volume), D_{1cc}, D_{0.1cc} values, rectum D_{2 cc}, D_{1cc}, D_{0.1cc} values, and sigmoid D_{2 cc}, D_{1cc}, D_{0.1cc} values were calculated, and the bladder fullness was recorded in cc.

Treatment

According to the recommendations of the American Brachytherapy Society (ABS), the number and dose of the fractions were determined based on the condition of external radiotherapy and operation status of the patients.

After the treatment doses and the appropriate treatment plans were determined, the patients were treated with Ir-192 after loading HDR BRT (Nucletron, Vandaag, Netherlands) (10 Ci source activities) twice a week. In postop patients, the 5-mm depth of the vaginal mucosa was determined as the PTV target tissue. The distribution of bladder volumes were examined, and bladder fullness values were divided into 3 groups as <90 cc, 90-110 cc, and >110 cc. For HR-CTV, D₉₀ (HR-CTV's minimum dose taken by %90) and for organs at risk the D_{2cc,1cc,0.1cc} were calculated. Physical doses were converted to the EQD2 Linear Quadratic Model that was $a/\beta = 10$ Gy for HR-CTV, and $A/\beta = 3$ Gy for OARs. The planning target was EQD2 D₉₀ ≥85 Gy (total dose EBRT + BT) for HR-CTV. For OARs, the D_{2cc} values were EQD2 90 Gy for the bladder, and EQD2 75 Gy for the rectum and sigmoid. The Fr count and dose of the patients were calculated by taking into account these values.

Statistics

The SPSS (Version 17.0; SPSS Inc., Chicago, IL) program was used in the statistical analysis of the data. The categorical measurements were summarized as numbers and percentages, and continuous measurements were summarized as mean and standard deviation (median and min-max when needed). The dosimetric analyses were made separately for each application method and doses were compared among the three application methods. For the evaluation of the data according to the application types, the Kruskal Wallis Test and Mann Whitney U-test were used (cylinder and tandem ring comparison), and the Mann Whitney U-test was used to analyze the effect of the operation presence. The difference between the basal values and other measurements was evaluated with the Wilcoxon Test. The statistical significance level was taken as p=0.05 in all tests.

N.B.: This study was presented in March 2014 as a dissertation under the same name.

3. Results

The median age was 55 years (min:26 - max:84). A total of 23 of the patients had endometrium cancer (22 adenoma, 1 serous papillary ca) and 32 had cervix cancer (27 squamous hc, 4 adenoma, 1 adenosquamous ca). The bladder, sigmoid and rectum D_{2cc}, D_{1cc}, D_{0.1cc} values had interfractional changes, in other words, the measurements were in basal values. When the 2nd and 3rd fractions of the 55 patients who were diagnosed with cervical and endometrium cancer were compared, significant differences were detected only in sigmoid 1st and 3rd fr D_{2cc}, D_{1cc}, D_{0.1cc}. Although there were no statistically significant differences between the 1st fr and 2nd fr measurements, the Sigmoid D_{1cc}, D_{1cc} values between the 1st and 3rd fractions were found to be statistically significant (p=0.004). Although Sigmoid 1.frc D_{1cc} was 482.2cGy (122.5-946 cGy), Sigmoid 3.frc was found to be D_{1cc} 395cGy (82.0-812.5cGy). An

interfractional decrease was found to be statistically significant(Table 1).

Table 1: Comparison of basal and other measurement values

OAR D _{1cc} and D _{0.1cc} 1.frc and 2. and 3.frc values	p
rectum 1cc1frc - r1cc2frc	0.319
rectum 1cc1frc - r1cc3frc	0.346
bladder1cc1frc - m1cc2frc	0.645
bladder1cc1frc - m1cc3frc	0.332
sigmoid 1cc1frc - s1cc2frc	0.573
sigmoid 1cc1frc - s1cc3frc	0.004
rektum0.1cc1frc - r0.1cc2frc	0.140
rektum0.1cc1frc - r0.1cc3frc	0.080
bladder0.1cc1frc - m0.1cc2frc	0.538
bladder0.1cc1frc - m0.1cc3frc	0.465
sigmoid0.1cc1frc - s0.1cc2frc	0.101
sigmoid0.1cc1frc - s0.1cc3frc	0.002

P= < 0,05

29 of the 55 patients were treated with 3 frc, 26 were treated with 4 frc. It was aimed that the frc count was increased to 4 and the dose of the OAR per fraction was reduced for 23 inoperable patients with cervical cancer, 2 inoperable endometrium cancer patients, and 1 operable endometrium cancer patient to optimize the OAR tolerance doses. The patients were divided into 3 groups according to bladder volumes as <90 cc, 90-110 cc, and >110 cc (Table 2).

Table 2: Distribution of Bladder Fullness Rate according to Bladder Volumes

	Number	% Rate
Bladder full. 1.frc		
≤90	15	27.3
90-110	20	36.4
>110	20	36.4
Bladder full. 2.frc		
≤90	17	30.9
90-110	16	29.1
>110	22	40.0
Bladder full. 3frc		
≤90	11	20.0
90-110	17	30.9
>110	27	49.1
Bladder full. 4frc		
≤90	3	11.5
90-110	9	34.6
>110	14	53.8

When the effect of interfractional change of bladder fullness on OAR doses in the first 3 fractions were

examined, there were effects on the bladder, sigmoid and rectum D_{2cc} , D_{1cc} , $D_{0.1cc}$; however, these effects were not at statistically significant levels (Table 3).

Table 3: Effect of Bladder Fullness on OAR Doses in all Fractions

Bladder fullness (cc) 1.frc	≤90		90-110		>110		p
	n	Mean (Min-Max)	n	Mean (Min-Max)	n	Mean (Min-Max)	
(cGy)							
rectum2cc 1.frc	15	361(134-555)	20	384(72-519)	20	383(226-562)	0.594
mesane2cc 1.frc	15	351(246-593)	20	404(331-602)	20	447(305-681)	0.026
sigmoid 2 cc 1.frc	15	279(92-495)	20	264(104-582)	20	314(156-525)	0.464
rectum 1cc 1.frc	15	403(147-602)	19	412(292-561)	19	427(247-620)	0.398
mesane 1cc 1.frc	15	384(273-613)	19	436(360-654)	19	468(330-743)	0.045
sigmoid 1cc 1.frc	15	269(97-625)	20	405(115-648)	20	337(113-588)	0.551
rektum0.1cc 1.frc	15	501(177-760)	19	502(368-676)	19	500(294-822)	0.669
mesane0.1cc 1.frc	15	484(242-1096)	19	521(420-802)	19	570(381-1461)	0.279
sigmoid0.1cc 1.frc	15	422(122-946)	20	514(139-816)	19	476(147-800)	0.824
Bladder fullness (cc) 2.frc	≤90		90-110		>110		p
(cGy)	n	Mean (Min-Max)	n	Mean (Min-Max)	n	Mean (Min-Max)	
rectum2cc 2.frc	7	365(252-483)	16	369(96-553)	22	352(203-579)	0.438
mesane2cc 2.frc	7	387(307-519)	16	390(35-573)	22	460(323-643)	0.041
sigmoid 2 cc 2.frc	7	226(106-559)	16	346(150-557)	22	302(73-463)	0.271
rectum 1cc 2.frc	7	419(278-529)	16	432(149-643)	22	387(230-640)	0.968
mesane 1cc 2.frc	7	415(340-527)	16	430(340-628)	22	485(252-713)	0.233
sigmoid 1cc 2.frc	7	265(108-527)	16	401(172-637)	22	341(81-519)	0.222
rektum0.1cc 2.frc	7	496(349-632)	16	505(174-811)	22	464(294-800)	0.989
mesane0.1cc 2.frc	7	482(38)	16	567(4)	22	592(3)	0.1

Bladder fullness (cc) 3.frc	≤90		90-110		>110		p
	n	Mean (Min-Max)	n	Mean (Min-Max)	n	Mean (Min-Max)	
(cGy)							
rectum2cc 3.frc	17	343(132-456)	17	360(102-517)	27	386(44-589)	0.293
mesane2cc 3.frc	17	399(323-589)	17	435(353-569)	27	432(221-637)	0.736
sigmoid 2cc 3.frc	17	189(123-510)	17	281(91-551)	27	291(57-693)	0.282
rectum 1cc 3.frc	17	401(153-518)	17	382(190-561)	27	446(281-657)	0.055
mesane 1cc 3.frc	17	468(354-676)	17	489(386-627)	27	500(327-856)	0.801
sigmoid 1cc 3.frc	17	213(143-582)	17	333(100-545)	27	307(64-623)	0.361
rectum0.1cc 3.frc	17	481(55-665)	17	461(252-644)	27	537(365-876)	0.024
mesane0.1cc 3.frc	17	565(415-917)	17	577(456-837)	27	549(380-902)	0.569
sigmoid0.1cc 3.frc	17	281(195-812)	17	410(110-752)	27	421(82-701)	0.392

P= < 0,05

When examined according to operation presence, the bladder spot dose was found to be statistically significant in operated patients (p=0.005) (table 4). Although it was less effective on rectum doses when compared in terms of operation status, it was also observed that it increased organs at risk doses in all fractions (p<0.001) (Table 5). When compared in terms of the type of application, the bladder dose was significantly higher in cylinder applications compared to the other two applications (p=0.001) (Table 6). Today, the Intracavitary Brachytherapy application is applied according to the bone structure with BT-planning in the first fraction and with conventional graphics in the following fractions in many centers. Anatomical changes of the target and organs at risk might change the applicator placement angle, which can change the target and organs at risk doses among fractions. When Adaptive Brachytherapy is applied with the guidance of imaging, the volume definition may be made with high accuracy by seeing changes in the targets and OARs by performing CT in each fraction [6, 7, 8].

Table 4: Comparison of OAR, Volume and Fraction Variables according to Operation Presence

OAR/Vol ume/fr no (cGy)	Operation			No Operation			p
	N	Mea n±S D	Mean (Min- Max)	N	Mea n±S D	Mean (Min- Max)	
Rectum 2cc 1.frc	3 0	404. 8±7 7.8	391.6(235.2- 561.7)	2 5	348. 5±1 17.9	329.0(72.0- 549.7)	0. 03 0
Rectum 2cc 2.frc	3 0	385. 7±6 2.2	385.2(246.0- 524.0)	2 5	319. 0±1 20.6	298.0(96.0- 579.0)	0. 01 1
Rectum 2cc 3.frc	3 0	394. 9±6 3.8	384.5(258.7- 528.4)	2 5	332. 1±1 28.3	365.0(44.0- 589.0)	0. 06 2
Rectum 2cc 4.frc	1 1	408. 7±6 9.7	397.0(286.0- 521.2)	1 5	311. 0±9 5.0	314.0(93.0- 447.4)	0. 01 3
Mesane 2cc 1.frc	3 0	395. 2±6 6.1	387.4(246.0- 570.6)	2 5	464. 0±1 04.1	466.0(263.5- 681.0)	0. 00 5
Mesane 2cc 2.frc	3 0	393. 4±6 1.5	383.5(307.0- 543.0)	2 5	458. 0±8 8.0	470.0(318.5- 642.6)	0. 00 7
Mesane 2cc 3.frc	3 0	393. 6±5 6.6	387.8(298.0- 516.0)	2 5	468. 2±8 7.0	479.0(221.0- 637.1)	0. 00 01
Mesane 2cc 4.frc	1 1	395. 7±6 8.0	366.0(305.0- 516.3)	1 5	457. 8±5 1.9	467.0(350.0- 567.0)	0. 04 1
Sigmoid 2cc 1.frc	3 0	241. 7±1 00.4	246.7(92.0- 449.0)	2 5	364. 8±1 12.9	369.0(143.0- 582.0)	0. 00 01
Sigmoid 2cc 2.frc	3 0	242. 9±1 17.1	210.8(73.3- 455.0)	2 5	372. 8±1 12.5	368.0(143.0- 559.0)	0. 00 01
Sigmoid 2cc 3.frc	3 0	215. 5±1 06.4	204.1(57.4- 44.0)	2 5	372. 8±1 39.9	333.0(174.3- 693.4)	0. 00 01
Sigmoid 2cc 4.frc	1 0	178. 7±7 5.8	202.0(55.0- 277.3)	1 5	400. 9±1 09.4	393.0(206.0- 581.0)	0. 00 01

P= < 0,05

Table 5: Evaluation of the Effect of the Operation Factor on Organ at Risk Volumes

Operati on	Yes	No	p
	Med (Min-Max)	Med (Min-Max)	
rectum 1cc1frc	427.5(270.3- 610.9)	381.1(147.0- 620.5)	0.071
r1cc2frc	422.5(278.0- 579.2)	368.0(149.0- 643.0)	0.040
r1cc 3frc	437.3(290.6- 657.5)	384.0(153.0- 620.3)	0.033
r1cc 4frc	440.0(279.0- 571.2)	370.0(198.0- 555.5)	0.305
r1cc5frc	350.0(313.0- 416.0)	-	

mesane1 cc 1frc	420.7(273.0- 614.0)	493.5(301.0- 743.0)	0.010
m1cc 2frc	406.5(252.0- 616.5)	512.7(340.0- 712.6)	0.001
m1cc 3frc	436.5(327.0- 856.0)	519.0(354.0- 693.4)	0.000 1
m1cc 4frc	428.0(331.0- 558.0)	517.4(448.0- 583.0)	0.002
m1cc 5frc	387.0(310.0- 391.0)	-	
sigmoid 1cc1frc	281.8(97.5- 553.0)	427.0(154.5- 648.0)	0.001
s1cc 2frc	247.5(80.7- 504.0)	420.0(160.0- 637.4)	0.001
s1cc 3frc	240.3(64.0- 504.0)	365.0(199.0- 623.0)	0.000 1

P= < 0.05

Table 6: Evaluation of the Effect of Applicator Type on Organs at Risk Volumes

Appli cator Type	Cylinder	Tandem ring	Tandem cylinder	p	p*
	Med (Min- Max)	Med (Min- Max)	Med (Min- Max)		
rectu m 1cc1f rc	427.5(270 .3-610.9)	385.0(147 .0-620.5)	377.2(292 .0-602.3)	0.1 95	0.0 75
r1cc2 frc	422.5(278 .0-579.2)	356.5(149 .0-643.0)	368.0(283 .0-640.0)	0.1 08	0.0 36
r1cc 3frc	437.3(290 .6-657.5)	392.0(153 .0-620.3)	333.0(231 .0-518.0)	0.1 03	0.0 40
r1cc 4frc	440.0(279 .0-571.2)	370.0(198 .0-555.5)	462.5(370 .0-555.0)	0.3 73	0.2 28
r1cc5 frc	350.0(313 .0-416.0)	-	-		
mesa ne1c c 1frc	420.7(273 .0-614.0)	483.0(301 .0-743.0)	510.0(432 .7-612.6)	0.0 32	0.0 19
m1cc 2frc	406.5(252 .0-616.5)	505.4(340 .0-712.6)	527.0(463 .5-681.0)	0.0 04	0.0 05
m1cc 3frc	436.5(327 .0-856.0)	527.0(354 .0-693.4)	516.0(467 .6-676.0)	0.0 00 1	0.0 00 1
m1cc 4frc	428.0(331 .0-558.0)	517.4(448 .0-583.0)	521.5(511 .0-532.0)	0.0 12	0.0 04
m1cc 5frc	387.0(310 .0-391.0)	-	-		
sigm oid 1cc1f rc	281.8(97. 5-553.0)	420.5(154 .5-648.0)	461.0(243 .0-466.8)	0.0 05	0.0 01
s1cc 2frc	247.5(80. 7-504.0)	422.5(237 .4-637.4)	237.4(160 .0-527.0)	0.0 01	0.0 00 1
s1cc 3frc	240.3(64. 0-504.0)	378.5(239 .0-623.0)	338.3(199 .0-416.0)	0.0 00 1	0.0 00 1

P= < 0.05

4. Discussion

There are many studies in the literature examining the effect of bladder volume on OAR doses [9, 10, 11]. Studies conducted with the standard bladder filling protocol in each application reported dosimetric changes stemming from the differences in organ volumes [11, 12]. In the study conducted by Jamema et al. in which they examined the OAR dose and volume changes, they found interfractional increases only in sigmoid doses, and associated this with the treatment applied by emptying the bladder in the same way in each fraction resulting in constant bladder and rectum volumes, due to the sigmoid being a more mobile organ [13]. In the present study, bladder fullness rates did not have any significant effects on OAR doses. This result can be explained with good bowel preparation before each application and standard bladder filling protocol (20 cc contoured SF with probe). Because the distribution of bladder fullness values were examined, the median residue urine amounts measured in planning BT were similar to each other (Table 2).

GEC ESTOAR (Group European de Curietherapie-European Society for Therapeutic Radiology and Oncology) and ABS recommended the dose of 2 cc in organs at risk as the hot spot (D_{max}), and 1 cc and 0.1 cc doses as spot doses [14, 15]. There are many studies evaluating the D_{2cc} , D_{1cc} and $D_{0.1cc}$ doses of organs at risk which show that bladder fullness affects rectum and sigmoid doses [9, 16, 17, 18, 19]. In our study, the dose of 2 cc was used as D_{max} , and bladder fullness was not found to be effective on OAR D_{2cc} values. When the interfractional changes of OAR, D_{2cc} , D_{1cc} and $D_{0.1cc}$ were examined, there were significant differences only in sigmoid D_{1cc} and $D_{0.1cc}$ 1st and 3rd fractions ($p=0.004$).

During planning, there may be anatomical variations in the bladder position, and some studies showed that there were anatomical changes in the bladder after hysterectomy [20]. When the effect of the applicator type and operation factors on OAR D_{2cc} , D_{1cc} , $D_{0.1cc}$ were examined, although rectum doses were less affected, all dose values were found to be significantly higher in cylinder applications compared to tandem + ring applications because the choice of applicators in operated patients would be cylindrical. The dose distribution stemming from the shape of the applicators and the treatment of the vagina that is neighboring the bladder may have caused the OAR dose increase [12].

When the results of the studies were evaluated together, it can be seen that the bladder dose was higher in patients for whom cylinders were used, and the changes in the anatomical placements of organs at risk in operated patients contribute to this dose increase [14, 18, 19, 20].

In the present study, various factors that affected the D_{2cc} , D_{1cc} , $D_{0.1cc}$ values of the bladder, sigmoid and rectum. The operation status and the applicator type of the patients affected OAR doses, and bladder fullness had no statistically significant effect on organs at risk. It was also observed that although the presence of an operation was less effective on rectum doses, it increased organs at risk doses in all fractions (Table 5).

Similarly, when OAR doses were evaluated in terms of applicator shape, since the selection of applicator in operated patients would be cylindrical, OAR doses were statistically higher in cylinder applications than in tandem + ring applications however, rectum doses were less affected (Table 6).

The limitations of the present study were that although patients were taken into the treatment with nutritional advice and standard enema applications, rectum fullness could have a wide-range among the fractions. Thus, a more standard treatment approach may be possible with methods with which rectum fullness can be monitored objectively. Another limitation of our study was that the patient population was relatively low. Further studies with wider number of patients are needed.

5. Conclusion

3D Adaptive Brachytherapy (3D-ABRT) ensures that the volumes are determined in the most accurate way by observing the changes in target tissue and surrounding tissues in each application. In this way, it is possible to apply high doses directly to the target volume without increasing the morbidity risk in organs at risk. Furthermore, treatment accuracy can be increased with routine preparations before the treatment and by imaging in each fraction.

References

1. World Health Organization. Global Health Observatory. Geneva: World Health Organization; 2018. who.int/gho/database/en/. Accessed June 21, 2018.
2. Kizilkaya HO, Kutluhan Dogan A, Dag Z et al, A Comparison of Magnetic Resonance and Computed Tomography Imaging Based Target-Volume Definition and Interfraction Variations of Treatment Planning Parameters (D_{90} HR-CTV, D_{2cc} for OARs) During Image Guided Adaptive Brachytherapy for Cervical Cancer. UHOD 2019; 29(4): 227-237.
3. Manea E, Escande A, Bockel S et al. Risk of Late Urinary Complications Following Image Guided Adaptive Brachytherapy for Locally Advanced Cervical Cancer: Refining Bladder Dose-Volume Parameters. Int J Radiat Oncol Biol Phys 2018 Jun 1;101(2):411-420
4. Westerveld H, Nesvacil N, Fokdal L et al, Definitive radiotherapy with image-guided adaptive brachytherapy for primary vaginal cancer, Lancet Oncol. 2020 Mar;21(3):e157-e167.

5. Tanderup K, Georg D, Pötter R, et al. Adaptive management of cervical cancer radiotherapy. *Semin Radiat Oncol* 2010;121–9.
6. Viswanathan AN, Thomadsen B American Brachytherapy Society Cervical Cancer Recommendations Committee, American Brachytherapy Society. American Brachytherapy Society consensus guidelines for locally advanced carcinoma of the cervix. Part I: General principles. *Brachytherapy*. 2012;11:33–46.
7. Dankulchai P, Petsuksiri J, Chansilpa Y, et al. Image-guided high-dose-rate brachytherapy in inoperable endometrial cancer. *Br J Radiol*. 2014;87:20140018.
8. Van den Bos W, Beriwal S, Velema L, et al. Image guided adaptive brachytherapy for cervical cancer: Dose contribution to involved pelvic nodes in two cancer centers. *J Contemp Brachytherapy*. 2014;6:21–7.
9. Rangarajan R. Interfraction Variations in Organ Filling and Their Impact on Dosimetry in CT Image Based HDR Intracavitary Brachytherapy. *J Med Phys*. 2018;43(1):23- 27
10. Patel RB, Gururajachar JM, Revathy T, Implications of bladder volume on target coverage and dose to critical structures during high dose rate intracavitary brachytherapy for cervical cancer: A dosimetric study. *J Cancer Res Ther*. Oct-Dec 2019;15(6):1207-1211.
11. Kim R. Y, M.D, Shen S, Lin HY, et al. Effects of bladder distension on organs at risk in 3D image-based planning of intracavitary brachytherapy for cervical cancer. *Int J Radiat Oncol Biol Phys*. 2010;76:485–9
12. Adli M, Garipagaoglu M, Kocak Z. Effect of bladder distention on bladder base dose in gynaecological intracavitary high dose rate brachytherapy. *Br J Radiol*. 2009;82:243–8.
13. Jamema S.V, Mahantshetty U, Tanderup K, et al. Inter-application variation of dose and spatial location of D2cm3 volumes of OARs during MR image based cervix brachytherapy 2013; *Radiotherapy and Oncology* 107: 58–62
14. The GEC-ESTOAR Handbook of Brachytherapy. <http://www.estro-education.org/publications/Documents/GEC-ESTOARHandbookofBrachytherapy.html>
15. Viswanathan AN, Erickson BA. Three-dimensional imaging in gynecologic brachytherapy: a survey of the American Brachytherapy Society. *Int J Radiat Oncol Biol Phys*. 2010;76:104–9.
16. Davidson MT, Yuen J, D'Souza DP, et al. Image-guided cervix high-dose-rate brachytherapy treatment planning: Does custom computed tomography planning for each insertion provide better conformal avoidance of organs at risk? *Brachytherapy*. 2008;7:37–42.
17. Kirisits C, Lang S, Dimopoulos J, et al. Uncertainties when using only one MRI-based treatment plan for subsequent high-dose-rate tandem and ring applications in brachytherapy of cervix cancer. *Radiother Oncol*. 2006;81:269–75.
18. Cengiz M, Gurdalli S, Selek U, et al. Effect of bladder distension on dose distribution of intracavitary brachytherapy for cervical cancer: Three-dimensional computed tomography plan evaluation. *Int J Radiat Oncol Biol Phys* 2008;70:464–468.
19. Sun LM, Huang HY, Huand EY, et al. A prospective study to assess the bladder distention effects on dosimetry in intracavitary brachytherapy of cervical cancer via computer tomography-assisted techniques. *Radiother Oncol* 2005;77:77–82.
20. Jhingran A, Salehpour M, Sam M et al., Vaginal motion and bladder and rectal volumes during pelvic intensity-modulated radiation therapy after hysterectomy, *Int J Radiat Oncol Biol Phys*. 2012 Jan 1;82(1):256-62.



A Conceptual Framework for Biothermal variations in Municipal Solid Waste landfill under Mesophilic Temperature Regime

Aniekan Essienubong IKPE^{1*}, Akanu-Ibiam Effiong NDON², Promise Joseph ETIM³

¹Department of Mechanical Engineering, University of Benin, PMB. 1154 Benin City, Nigeria

²Department of Civil Engineering, Akwa Ibom State University, Ikot Akpaden, Mkpato Enin, Nigeria

³Department of Agricultural Engineering, Akwa Ibom State University, Mkpato Enin, Akwa Ibom State, Nigeria.

* **Corresponding Author** : aniekan.ikpe@eng.uniben.edu

ORCID: 0000-0001-9069-9676

Article Info:

DOI: 10.22399/ijcesen.737662

Received : 15 May 2020

Accepted : 02 November 2020

Keywords

Mesophilic temperature
Organic waste decomposition
Landfill
Bio-thermal variations
Bioenergy

Abstract:

Conversion of organic fraction of Municipal Solid Waste (MSW) into energy involves a complex biological and thermal reactions. This study presents a conceptual framework for biothermal variations in MSW landfill based on computational modelling. Landfill Mesophilic temperature range (291-321 K) was modelled using SOLIDWORKS simulation module based on steady state thermal analysis, and the biothermal variations obtained were graphically presented. The rate of heat generation in the landfill model varied in the range of 0.111-0.784 W/m³ at initial temperature distribution of 291 K to the range of 2.216-2.837 W/m³ at a terminal temperature distribution of 321 K. The landfill gas temperature varied in the range of 297-306 K at initial landfill temperature of 291 K to the range of 313-324 K at a terminal landfill temperature of 321 K. The aforementioned biothermal landfill variations revealed that, heat is a function of temperature upon which biogas evolve during anaerobic digestion. Furthermore, the total heat generated at the lower section of a landfill is higher than the total heat at the upper section of the system. With proper understanding of the biothermal variations in a landfill, heat energy and biogas can be harnessed for domestic and industrial purposes.

1. Introduction

Landfill is the most widely used and economically viable means of MSW disposal. The sustainable waste management concept of converting waste to energy makes landfill technology to be one of the most effective waste management methods. However, maximizing energy recovery from a given landfill is a function of several factors, of which temperature is one of such. MSW Landfills represent large energy reservoirs where large amount of biogas as well as heat energy are stored, provided its thermal properties are well characterized for optimum output [1]. Landfill temperature varies widely from one landfill to the other, and is affected by the size and height of the landfill, climatic conditions and landfilling operations as well as the type and age of waste deposited [2]. The temperature of waste in MSW

landfills tends to increase gradually over time until a steady elevated temperature is reached generally within regions of the compacted waste mass. The temperature at which anaerobic digestion takes place can be classified under three categories namely: psychrophilic or cryophilic temperature (-20-15°C), mesophilic temperature (18-55°C) and thermophilic temperature (60°C and above). Through pilot tests and experimental investigations, anaerobic digestion of organic substrates for energy recovery have been reported to be optimum within mesophilic temperature range [3, 4]. This is because thermophilic temperature is rarely obtained by natural decomposition process, except through artificial heating to increase the landfill temperature. Results obtained from studies on MSW landfills have been reported on the variations in thermal properties including elevated temperatures [5]. Yesiller et al. [6] measured landfill temperatures up

to 60-90°C in typical solid waste landfills under different climatic conditions across the world. In a landfill containing aluminium processing waste, landfill temperature of over 100°C was reported from the gas wellheads [7]. Yesiller et al. [8] investigated the thermal process of municipal solid waste landfills as a function of operational conditions and climatic region. The heat generated values ranged from 23-77 MJ/m³ without losses. Thermal gradients measured within the compacted waste stream was in the range of -30 and +22°C/m, with average absolute values less than 5°C/m. Steady elevated temperature of the landfill was in the range of 23 and 57°C while the peak heat content values ranged from 12.5 to 47.8°C/day. Yesiller et al. [9] understudied the heat management approaches in Municipal Solid Waste (MSW) landfills based on three strategies namely: extraction, regulation, and supplementation. For all strategies employed in the study, heat energy in the landfill was determined from the difference between temperature of the landfill waste and the temperatures targeted. Data obtained from landfill facilities with relatively low and high rate of heat generation revealed thermal energy ranging from -48.4 to 72.4 MJ/m³ available for heat management. Maximum landfill temperature reported by Rees [10] varied from 40-65°C and were measured along one-third of the mid-section to over one-half depth of the landfill with total waste heights of approximately 20-60m. This is contrary to results reported by Koerner [11], where psychrophilic temperatures between 10 and 20°C were measured for wastes with maximum height of approximately 50m for over 9.5 years. Temperature variation towards the base of MSW landfill was reported between 30-50°C [12, 13]. However, Rees [14] reported the optimum landfill temperature in England for gas production in the range of 40-45°C. An experimental study conducted by Lamothe and Edgers [15] on the effects of environmental parameters on the laboratory compression of waste revealed that settlements increases with increasing temperatures. In a laboratory experiment, the range of optimum temperatures required for mesophilic and thermophilic microorganisms to thrive during waste decomposition process were identified as 35-40°C and 50-60°C [16, 17]. Onnen [18] investigated the thermal behaviour of vertical Heat Extraction Systems (HES) in Landfills using numerical models. The heat extraction rate ranged from 0-2550, 310-3080, and 0-530 W for the first year, peak year, and last year of the heat extraction process. Difference in baseline landfill temperatures and temperatures that are 0m away from the HES ranged from 5.2-43.2°C. An increase was observed in the total heat energy

extracted at increasing waste filling rate. Wastes placed in warmer months resulted in an increase in the total heat energy extracted. In a bottom ash landfill, Klein et al. [19] found the energy released to be 250 MJ/m³, resulting in 97°C peak temperature. Nastev et al. [20] reported the rate of heat generated from MSW landfill as 40.2 kJ/mol of generated CH₄ and CO₂, and the minimum and maximum heat flux as 6.8×10⁻⁷ W/m² and 0.39 W/m². Several studies have been conducted on the bio-thermal variations of landfills. In this study, MSW landfill system was modelled using SOLIDWORKS 2018 version while the mesophilic temperature condition was computed using steady state thermal analysis in SOLIDWORKS flow simulation.

2. Materials and Methods

The 3D isometric landfill system was modelled using SOLIDWORKS 2018 software which is a solid modelling Computer Aided Design (CAD) as well as Computer Aided Engineering (CAE) tool that runs mainly on Microsoft Windows. The modelling steps started with 2D sketch, consisting of geometries such as arcs, points, conics, lines, splines and so on. Dimensions were added to the sketch to define the size and configuration of the geometry. Relations in the tool bar were used to define features such as parallelism, tangency, concentricity, perpendicularity among others. In the part assembly, sketches of individual parts were assembled together to form the intended solid model of the landfill system. The landfill data were obtained from a field prototype in the Faculty of Engineering, University of Benin, Nigeria. Materials used in the construction of the field prototype were used as a guide during selection of the landfill materials from SOLIDWORKS material library. A steady state thermal analysis was carried out to determine the biothermal behaviour of the landfill which was modelled as a closed system. This was done by clicking the simulation study tree in SOLIDWORKS thermal analysis module and selecting the steady state thermal analysis as the study type. The study properties were defined as presented in Table 1 and Table 2. Since biogas which is a combination of gases was not found in the material library, Apply/Edit material icon was clicked on the simulation study tree to add the biogas materials which were: 60% CH₄, 45.3% CO₂, 3% N₂, 1% H₂, 0.2% H₂O, 0.4% NH₃ and 0.1% H₂S. The gas percentage composition were obtained from the landfill prototype in the University of Benin. Applying the conditions in Table 1 and Table 2, the biothermal conditions specified for the landfill model was simulated to check its variations.

Table 1. Parameters for the heat transfer simulation

Type	Inlet volume flow
Faces	Face<7>@LID6-2
Flow parameters	Flow vectors direction: Normal to face Volume flow rate: 0.1000 m ³ /s Mass flow rate: 0.020 kg/s Flow type: Inlet Mass Flow Viscous regime: Turbulent Turbulent intensity: 10% Turbulent length scale: 7% of the Hydraulic diameter Turbulent velocity scale: 5% of the free steam velocity
Thermodynamic parameters	Approximate pressure: 101325.00 Pa Mesophilic Temperature: 291-321 K
Internal materials	Biogas, MSW, Leachate
Ambient air pressure	0.101 MPa
Ambient temperature	294 K
Boundary conditions	Static pressure of 0.202 MPa at the start of each nozzles. The nozzles are 50 mm long, 20 mm wide lids at the start and then 10 mm openings at the end.
Mesh	Automatic, resolution 7.

As presented in Table 2, the following landfill gas parameters used by Orhorhoro et al. [21] and properties of the waste measured by Emmia et al. [22] were also considered in the thermal analysis carried out in this study. Temperature flow trajectory depicting the biothermal conditions at the upper and lower section of the landfill is presented in Figure 1. The landfill models as shown in Figure 2 and 3 incorporates all the functional materials needed for its operation. The gas extraction unit is modelled with four (4) cornered steel rods binned together with copper wire, and the annulus packed with granular materials (non-cancerous stone). Perforated

gas extraction pipe is incorporated at the middle of the four (4) cornered steel rods to allow the flow and channelling of biogas generated from decomposing waste stream in the landfill to storage vessels. Borehole diameter for the gas extraction well is 0.20m while the gas extraction pipe diameter is 0.10m. The landfill model also incorporate perforated pipes buried horizontally (diameter of 0.10m and 0.40-50m spacing) within the compacted waste layers and also within the granular layers (gravel layer) at the bottom of the landfill. The purpose is for transporting and channelling of leachate to a sizable trench (leachate collection

Table 2. Properties of the landfill phases

Properties of the gas Phase	Minimum	Maximum
Pressure (Pa)	18781.47	507113.54
Thermal conductivity (W/mK)	0.015	0.038
Specific heat capacity (KJ/kgK)	600	2100
Density Fluid (kg/m ³)	0.282	0.840
Velocity (m/s)	0	2198.108
Velocity (X) (m/s)	-195.020	195.130
Velocity (Y) (m/s)	-28.893	2197.940
Velocity (Z) (m/s)	-201.483	202.130
Temperature (Fluid) (K)	280.96	330.20
Mach Number	0	7.23
Vorticity (1/s)	22.226	71927.174
Relative Pressure (Pa)	-82543.53	405788.54
Properties of Solid Phase (MSW)	Minimum	Maximum
Density (Kg/m ³)	5.2	9.8
Thermal conductivity (W/mK)	0.3	3.5
Specific heat capacity (KJ/kgK)	1000	2200
Properties of Solid Phase (leachate)	Minimum	Maximum
Density (Kg/m ³)	3.2	5.1
Thermal conductivity (W/mK)	0.200	0.600
Specific heat capacity (KJ/kgK)	1000	3000

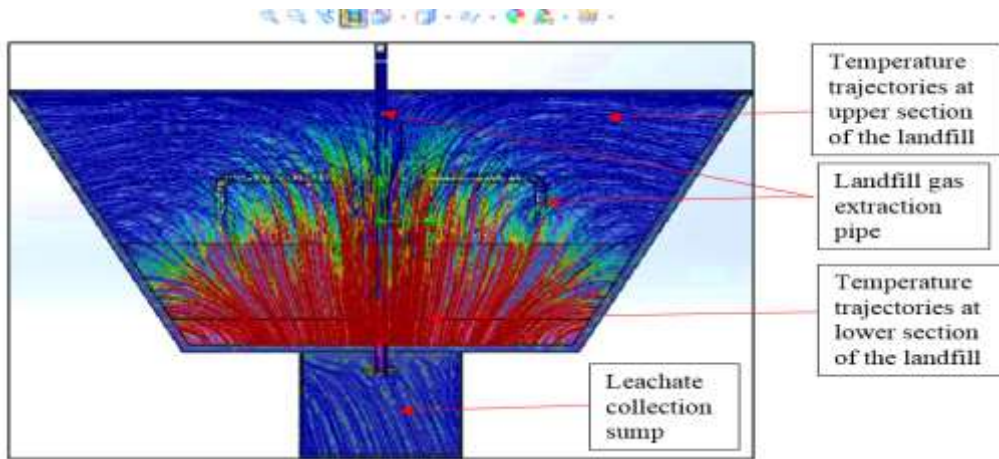


Figure 1. Temperature trajectory depicting the biothermal conditions in the landfill



Figure 2. Cross sectional view of the landfill showing internal components

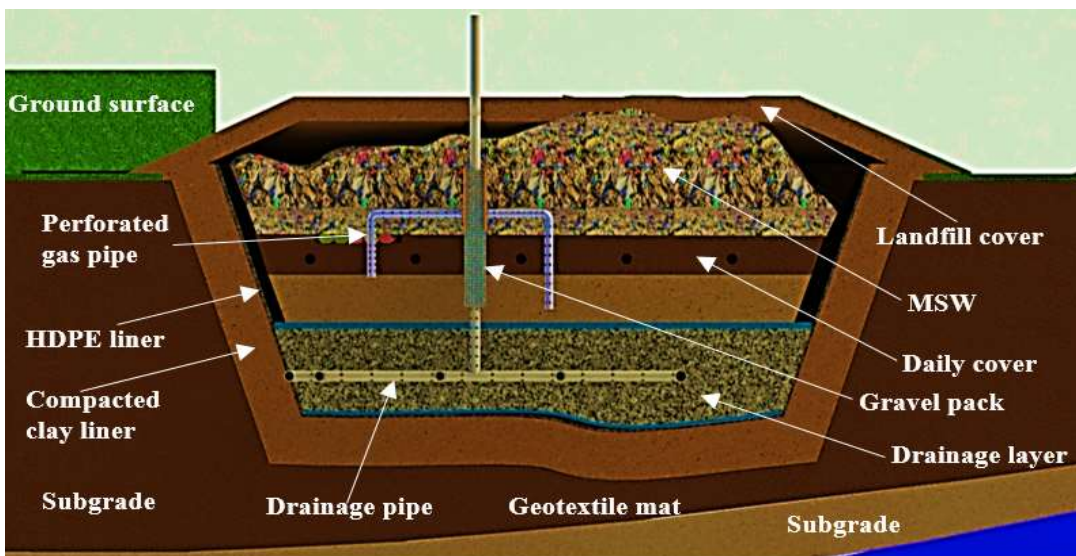


Figure 3. Cross sectional view of the landfill with MSW inside

(primary liner) is further modelled to align properly with the surface of the bentonite clay liner to further prolong water retention in the landfill. The HDPE material specification was thickness of 2mm as presented by Ikpe et al. [23]. The model also incorporates polypropylene geotextile mat or system sump) at a lower base of the landfill for extraction when necessary. The bottom and side walls of the is modelled with bentonite clay (secondary liner) of low hydraulic conductivity ($1 \times 10^{-7} \text{cm/s}$) to delay and control the rate of leachate percolation, while High Density Polyethylene (HDPE) liner geomembrane filter placed on the surface of the granular layer to separate solid particles from liquid content of the waste during decomposition. Specifications of this material as presented by Ikpe et al. [24] are melting point temperature of 30°C , tensile strength between the range of $31.03\text{-}41.37\text{MPa}$ (ISO527), mass of 9613.75 g and thickness of 4.5mm . The waste permeability value was $3 \times 10^{-12} \text{m}^2$, porosity was 0.5 , cover thickness was 0.3m , and the permeability of cover was $1 \times 10^{-13} \text{m}^2$. In evens of the primary and secondary liner failure, ground water monitoring probes is also incorporated in the model to detect the presence of leachate in ground water. The above descriptions of the landfill models are presented in Figure 2 and 3. A method for determining the effect of temperature on landfill gas production is given by Equation 1 [18], while the temperature correction factor describing the temperature dependence of the growth of aerobic bacteria is given by Equation 2 [25].

$$k_{T_2} = k_{T_1} e^{\frac{E_a(T_2 - T_1)}{RT_2 T_1}} \quad (1)$$

$$k_{tem} = \frac{(T - T_{max})(T - T_{min})^2}{(T_{opt} - T_{min}) \left[\frac{(T - T_{opt}) - (T_{opt} - T_{max})}{(T_{opt} + T_{min} - 2T)} \right]} \quad (2)$$

where k_{T_1} is CH_4 production rate at temperature 1, k_{T_2} is CH_4 production rate at temperature 2, E_a is the energy of activation, T is temperature and R is the ideal gas constant, where T is the temperature of the MSW, T_{max} denotes the maximum temperature for aerobic bacterial growth, T_{min} represents the minimum temperature for aerobic bacterial growth and T_{opt} denotes the optimal temperature for aerobic bacterial growth. Hanson et al. [26] modelled the waste heat generation using an exponential growth and decay function with time. The function is give by Equation 3.

$$HG = A \left(\frac{t}{B+t} \right) \left(\frac{C}{C+t} \right) e^{-\sqrt{\frac{t}{D}}} \quad (3)$$

where HG is the generation (W/m^3), T is the temperature ($^\circ\text{C}$), t denotes time (days), A is the peak

heat generation factor (W/m^3), B, C are the time factors (days and D denotes decay factor (days). Combining density, thermal conductivity, and heat capacity the equation for thermal diffusivity is given by Equation 4 [27, 28].

$$\alpha = \frac{k}{\rho c} \quad (4)$$

where α is the thermal diffusivity, k is the thermal conductivity, ρ is the density, c is the heat capacity. The thermal conductivity can be determined from the universal equation of heat flow given by Equation 5 [29].

$$\lambda_{\Sigma} = \lambda_s * \left\{ \frac{K}{[K * \epsilon_s + (1 - \epsilon_s)] * [\epsilon_s + (1 - \epsilon_s) * K]} \right\}^D * [\epsilon_s + (1 - \epsilon_s) * K] \quad (5)$$

where K is the proportionality factor λ_s is the thermal conductivity, D is dispersion state, ϵ_s volumetric fraction of the landfill. The three dimensional transient heat transfer equation is given by Equation 6 [27, 28].

$$\frac{\partial T}{\partial t} = \alpha \left(\frac{\partial^2 T}{\partial x^2} + \frac{\partial^2 T}{\partial y^2} + \frac{\partial^2 T}{\partial z^2} \right) + \dot{Q}_{hg} \quad (6)$$

Where T is the landfill temperature, t denotes time (days), α is the thermal diffusivity and \dot{Q}_{hg} is the volumetric rate of heat generation. The equivalent heat conductivity is given as:

$$\lambda_{eq} = \phi \lambda_g + (1 - \phi) \lambda_s \quad (7)$$

where λ_s is heat conductivity of solid phase, λ_g is heat conductivity of gas phase, ϕ is the waste porous media. The equivalent heat capacity within a landfill system is given by Equation 8.

$$C_{eq} = \phi \rho_g c_{pg} + \rho_d c_{ps} \quad (8)$$

where c_{ps} is the specific heat capacity of solid phase, c_{pg} is the specific heat capacity of the phase. Heat capacity for the landfill surrounding soil is given by Equation 9 [30].

$$C_s \rho_s = C_m \rho_d + C_w \rho_d \frac{w_w}{100} \quad (9)$$

where C_s is the heat capacity of soil, ρ_s is the soil density, C_m is the heat capacity of mineral constituents, ρ_d is the dry soil density, C_w is the heat capacity of leachate, and w_w is moisture content. At any depth of the landfill, temperature can be determined at any time of the year using Equation 10 [31].

$$T_{z,t} = T_m + A_z \text{Sin} \left(\frac{2\pi t}{p} - z \sqrt{\frac{\pi}{\alpha p}} \right) \quad (10)$$

where $T_{z,t}$ is the temperature at depth at different landfill depth z and time t , T_m is the mean annual earth temperature, A_z is the temperature amplitude at depth, z is the depth beneath ground surface, α is the soil thermal diffusivity. The waste volumetric heat capacity is given by Equation 11 [32].

$$C_w \sum_{i=1}^n x_i (C_i) \tag{11}$$

where C_w is the volumetric heat capacity of waste. However, the heat capacity of buried waste can be determined using Equation 12.

$$C_{p,s} = x_{msw} [(1 - \varphi) \sum_{i=1}^n C_{p,i} x_i + \varphi C_{p,H_2O}] + x_{ash} C_{p,ash} \tag{12}$$

where $C_{p,s}$, $C_{p,i}$, and $C_{p,ash}$ are the heat capacities of buried waste, i is the biodegradable component in wet refuse, and ash, and φ is the moisture content. Using the analytical formulation for ground temperature, the baseline waste temperatures can be determined as [33]:

$$T_{(x,t)} = T_m - A_s e^{-x\sqrt{\pi/365\alpha}} \cos \left[\frac{2\pi}{365} \left(t - t_0 - \frac{x}{2} \sqrt{\frac{365}{\pi\alpha}} \right) \right] \tag{13}$$

where $T_{(x,t)}$ is the temperature at depth x and time t , T_m is the mean annual earth temperature, A_s is the amplitude of surface temperature wave x is the depth below the landfill surface, t is the time of the year in days and t_0 is the phase constant. Ground temperature in the vicinity of the landfill due to constant heat rate in polar coordinate is given by Equation 14.

$$\theta(r, t) - \theta_0 = \frac{q_l}{4\pi k} \int_{r^2}^0 \frac{e^{-u}}{u} du \tag{14}$$

where θ_0 is the ground initial temperature, q_l is the heat rate per length of the landfill, k is the thermal conductivity and α is the thermal diffusivity of the ground. Based on the finite-line source theory, Zeng et al. [34] proposed the analytical equation for temperature response in the ground as:

$$\theta(r, z, t) - \theta_0 = \frac{q_l}{4\pi k} \int_0^H \frac{\operatorname{erfc} \left(\frac{\sqrt{r^2 + (z-h)^2}}{2\sqrt{\alpha t}} \right)}{\sqrt{r^2 + (z-h)^2}} - \frac{\operatorname{erfc} \left(\frac{\sqrt{r^2 + (z+h)^2}}{2\sqrt{\alpha t}} \right)}{\sqrt{r^2 + (z+h)^2}} dh \tag{15}$$

where H is the depth and erfc is complementary error function. Municipal solid waste is a porous medium with pore spaces between irregularly shaped solid grains. Analytical equations applicable to heat conduction in porous media is given by Equation 16 [35].

$$\begin{cases} (1 - \phi) \rho_s c_s \frac{\partial \theta_s}{\partial t} = (1 - \phi) \nabla \cdot (k_s \nabla \theta_s) \\ \quad + (1 - \phi) Q_s + h(\theta_f - \theta_s) \\ \phi \rho_f c_f \frac{\partial \theta_f}{\partial t} + (\rho_f c_f) q_f \cdot \nabla \theta_f = \phi \nabla \cdot (k_f \nabla \theta_f) \\ \quad + (1 - \phi) Q_f + h(\theta_s - \theta_f) \end{cases} \tag{16}$$

where θ_s and θ_f are the solid and fluid temperatures, ρ_s and ρ_f are the densities of solid and liquid phases c_s and c_f are specific heat capacities of solid and liquid phases, k_s and k_f are heat conductivities, Q_s and Q_f are sources for liquid phases, ϕ is the landfill waste porosity and h is the exchange heat transfer coefficient. However, the constitutive equations for heat transfer in porous media is given by Equation 17 [36].

$$\begin{cases} (1 - \phi) \rho_s c_s \frac{\partial \theta_s}{\partial t} = (1 - \phi) k_s \nabla^2 \theta_s + h(\theta_f - \theta_s) + (1 - \phi) Q_s \\ \phi \rho_f c_f \frac{\partial \theta_f}{\partial t} + \rho_f c_f q_f \cdot \nabla \theta_f = \phi k_f \nabla^2 \theta_f - h(\theta_f - \theta_s) + \phi Q_f \end{cases} \tag{17}$$

3. Results and Discussion

written SOLIDWORKS flow simulation was used to simulate the internal condition of the landfill system based on mesophilic temperature ranging from 291-321K. Figure 4 shows the flow trajectory of mesophilic temperature distribution within the landfill system. However, Figures 5a-f are graphical representation of mesophilic temperature distribution between 291 and 321 K across the landfill system. The temperature flow trajectory within the landfill system is a function of heat transfer across the entire system as shown in Figure 4. In the hydrolysis phase of anaerobic digestion in the landfill, carbohydrates, fats and proteins are broken down by microorganisms into simple sugars and fatty acids. The products of hydrolysis are broken down into carbonic acids, alcohol, hydrogen, carbon dioxide and ammonia in the acidogenesis phase, while the products of acidogenesis are further broken down into hydrogen, acetic acid and carbon dioxide in the acetogenesis phase. In the methanogenesis phase, the products of acetogenesis are broken down by methanogenic bacteria into biogas which primarily consists of methane and carbon dioxide. The chemical reactions taking place through the aforementioned anaerobic digestion of organic fraction of MSW in a landfill generally have three by-products namely: solid which is the digestates left after decomposition, liquid which is the leachate generated from the process and gas which is the biogas that is processed into bio-methane. Obtaining the bi-products is a function of some parameters, particularly temperature which

enable microbes present in the system to thrive and effective breakdown organic fraction of the waste. This is because, increases in the landfill temperature stimulate gas particle movement, tending also to increase the gas pressure, so that landfill gas spreads more quickly.

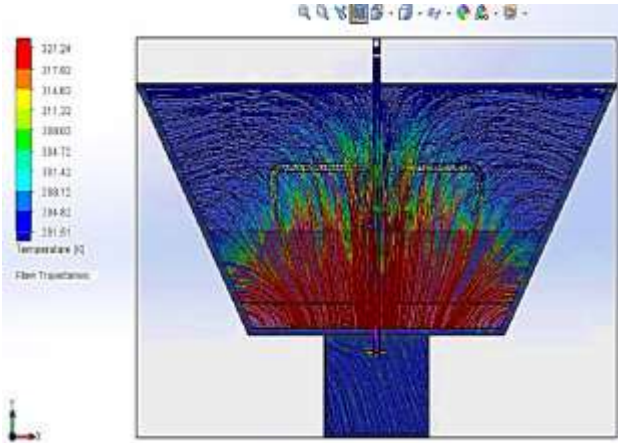


Figure 4. Trajectory of mesophilic temperature distribution within the landfill

Landfill temperature which takes the form of heat begins to flow gradually as decomposition takes place in the landfill. The heat which is a function of organic waste decomposition and landfill temperature begins to flow from a region of higher temperature to a region of lower temperature inside the landfill. Depending on the landfill temperature, the initial heat transfer inside the landfill may not have a wide range of coverage, thus resulting in a non-uniform temperature profile represented as scattered plot in Figures 5a and Figure 5b. This usually takes place during hydrolysis phase or the initial time when waste is newly placed in the landfill. At this stage, the necessary chemical reactions, microbial activities, as well as waste decomposition is not fully developed. After these phases shown in Figure 5a and Figure 5b, the heat distribution continues through acidogenesis phase until a constant temperature is attained within the landfill system where further decomposition of organic feedstock will cause further generation, distribution and increase (in acetogenesis phase) in the landfill temperature as shown in Figures 5c-e respectively. When all operating conditions are fully developed and well established, further increase or decrease is no longer observed in the landfill temperature. This phase of anaerobic digestion in the landfill is referred to as stabilization phase, a process where all operating conditions (temperature, available nutrients, Potential of Hydrogen-pH, water

content, C/N ratio etc.) have stabilized and the system performs optimally. Under such condition, the landfill will produce gas at a steady rate for as long as the condition remains optimally constant. It is important to note that waste materials in the landfill serves as food for the microorganisms while the nutrients present in the waste serves as supplements needed for their growth. After a long term operation of the landfill, nutrient availability in the waste begins to deplete due to the long term consumption/decomposition by microorganisms. This has a direct effect on the landfill performance, as microbial activities will reduce as a result of insufficient waste food or nutrient for microbes to feed on and maintain the anaerobic condition of the system. At this stage, a decline is likely to be observed in the biogas yield, landfill temperature and pressure. This is graphically represented in Figure 5f, where the trend in landfill temperature is gradually decreasing, thus, having a negative effect on the landfill operating conditions. The variations in heat generation rate at each mesophilic temperature used in this investigation are presented

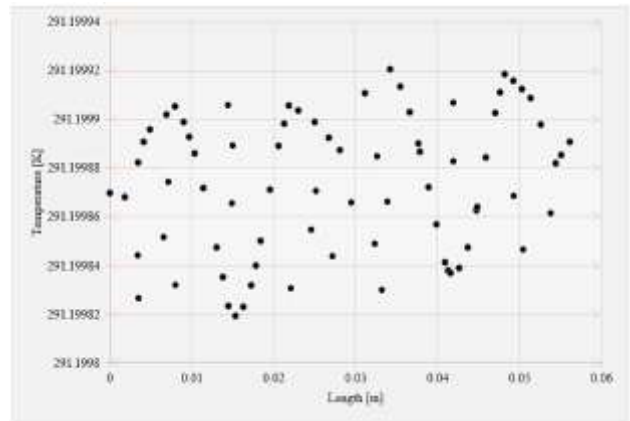


Figure 5a. Temperature distribution at 291 K across the landfill system

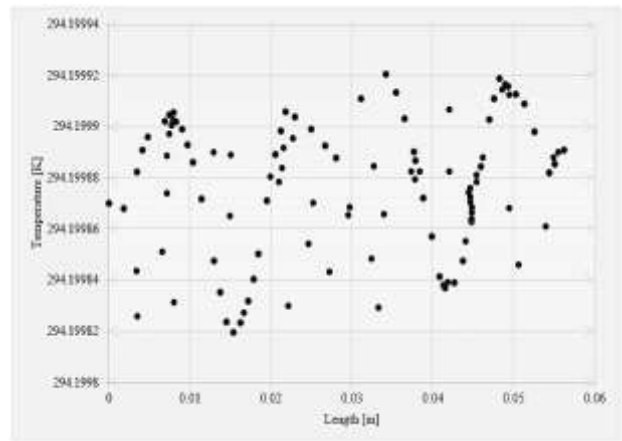


Figure 5b. Temperature distribution at 294 K across the landfill system

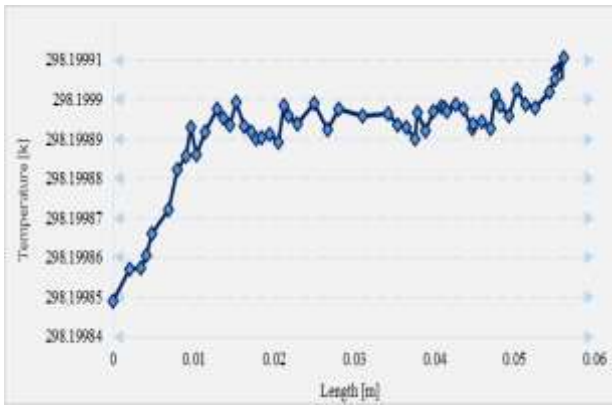


Figure 5c. Temperature distribution at 298 K across the Landfill System

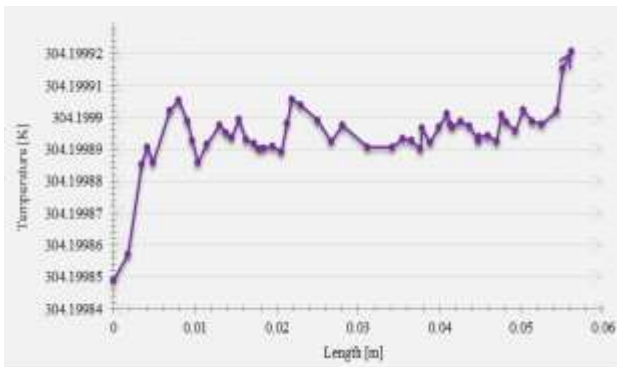


Figure 5d. Temperature distribution at 304 K across the landfill system

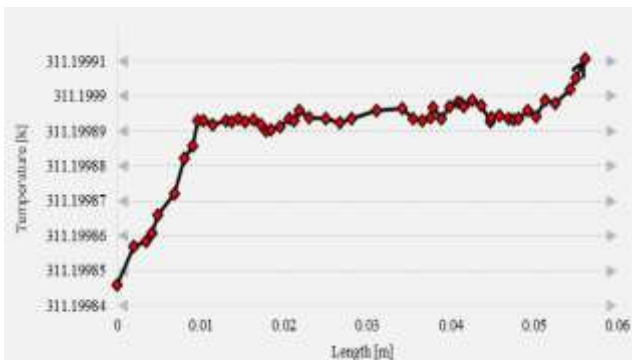


Figure 5e. Temperature distribution at 311 K across the landfill system

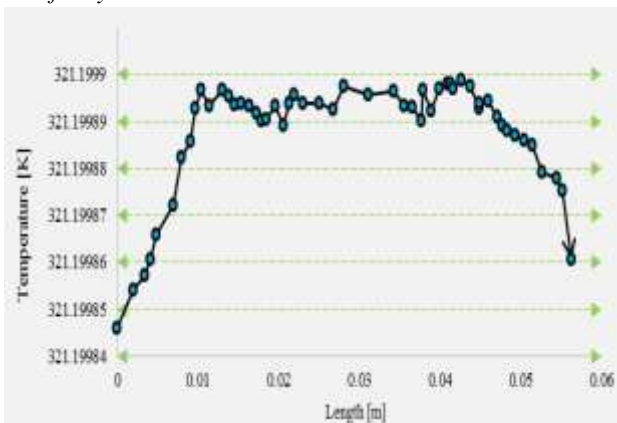


Figure 5f. Temperature distribution at 321 K across the landfill system

in Figures 6a-f. At landfill temperature of 291K, the rate of heat generation in the system varied from 0.111-0.784 as shown in Figure 6a, at landfill temperature of 294K, the rate of heat generation in the system varied from 0.301-0.974 as shown in Figure 6b. Furthermore, at landfill temperature of 298K, the rate of heat generation in the system varied from 0.813-1.485 as shown in Figure 6c, at landfill temperature of 304K, the rate of heat generation in the system varied from 1.320-1.892 as shown in Figure 6d. Moreover, at landfill temperature of 311K, the rate of heat generation in the system varied from 1.714-2.387 as shown in Figure 6e, at landfill temperature of 321K, the rate of heat generation in the system varied from 2.216-2.854 as shown in Figure 6f. There is correlation between the aforementioned values obtained for heat generation rate in this study and that of Emmia et al. [22], Hanson et al. [26], Magyar [29], Hanson et al. [37] and Nocko et al. [38]. The variations in heat rate is observed to increase as the temperature condition increases. It can be observed in the heat transfer trajectories that higher heat values tends to be at the lower section of the landfill profile while lower heat values are observed at the upper section of the landfill. This is because when waste is placed in the landfill cells, there is oxygen starvation, increased moisture content and increased heat at the bottom part of the landfill than the upper part. Reason being that, waste materials in the landfill are highly compacted/compressed, during which all possible voids are filled up and pore spaces eliminated, leaving the base of the landfill with little or air. Furthermore, water contents present in the waste materials flow downward under gravity to the bottom of the landfill. Since the landfill is conditioned for anaerobic digestion, the anaerobes which are poisoned by air migrates to the bottom of the system. The high concentration of anaerobic microorganisms at the lower part of the system causes increase in microbial activities, thereby, increasing the rate of heat generated at the lower section of the system than the upper section. This is indicated by red colour and also by the heat values, that variations in the rate of heat generation and distribution is higher at the lower section of the landfill profile (see Figure 6a-f), than the upper section. It is important to note that, heat variation in the landfill is directly proportional to the temperature of the landfill. Therefore, if there is a reduction in the rate of heat generation and distribution at any part of the landfill, the temperature in that part of the system may decline as well. Figures 7a-f are graphical representation of landfill gas temperature variation at landfill temperature ranging from 291-321 K.

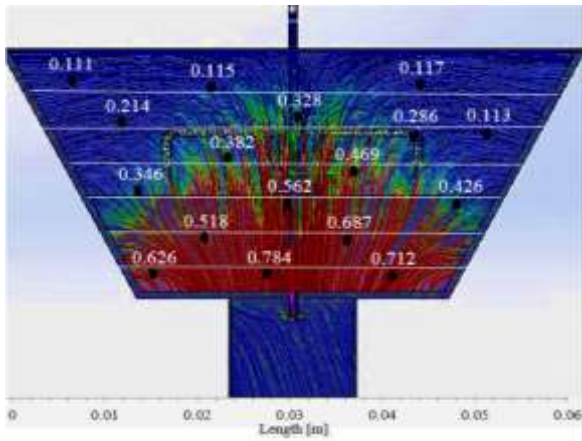


Figure 6a. Variation in landfill heat rate(W/m^3) at temperature distribution of 291 K

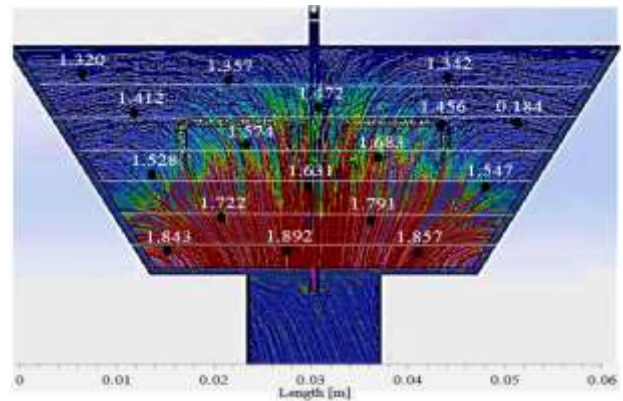


Figure 6d. Variation in landfill heat rate (W/m^3) at temperature distribution of 304 K

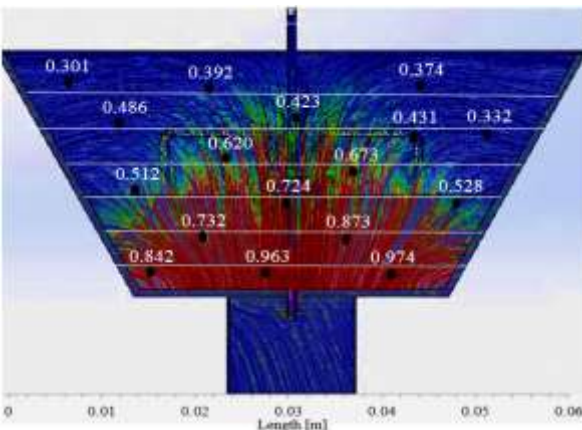


Figure 6b. Variation in landfill heat rate(W/m^3) at temperature distribution of 294 K

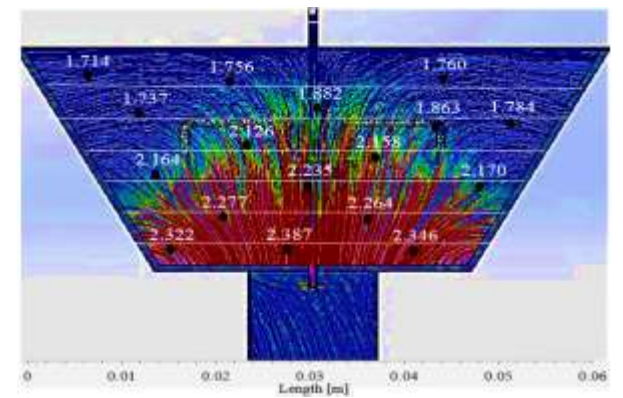


Figure 6e. Variation in landfill heat rate (W/m^3) at temperature distribution of 311 K

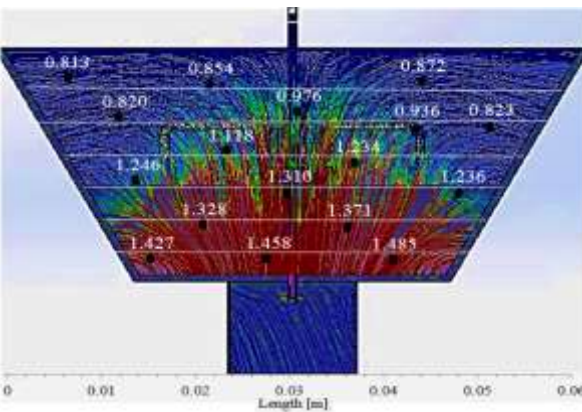


Figure 6c. Variation in landfill heat rate (W/m^3) at temperature distribution of 298 K

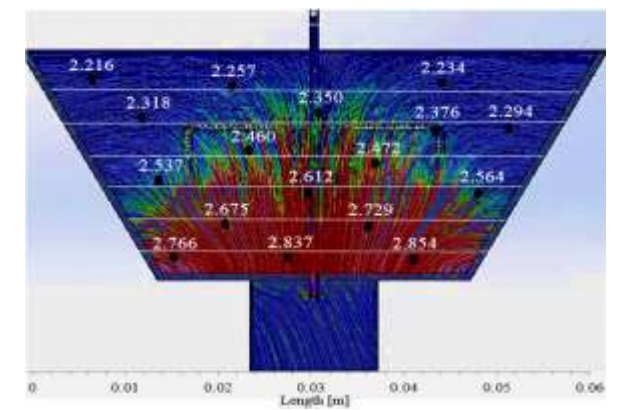


Figure 6f. Variation in landfill heat rate (W/m^3) at temperature distribution of 321 K

The trend in the landfill gas temperature plots is sinusoidal, implying that the landfill gas temperature inside the system increases and decreases at the same time. This is because, of the variations in microbial activities inside the landfill. As discussed earlier in the case of heat generation and distribution rate, the heat concentrates highly in areas with highest microbial activities, and so does the peak temperatures and biogas evolving from the landfill

process areas or cells. That is the reason why some landfill cells produce higher biogas yield than other cells in the same landfill. It can be observed in Figures 7a-f, that the landfill gas temperature variation at the lower section of the landfill appears to be the peak gas temperature values, while the landfill gas temperature variation at the upper section of the landfill tends to be the minimum gas temperature values. Generally, gas flows from a region of higher concentration to the region of lower concentration within the boundaries of a system. In this case, the landfill gas flows from the landfill

compacted waste mass at the lower section of the system to the upper part (known as gas holder) where gas concentration is lowest. During this process, temperature of the gas at the time it leaves the lower section of the landfill decreases gradually as it flows towards the upper section where there are no microbial activities. This implies that the landfill gas temperature decreases as the gas flows upward towards the landfill cover. This also applies to the landfill gas temperature flowing through the gas extraction pipes laid within the compacted waste mass, as the temperature around the gas extraction point reduces to some extent during extraction. Temperature of the final extracted landfill gas is the difference between the landfill gas temperature at the upper and lower section of the landfill system.

4. Conclusion

Investigation of this type generally requires the design and construction of at least a prototype landfill, where the necessary data required for further development is obtained. In recent times, Computer aided tools have been employed in three dimensional modelling and simulation of a landfill and its biothermal process. The mesophilic temperature conditions and biothermal variations in MSW landfill was successfully modelled in this study using SOLIDWORKS heat simulation module.

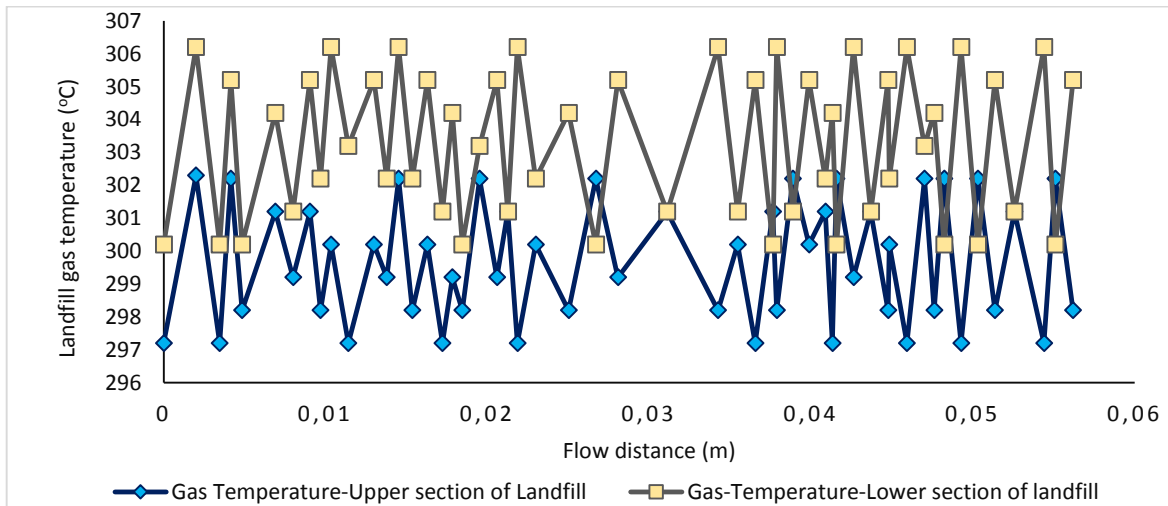


Figure 7a. Landfill gas temperature variation at landfill temperature of 291 K

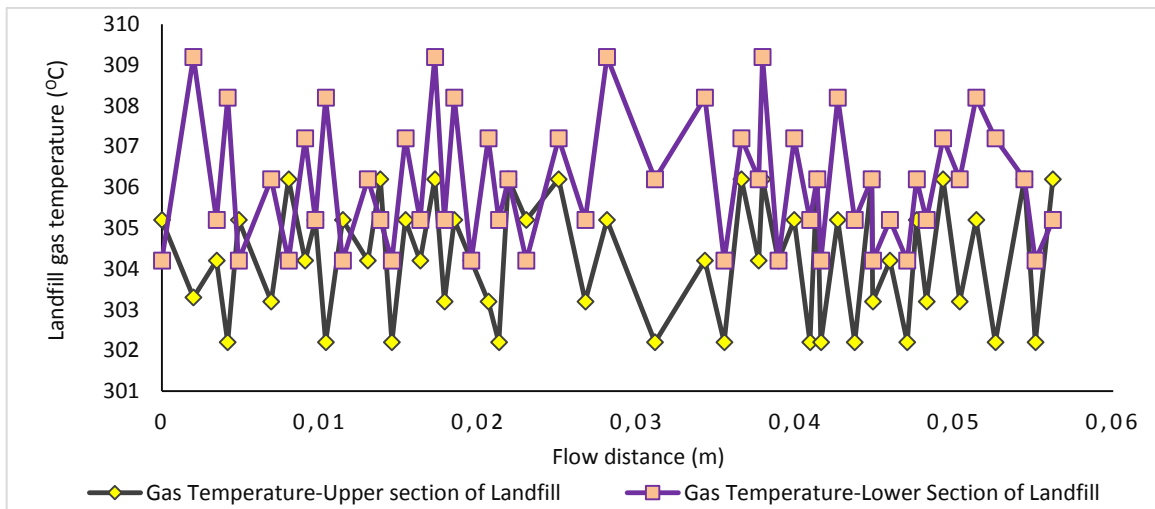


Figure 7b. Landfill gas temperature variation at landfill temperature of 294K

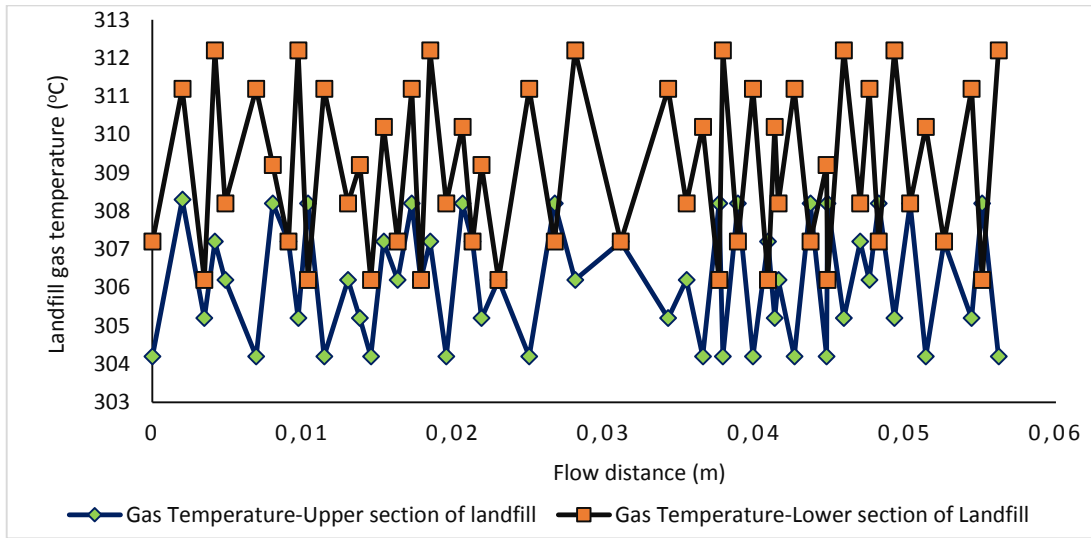


Figure 7c. Landfill gas temperature variation at landfill temperature of 298K

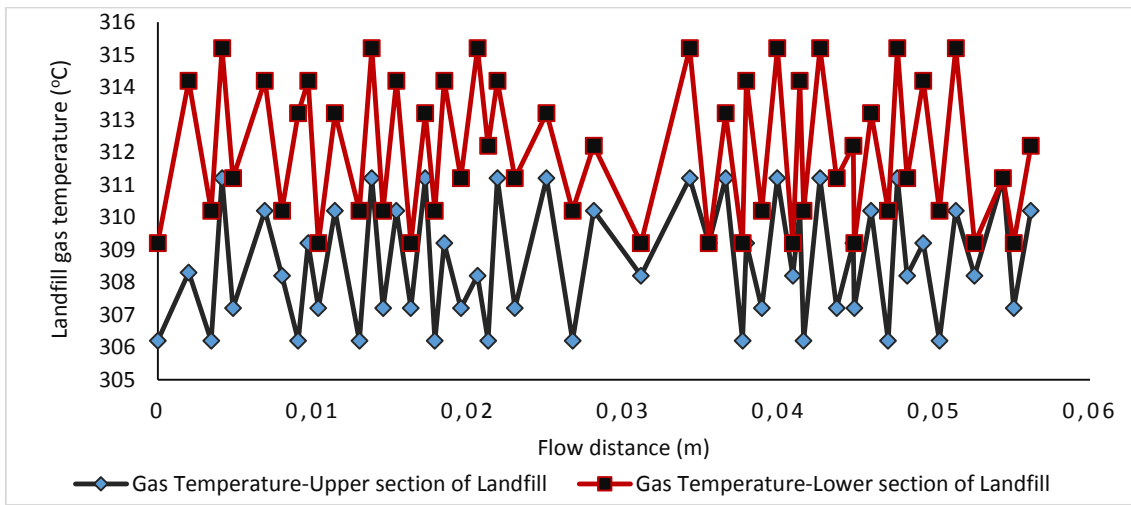


Figure 7d. Landfill gas temperature variation at landfill temperature of 304 K

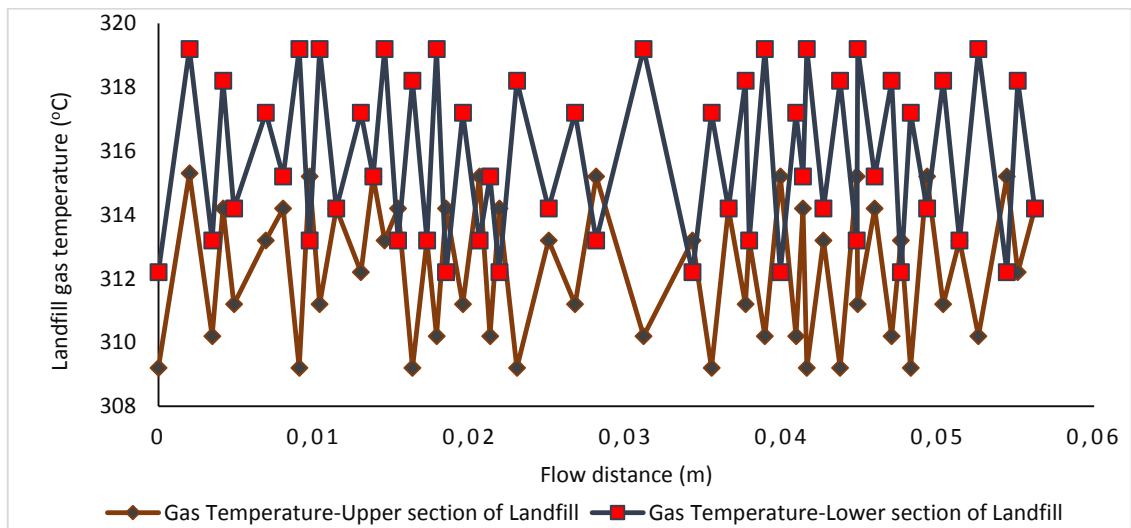


Figure 7e. Landfill gas temperature variation at landfill temperature of 311 K

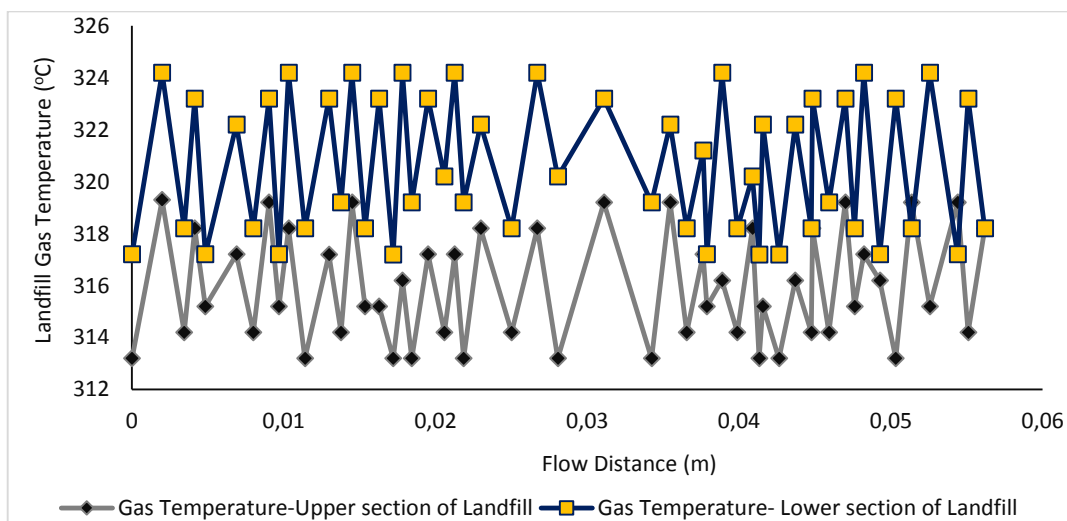


Figure 7f. Landfill gas temperature variation at landfill temperature of 321 K

Values obtained from the landfill model as the heat generation rate ranged from 0.111-2.837 W/m³ at mesophilic temperature range of 291-321, and correlated with landfill heat generation values reported in other investigations. Findings obtained from this study revealed that landfill gas temperature as well as the heat rate is maximum within the compacted waste stream placed in the landfill cells, and gradually reduces through cooling as it flows upwards from a region of higher concentration (around the decomposing waste stream at the lower section of the landfill) to a region of lower concentration (towards the gas holder at the upper section of the landfill). The study also indicated that constant increase in the landfill temperature can accelerate the rate of organic waste decomposition which in turn accelerates the gas generation and flow rate within the landfill. Finally, it is important to note that the biothermal process in a landfill system is optimum only when the pH of the feedstock is within the neutral range, internal temperature of the system is adequate to enhance decomposition, moisture content is sufficient to enable microorganisms thrive and above all, feedstock with proper carbon to nitrogen ratio is selected.

References

- [1] Faitli, J., Magyar, T., Erdélyi, A., Murányi, A. "Characterization of thermal properties of municipal solid waste landfills". *Waste Management*, 36(2015), 213-221.
- [2] Wang, Y., Pelkonen, M., Kaila, J. "Effects of Temperature on the Long-Term Behaviour of Waste Degradation, Emissions and Post-Closure Management Based on Landfill Simulators". *The Open Waste Management Journal*, 5(2012), 19-27.
- [3] Eburnilo, P. O., Okovido, J. Ikpe, A. E. "Investigation of the energy (biogas) production from co-digestion of organic waste materials". *International Journal of Energy Applications and Technologies*, 5, 2(2018), 68-75.
- [4] Ikpe, A. E., Imonitie, D. I., Ndon, A. E. "Investigation of Biogas Energy Derivation from Anaerobic Digestion of Different Local Food Wastes in Nigeria". *Academic Platform Journal of Engineering and Science*, 7, 2(2019), 332-340.
- [5] Hanson, J. L., Yesiller, N., Oettle, N. "Spatial and temporal temperature distributions in municipal solid waste landfills". *Journal of Environmental Engineering*, 136, 8(2010), 804-814.
- [6] Yesiller, N., Hanson, J. L., Yee, E. H. "Waste heat generation: a comprehensive review". *Waste Management*, 42(2015), 166-179.
- [7] Jafari, N. H., Stark, T. D., Rowe, R. K. "Service life of HDPE geomembranes subjected to elevated temperatures". *Journal of Hazardous Toxic and Radioactive Waste*, 18, 1(2014), 16-26.
- [8] Yesiller, N., Hanson, J.L., Liu, W. L. "Heat generation in municipal solid waste landfills". *Journal Geotechnical and Geoenvironmental Engineering*, 131, 11(2005), 1330-1344.
- [9] Yesiller, N., Hanson, J. L., Kopp, K. B. and Yee, E. H. "Heat management strategies for MSW landfills". *Waste Management*, 56(2016), 246-254.
- [10] Rees, J. F. "Optimisation of methane production and refuse decomposition in landfills by temperature control". *Journal of Chemical Technology and Biotechnology*, 30, 8(1980), 458-465.
- [11] Koerner, G. "In situ temperature monitoring of geosynthetics used in a landfill". *Geotechnical Fabrics Report*, 19, 4(2001), 12-13.
- [12] Dach, J., and Jager, J. "Prediction of gas and temperature with the disposal of pretreated residential waste". *5th International Waste Management and Landfill Symposium*, T. H.

- Christensen et al., eds., CISA, Italy, 1, 665-677, 1995.
- [13] Yoshida, H., Tanaka, N., and Hozumi, H. "Theoretical study on heat transport phenomena in a sanitary landfill". 6th International Waste Management and Landfill Symposium, T. H. Christensen et al., eds., CISA, Italy, 1(1997), 109-120.
- [14] Rees, J. F. "The fate of carbon compounds in the landfill disposal of organic matter". *Journal of Chemical Technology and Biotechnology*, 30, 4(1980), 161-175.
- [15] Lamothe, D., and Edgers, L. "The effects of environmental parameters on the laboratory compression of refuse". 17th International Madison Waste Conference, University of Wisconsin, Madison, Wisconsin, 592-604, 1994.
- [16] Tchobanoglous, G., Theisen, H., and Vigil, S. A. "Integrated solid waste management: Engineering principles and management issues". McGraw-Hill, New York, 1993.
- [17] Cecchi, F., Pavan, P., Musacco, A., Mata-Alvarez, J., and Vallini, G. "Digesting the organic fraction of municipal solid waste: Moving from mesophilic (37°C) to thermophilic (55°C) conditions". *Waste Management Research*, 11(1993), 403-414.
- [18] Onnen, M. T. "Thermal Numerical Analysis of Vertical Heat Extraction Systems in Landfills". California Polytechnic State University, San Luis Obispo, 2014.
- [19] Klein, R., Nestle, N., Niessner, R., Baumann, T. "Numerical modelling of the generation and transport of heat in a bottom ash monofill". *Journal of hazardous materials*, 100, 1-3(2003), 147-162.
- [20] Nastev, M., Therrien, R., Lefebvre, R., Gelinat, P. "Gas production and migration in landfills and geological materials". *Journal of contaminant hydrology*, 52, 1-4(2001), 187-211.
- [21] Orhorhoro, E. K., Ikpe, A. E., Ukwaba, S. I. "Effects of Landfill Gas Flow Trajectories at Three Distinct Temperature Phases on the Stress-Strain-Displacement Properties of a Gas Extraction Pipe". *Journal of Applied Science and Environmental Management*, 22, 11(2018), 1737-1743.
- [22] Emmia, G., Zarrellaa, A., Zuanettia, A., De Carlia, M. "Use of municipal solid waste landfill as heat source of heat pump". *Energy Procedia*, 101(2016), 352-359.
- [23] Ikpe, A. E., Ndon, A. E., Adoh, A. U. "Modelling and Simulation of High Density Polyethylene Liner Installation in Engineered Landfill for Optimum Performance". *Journal of Applied Science and Environmental Management* 23, 3(2019), 449-456.
- [24] Ikpe, A. E., Ndon, A. E., Etuk E. M. "Parametric Study of Polypropylene Based Geotextile Mat for Optimum Performance in Engineered Landfill Systems". *Applications of Modelling and Simulation*, 4(2020), 149-158.
- [25] Omar, H. M., Rohani, S. "Transport Phenomena in the Conversion of an Anaerobic Landfill into an Aerobic Landfill". University of Western Ontario, Canada, 2015.
- [26] Hanson, J. L., Liu, W., and Yesiller, N. "Analytical and Numerical Modelling of Temperatures in Landfills". *Proceedings of Selected Sessions of Geo-Congress 08: Geotechnics of Waste Management and Remediation*, ASCE GSP No. 177, Reston, Virginia, 24-31, 2008.
- [27] Holman, J. P. "Heat Transfer". 8th Edition, McGraw-Hill, Inc., United States, 1997.
- [28] Mills, A. F. "Basic Heat and Mass Transfer". 2nd Edition, Prentice-Hall Inc., New Jersey, 1999.
- [29] Magyar, T. "Laying the Foundation for Engineering Heat Management of Waste Landfills". Mikoviny Sámuel Doctoral School of Earth Sciences, University of Miskolc, 2017.
- [30] Jumikis, A. R. "Thermal Soil Mechanics". 2nd Edition, Rutgers University Press, New Brunswick, New Jersey, 1996.
- [31] Labs, K. "Regional Analysis of Ground and Above-Ground Climate". ORNL/SUB-81/4045/1, U.S. Department of Energy, Office of Buildings Energy R&D, 1981.
- [32] Yoshida, H., Hozumi, H., and Tanaka, N. "Theoretical Study on Temperature Distribution in a Sanitary Landfill". *Proceedings 2nd International Congress on Environmental Geotechnics*, A.A. Balkema, Osaka, Japan, 323-328, 1996.
- [33] Hao, Z. "Understanding and Predicting Temperatures in Municipal Solid Waste Landfills". North Carolina State University, Raleigh, North Carolina, 2020.
- [34] Zeng, H. Y., Diao, N. R. and Fang, Z. H. "A finite line-source model for boreholes in geothermal heat exchangers, Heat Transfer". *Asian Research*, 7(2020), 558-567.
- [35] Yang, Y. "Analyses of Heat Transfer and Temperature-induced Behaviour in Geotechnics". Ruhr-University, Bochum, Germany, 2016.
- [36] Nield, D., Bejan, A. "Convection in porous media, 3rd Edition". Berlin, Springer, 2006.
- [37] Hanson, J. L., Yesiller, N., Onnen, M. T., Liu, W., Oettle, N. K., Marinos, J. A. "Development of numerical model for predicting heat generation and temperatures in MSW landfills". *Waste Management* 33(2013), 1993-2000
- [38] Nocko, L. M., McCartney, J. S., Gupta, R., Botelho, K., Morris, J. "Heat Extraction from Municipal Solid Waste Landfills". *Proceedings, 43rd Workshop on Geothermal Reservoir Engineering*, Stanford University, Stanford, California, February 12-14, 2018, SGP-TR-213, 2018.



Modeling Hyperelastic Materials by MATLAB

Ahmad NASER ALDEEN¹, Yücel CAN², Murat YAZICI^{1*}

¹ Bursa Uludağ University, Engineering Faculty, Automotive Engineering Department, Bursa-TURKEY

² R&D Center, Oyak-Renault, Bursa-TURKEY

* Corresponding Author: myazici@uludag.edu.tr

ORCID: 0000-0002-8720-7594

Article Info:

DOI: 10.22399/ijcesen.662707

Received: 20 December 2019

Accepted: 11 November 2020

Keywords

Elastomer,
Mooney-Rivlin,
Hyperelastic materials

Abstract:

The finite element studies of hyperelastic materials always need founding a mathematical model describes the behavior of their elements. Several constitutive models differ in matching accuracy, can describe the behavior of hyperelastic material, such as Neo-Hookean, Yeoh, and Mooney-Rivlin, which are all derived from the strain energy density function.

Founding a mathematical model describing some hyperelastic material's behavior means the determination of the constitutive model's invariants, which are considered material parameters.

In this work, the two-parameter Mooney-Rivlin model was chosen to demonstrate the procedure of forming the mathematical model that describes the mechanical behavior of an incompressible hyperelastic material. Comparing with those results taken from Abaqus, obtained results were very close and exhibited a lower absolute error. This procedure can be considered as a general method to describe the hyperelastic materials by the other polynomial constitutive models.

1. Introduction

The finite element method used to study the material's mechanical performance is subject to various difficulties, starting with finding an appropriate mathematical model that describes element performance. As it is known, with a more accurate mathematical model, more realistic results are obtained.

Hooke's law is accurately characterized by linear elastic materials, but this law is not appropriate to describe many materials such as hyperelastic materials, which perform nonlinearly. Specific constitutive models are used in Finite element studies of hyperelastic materials, like Neo-Hookean, Mooney-Rivlin [1], Arruda-Boyce [2], and Ogden model. The constitutive model is chosen to respect the kind of data and the strain working range [3]. Mooney-Rivlin model is a special case of stress-energy density function [4], which has two

terms associated with the material's shear flexibility and compressibility.

$$W = \sum_{i+j=1}^N C_{ij}(I_1 - 3)^i (I_2 - 3)^j + \sum_{i=1}^N \frac{1}{D_i} (J_{el} - 1)^{2i}$$

Where C_{ij}, D_i Material's parameters, I_1, I_2 Strain invariants and J_{el} elastic volume ratio. The hyperelastic materials, in general, including the rubber-like materials, have a little compressibility compering with its shear flexibility. This little compressibility is not considerable for 2D elements or when the element is not highly restricted, but it should be considered in the 3D problems or in a highly restricted case [5]. The Mooney-Rivlin model is a linear combination of two strain invariants of the left Cauchy-Green deformation tensor [6]. It's derived by taking the first term of

shear flexibility (N=1), and considering the incompressibility of hyperelastic materials ($J_{el} = 1$). It is known that the Mooney-Rivlin model gives accurate results up to 200% of strains.

$$W = C_1 (I_1 - 3) + C_2 (I_2 - 3)$$

The specimen chosen in the experiments has a quiet little thickness compared with its high and width, so it can be considered a shell that is processed as an incompressible material.

The materials parameters in the Mooney-Rivlin model have a close relationship with the second shear modulus G expressed by,

$$G = 2 (C_1 + C_2)$$

2. Determining material parameters

The hyperelastic materials can be defined by determining its parameters, so the hyperelastic model characterizing the material's performance will be determined. In general, the parameters of the hyperelastic models derived from strain energy density function (i.e., C1, C2, C3...) are determined by statistical analysis utilizing one of the coding programs, such as Matlab or Python (Matlab was chosen in this paper). Depending on experimental points, an equation system will be formed. Then this system will be solved to acquire the common solutions, which are the material's parameters. The chosen common solution should dedicate an objective function, which is mostly the least-squares criterion [7].

$$\min: S = \sum_{q=1}^4 w_q (\sum_{i=1}^{n_q} ((f_q)_i - (\sigma_q)_i)^2)$$

The w_q, n_q are weight of different experiment types and the number of experimental data for each experiment, respectively. The number of experiment types is q. Here, the number of tests is 4. $(f_q)_i, (\sigma_q)_i$ notations are the predicted value by the equation and experimental value, respectively.

Notice that the model found is valid to predict the results of the tests considered before when the model's parameters were acquired, i.e., the model found considering uniaxial tension test only is invalid for a biaxial or planar test [8]. So to obtain a more general model, all kinds of tests should be considered [7]. In general, the determination of material's parameters requires implantation of four kinds of tests, uniaxial tension, biaxial tension, planer (pure shear) test, and volumetric tension (Volumetric tension test is only required when the compressibility can't be ignored in the 3D analyses

or unrestrained objects, so it is neglected in this paper).

Rivlin [9] formed the differential equations to connect nominal stresses and principal stretch ratio λ ($\lambda=1+\epsilon$).

For the uniaxial tensile test:

$$T=2(1-\lambda^{-3})(\lambda \frac{\partial W}{\partial I_1} + \frac{\partial W}{\partial I_2})$$

For the equibiaxial tensile test:

$$T=2(\lambda-\lambda^{-5})(\frac{\partial W}{\partial I_1} + \lambda^2 \frac{\partial W}{\partial I_2})$$

For the planar or pure share test:

$$T=2(\lambda-\lambda^{-3})(\frac{\partial W}{\partial I_1} + \frac{\partial W}{\partial I_2})$$

The hyperelastic constitutive model must dedicate Drucker's stability postulate [10], which decides that if a material is stable or not. According to Drucker, the typical material curves must have no softening region at the end of the tension test, but if it has, it is considered as unstable material. So Drucker's stability condition is expressed as follows:

$$\sum_i \partial \sigma_i \partial \epsilon_i \geq 0$$

Where $\partial \sigma_i$ is presented an increment in the principal Cauchy stress. Also, an increment of the corresponding strain is described by $\partial \epsilon_i$.

The materials' parameters described above can be obtained by the following procedure explained step by step.

- Choosing a hyperelastic model depending on the objective of this model and the working strain range.
- Using Rivlin's relations between stretch ratios and nominal stresses for uniaxial, biaxial, and pure shear tests.
- Derivation of the chosen strain energy density function respects the strain invariants to obtain stress-strain relations for each test type.
- Substituting the experimental points in the relations leads to forming an equation system, whose unknowns are the material's parameters.
- Searching for common solutions by implementing statistical analyses, using the least square criterion by Matlab or Python.
- Investigating Ducker's stability conditions.

3. The validation of the procedure

To ensure that the procedure and written code were implemented correctly, an example of a rubber (incompressible material) with known material parameters was chosen [5].

The experimental results corresponding to the uniaxial tension test, the biaxial tension test, and the planer test are shown in tables 1, 2, and 3. The comparison between Abaqus and Matlab code results is shown in Figures 1, 2, 3. The comparison showed high matching quality for all test kinds. Table 4 shows the Similarity between the material's parameters acquired by Abaqus and Matlab.

Table 1. Uniaxial tension test

Stress (Pa)	Strain
0.054E6	0.0380
0.152E6	0.1338
0.254E6	0.2210
0.362E6	0.3450
0.459E6	0.4600
0.583E6	0.6242
0.656E6	0.8510
0.730E6	1.4268

Table 2. Equibiaxial tension test

Stress (Pa)	Strain
0.089E6	0.0200
0.255E6	0.1400
0.503E6	0.4200
0.958E6	1.4900
1.703E6	2.7500
2.413E6	3.4500

Table 3. Planer tension test

Stress (Pa)	Strain
0.055E6	0.0690
0.324E6	0.2828
0.758E6	1.3862
1.269E6	3.0345
1.779E6	4.0621

Table 4. Material's parameters

	Abaqus	Matlab
C1	176050	173740
C2	4330	4590
Absolute error	1,1757e+11	1,1090e+11

Conclusion:

The mechanical performance of a hyperelastic material was modeled by Matlab, considering three

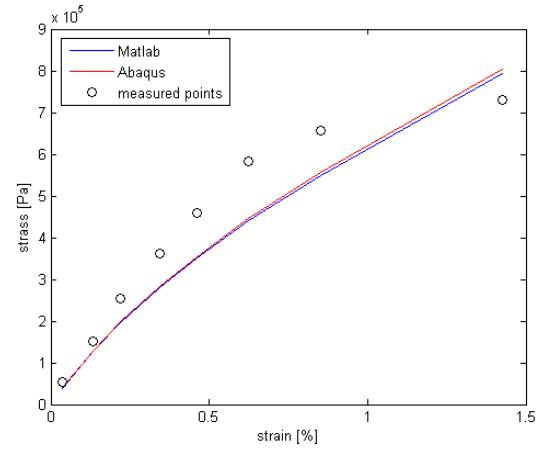


Figure 1. Uniaxial tension test

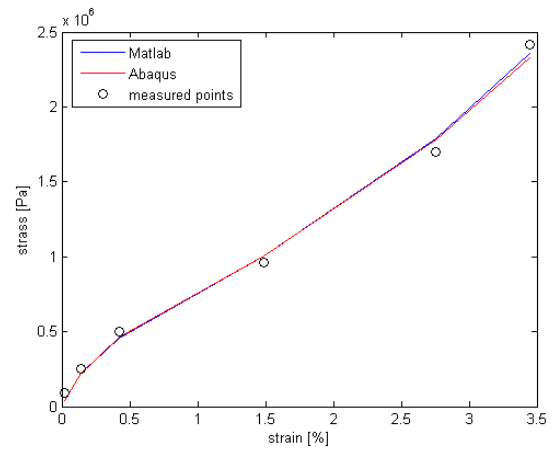


Figure 2. Equibiaxial tension test

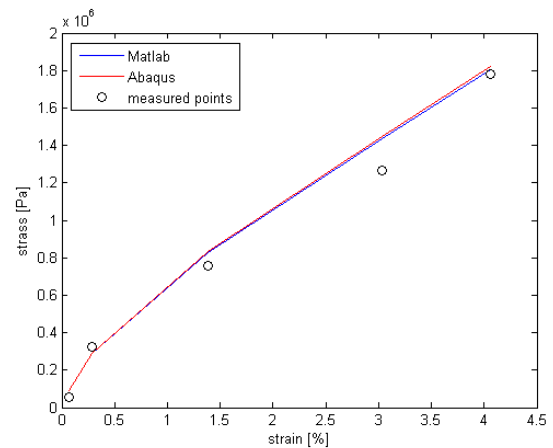


Figure 3. Planer shear test

kinds of tests uniaxial, equibiaxial, and planer tension tests. The results predicted by Matlab code well matched both of the experimental points, and those results were taken from Abaqus, so the

procedure used produced a mathematical model describing the material's performance successfully. The results obtained by the Matlab code had a less absolute error.

References

- [1] Kumar, N., Rao, V.V. "Hyperelastic Mooney-Rivlin Model : Determination and Physical Interpretation of Material Constants" MIT International Journal of Mechanical Engineering, 6, 1(2016)43–46.
- [2] M. C. Boyce, E. M. Arruda, "Constitutive models of rubber elasticity: A review" Rubber Chemistry and Technology.73,3(2000)504–523,DOI: <https://doi.org/10.5254/1.3547602>
- [3] B. Kim, S. B. Lee, J. Lee, S. Cho, H. Park, S. Yeom, S. H. Park, A comparison among Neo-Hookean model, Mooney-Rivlin model, and Ogden model for Chloroprene rubber. International Journal of Precision Engineering and Manufacturing, 13,5(2012)759–764. <https://doi.org/10.1007/s12541-012-0099-y>
- [4] M. Mooney, "A Theory of Large Elastic Deformation" Applied Physics,11,(1940)582. <https://doi.org/10.1063/1.1712836>
- [5] Anonim 2019. Abaqus 6.14 Documentation. <http://ivt-abaqusdoc.ivt.ntnu.no:2080/texis/search/?query=wetting&submit.x=0&submit.y=0&group=bk&CDB=v6.14>.
- [6] H. Menderes, and A. W. A. Konter, "Advanced FE Analysis of Elastomeric Automobile Components under Realistic Loading Conditions," Proceedings of the First European Conference on Constitutive Models for Rubber, pp. 3-12 (1999).
- [7] Y. Wu, H.Wang and A. Li, "Parameter Identification Methods for Hyperelastic and Hyper-Viscoelastic Models" Applied Sciences, 6,12-386(2016)1-13. <https://doi.org/10.3390/app6120386>
- [8] D. J.Charlton, J.Yang, K. K. Teh,. "A Review of Methods to Characterize Rubber Elastic Behavior for Use in Finite Element Analysis" Rubber Chemistry and Technology,67,3(1994)481–503. <https://doi.org/10.5254/1.3538686>
- [9] R.S. Rivlin, "Large Elastic Deformations. Rheology: Rheology", Academic Press, (1956) 351–385. <https://doi.org/10.1016/B978-0-12-395694-1.50016-6>
- [10] D.C. Drucker "A definition of a stable inelastic material", J. Appl. Mech.,26 (1959) 101–106.



Calculated hyperfine coupling constants of some sigma-type radicals

Fatih UCUN*, Sadun KÜÇÜK

Süleyman Demirel University, Science and Arts Faculty, Physics Department, 32200, Isparta-Turkey

* Corresponding Author : fatihucun@sdu.edu.tr
ORCID: 0000-0001-7464-7788

Article Info:

DOI: 10.22399/ijcesen.750537

Received : 10 June 2020

Accepted : 11 November 2020

Keywords

Hyperfine Constant
EPR
Radical
Density Functional Theory
Simulation

Abstract:

The hyperfine coupling constants of some σ -type radicals were calculated by using the DFT(B3LYP) method with LanL2DZ basic set. These are phenyl, naphthyl, pyridyl, and quinolyl radicals. Also, the study was enriched by the calculations of the spin densities for all the radicals. From the results it was concluded that the spin density of the unpaired electron is mainly in one sp-hybrid orbital of carbon atom from which hydrogen is removed. The electron paramagnetic resonance (EPR) spectra of all the radicals are generally based on the hyperfine splitting belonging to only the close hydrogen or nitrogen atoms of the benzene ring to the unpaired electron since the effect of the other atoms is disappeared in the linewidth of the EPR spectrum lines. The EPR spectra were also simulated by using their calculated isotropic hyperfine coupling constants and, compared with the experimental data. It was found a good agreement between them.

1. Introduction

Analysis of electron paramagnetic resonance (EPR) spectra of σ -type radicals give detailed information about the distributions of the spin density of the unpaired electron. The bigger hyperfine coupling constant means the higher spin density. Pyridyl (2-, 3-, and 4-) [1], 2-, 3-, and 4-quinolyl and 4-isoquinolyl [2] radicals generated in argon matrices after UV irradiation were studied by EPR spectroscopy. All these radicals were found to be σ -type radicals. The EPR spectra of the radicals were readily resolved by the identifications of the hyperfine values of the protons of the radicals. The results indicated a little effect of the fused benzene ring upon the nature of the semi filled orbitals of the radicals. Some authors have also reported the observation of the carbon-13 spectra of phenyl, 2-pyridyl, and 2-pyrimidinyl radicals [3]. A specific chemical reaction was used in the preparation of these radicals, and the radicals were trapped in an inert matrix at 77 °K using a rotating cryostat. They found that the unpaired electron is localized mainly in one sp-hybrid orbital of the carbon atom form

which proton is removed and, is not delocalized in the orbital system of the aromatic ring. The electronic ground states of phenyl, 1- and 2-naphthyl, 1- and 9-anthracyl, and 1-pyrenyl radicals were determined by means of EPR in order to find if a crossing of s and p levels occurs as the aromatic ring system is expanded [4]. In all cases the unpaired electron was found to occupy on the essentially nonbonding orbital corresponding to the broken bond.

Some authors have showed that the density functional theory (DFT) method could be helpful to make proper assignments of complex EPR spectra and, to determine the main features of the distributions of the spin densities of overcrowded polycyclic aromatic hydrocarbon radical cations [5]. The hyperfine values of the HCS and the isovalent HCO, HSiS and HSiO radicals were calculated using the B3LYP and MRSDCI methods by Chen and Huang [6]. Isotropic hyperfine coupling constants for the radicals BH_2 , CH_2^- , NH_2 , OH_2^+ , BH_3^- , CH_3 , NH_3^+ , H_2CO^+ and CH_2CH were obtained using the density-functional theory with a gradient-corrected local-spin-density approximation and a

Slater-type-orbital basis set [7]. The hyperfine constants of aromatic radicals containing ^{14}N nucleus were investigated by an extensive study in which there are 165 hyperfine constants belonging to 38 radical species [8]. They were obtained from the computations with the DFT/B3LYP and PBE0 functional combined with 6-31G*, N07D, TZVP, and EPRIII basis sets.

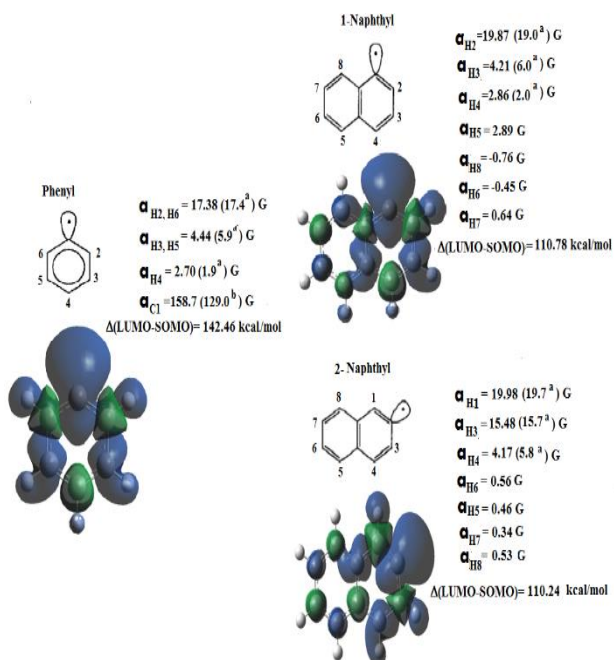


Figure 1. Calculated hyperfine constants and spin densities for phenyl and naphthyl radicals. ^aRef [4] and ^bRef. [13].

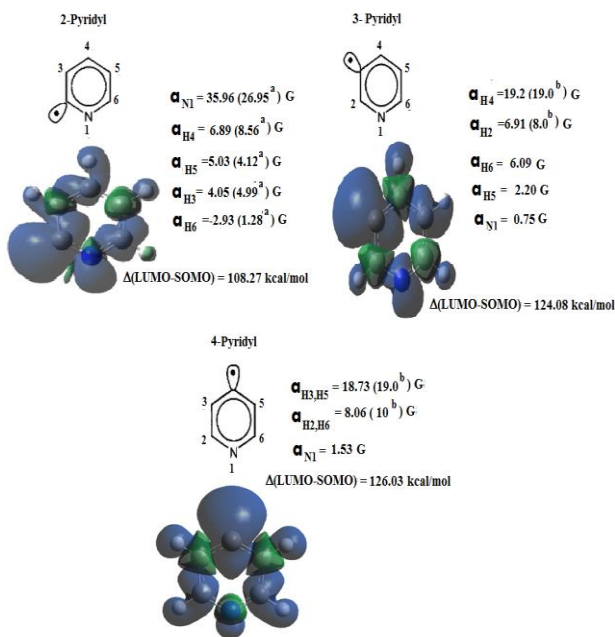


Figure 2. Calculated hyperfine constants and spin densities for pyridyl radicals. ^aRef [3] and ^bRef. [2].

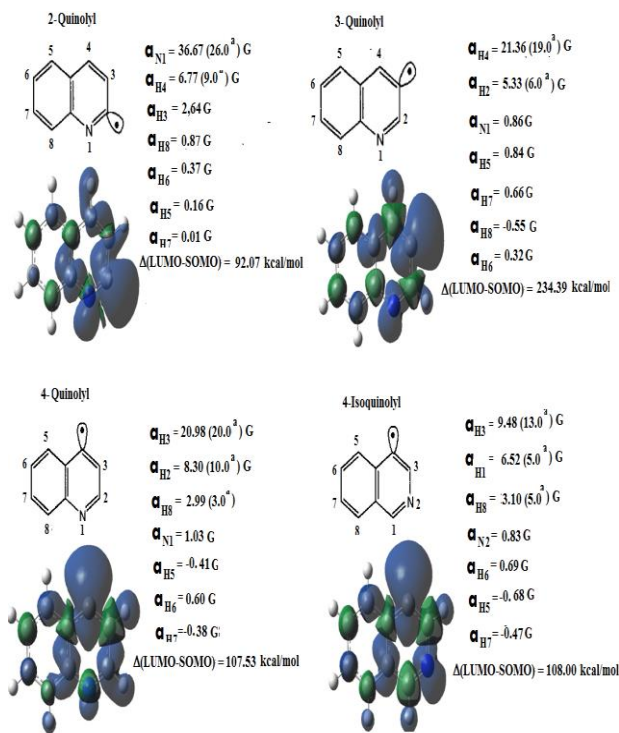


Figure 3. Calculated hyperfine constants and spin densities for quinonyl radicals. ^a Ref [2].

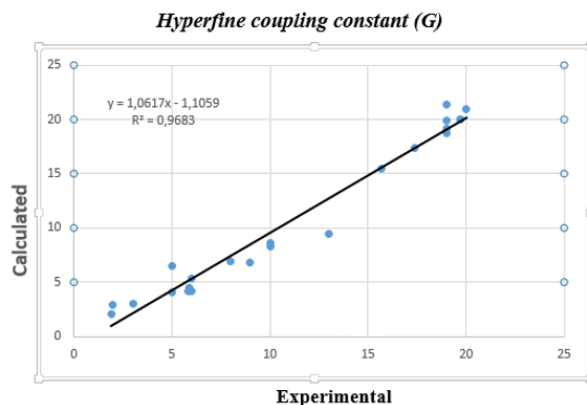


Figure 4. The correlation graph between the experimental and calculated hyperfine constants(G).

In this study the isotropic hyperfine coupling constants of some σ -type radicals were calculated by DFT/B3LYP method at LAN2DZ level. It is aimed to determine the distributions of the spin density of these aromatic radicals.

2. Computational Methods

Our previous studies have showed that the DFT(B3LYP)/LanL2DZ level cause pretty good values in hyperfine calculations [9,10]. So in this study the radicals were optimized by using the DFT (B3LYP hybrid functional) method with LanL2DZ basis set level. All the calculations have been

performed using Gaussian 09 package [11] and Gauss-View molecular visualization programs [12]. The simulated EPR spectra were obtained by using WINEPR SimFonia Version 1.25 software of Bruker.

3. Results and Discussion

The calculated hyperfine coupling constants (hfccs) and spin density distributions of all the radical have been shown in Figs. 1–3, respectively. Figures also show the experimental hfcc values. Taking into account that the calculated results based on a single gas molecule may not match to the experimental one in which multiple interactions takes place, there is reasonable agreement between the calculated and experimental values. Root-mean-square deviations (RMSD) between the experimental and computed hfccs of all the considered radicals except for two big values have been obtained and, given in Figure 4. From the RMSD value of about 1.97 in the figure, it is stated that the LanL2DZ basis set level gives a reasonable good agreement with the experimental data. The spin density distributions of all the radicals in Figs 1-3 show that all these radicals are σ -type radicals. The resolved EPR hyperfine structures of the radicals were readily identified with the hyperfine values of the hydrogen or nitrogen atoms of the radicals. From the figures we can say that the unpaired electron is localized mainly in one sp-hybrid orbital of the carbon atom from which hydrogen is removed and, that the spin densities on the ring hydrogen and nitrogen atoms are fairly low. The hfccs of only the close hydrogen or nitrogen atoms to the unpaired electron are enough big to visible in the EPR spectra of the radicals. The others are too low to appear in the linewidth of the EPR lines. They can only be calculated.

The highest occupied molecular orbital (HOMO) energy is associated with the electron donating ability of a molecule while the lowest unoccupied molecular orbital energy (LUMO) energy is an indicator of its electron accepting ability. HOMO is called as SOMO for semi occupied molecular orbital, namely radicals. The energy gap between E_{HOMO} and E_{LUMO} energy levels (ΔE) is an important parameter as a function of reactivity of a molecule. A molecule with a lower ΔE is more chemical reactive. So, from the ΔE values given in Figs.1-3, 2-naphthyl between naphthyl radicals, 2-pyridyl between pyridyl radicals and 2-quinolyl between quinolyl radicals has the highest chemical reactive. Fig.5-7 shows the simulation and experimental EPR spectra of all the radicals. The simulations spectra were obtained by using the calculated hyperfine coupling constants of the radicals. The most corresponding linewidth values are written in bottom

of the figures. As seen the simulation and experimental spectra suit well. This shows the calculated values of hfcc are in good agreement with the experimental data. The computations of the non-observed hyperfine values completes the EPR analysis of all these radicals.

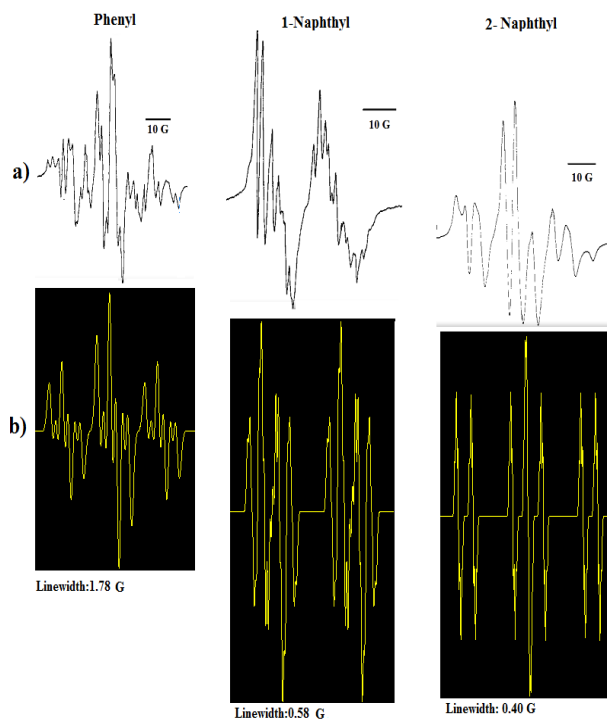


Figure 5. Simulation and experimental spectra of phenyl and naphthyl radicals. The experimental spectra was taken from Ref [4].

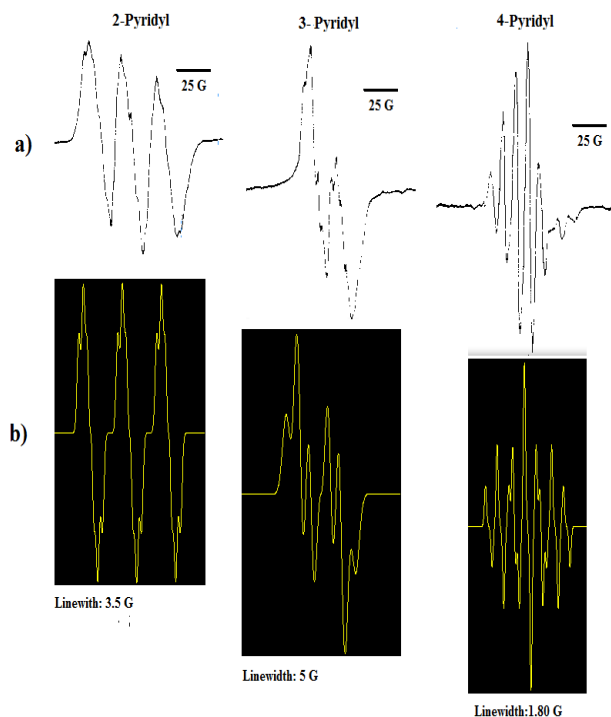


Figure 6. Simulation and experimental spectra of pyridyl radicals. The experimental spectra was taken from Ref [2].

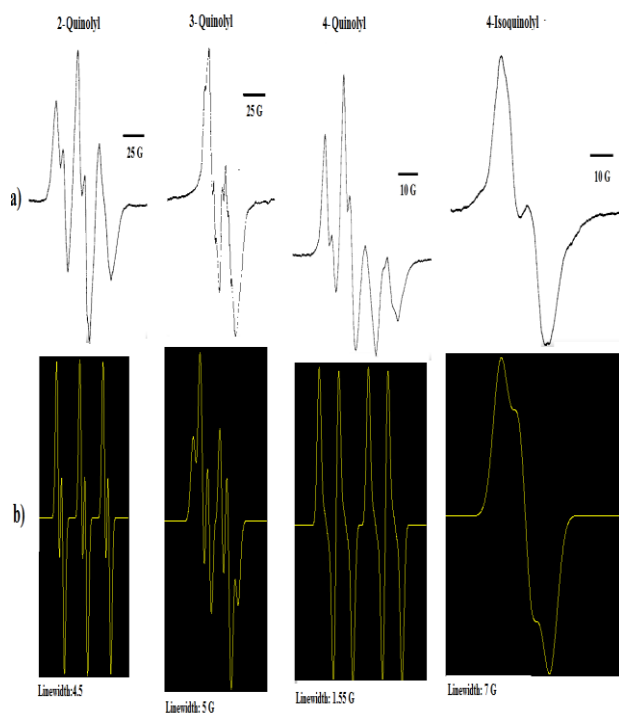


Figure 7. Simulation and experimental spectra of quinolyl radicals. The experimental spectra was taken from Ref [2].

4. Conclusions

The EPR hyperfine coupling constants of some σ -type phenyl, naphthyl, pridyl, and quinolyl radicals were calculated by using the DFT(B3LYP) method with LanL2DZ basic set. The simulated EPR spectra of all the radicals were also found by using the calculated isotropic hyperfine coupling constants and, compared with the experimental data. From the results it was concluded that the unpaired electron is localized mainly in one sp-hybrid orbital of the carbon atom from which hydrogen is removed, and that there is the effect of only the close hydrogen or nitrogen atoms of the fused benzene ring to the unpaired electron upon the EPR spectra of the radicals.

References

- [1] P. H. Kasai and D. McLeod, "Electron spin resonance study of heterocycles. I. Pyridyl radicals" *J. Americ. Chem. Soc.* 94,3(1972)720-727. <https://doi.org/10.1021/ja00758a007>
- [2] P. H. Kasai and D. McLeod, "Electron spin resonance study of heterocycles. V. Quinolyl radicals" *J. Americ. Chem. Soc.* 97,6 (1975) 1548-1551. <https://doi.org/10.1021/ja00839a046>
- [3] H. Zemel and R. W. Fessenden, "Electron spin resonance studies of phenyl and pyridyl radicals in aqueous solution" *J. Physic. Chem.* 79,14 (1975) 1419-1427. <https://doi.org/10.1021/j100581a016>
- [4] P. H. Kasai, P. A. Clark, and E. B. Whipple, "Electronic ground states of aryl radicals" *J. Americ. Chem. Soc.* 92,9 (1970) 2640-2644. <https://doi.org/10.1021/ja00712a009>
- [5] Bo-Z. Chen and Ming-B. Huang, "Hyperfine structure in HCS and related radicals: a theoretical" *Chem. Phys. Lett.* 308, 3-4 (1999) 256-262. [https://doi.org/10.1016/S0009-2614\(99\)00601-6](https://doi.org/10.1016/S0009-2614(99)00601-6)
- [6] T. Wang, F. M. Tang and Y. F. Wu, "A combined EPR and DFT study of the overcrowded aromatic radical cations from Friedel-Crafts alkylation reactions" *J. Mol. Struct.* 1002,1-3 (2011). 128-134. <https://doi.org/10.1016/j.molstruc.2011.07.009>
- [7] N. Ishii and T. Shimizu, "Density-functional-theory calculations of isotropic hyperfine coupling constants of radicals" *Chem. Phys. Lett.* 225,4-6 (1994). 462-466. [https://doi.org/10.1016/0009-2614\(94\)87112-4](https://doi.org/10.1016/0009-2614(94)87112-4)
- [8] L. Hermosilla, G. Vega, C. Sieiro, and P. Calle, "DFT Calculations of Isotropic Hyperfine Coupling Constants of Nitrogen Aromatic Radicals: The Challenge of Nitroxide Radicals" *J. Chem. Theory Comput.* 7, 1 (2011) 169-179. <https://doi.org/10.1021/ct1006136>
- [9] S. Nardali, F. Uçun and M. Karakaya, "Calculated hyperfine coupling constants for 5,5-dimethyl-1-pyrroline N-oxide radical products in water and benzene" *Russian J. Phys. Chem. A (2017)* 91, (2017) 2137-2148. <https://doi.org/10.1134/S0036024417110164>
- [10] F. Uçun and S.G. Aydın, "Calculated optimized structures and hyperfine coupling constants of some radical adducts of α -phenyl-*N*-tert-butyl nitron in water and benzene solutions" *J. Organomet. Chem.* 759, (2014). 27-32. <https://doi.org/10.1016/j.jorganchem.2014.02.011>
- [11] M. J. Frisch, G. W. Trucks, H. B. Schlegel, et al., *Gaussian 09, Revision D.01* (Gaussian, Inc., Pittsburgh, PA, 2009). <https://gaussian.com/g09citation/>
- [12] R. Dennington, T. Keith and J. Millam, *GaussView, Version 5.0.9*, (Semicem Inc., Shawnee Mission: KS, 2009). <https://gaussian.com/g09citation/>
- [13] J. E Bennett and B. Mile "Electron Spin Resonance Spectra of Some -Type Aromatic Radicals" *The J. Phys. Chem.* 75, 22 (1971) 3423,3437. <https://doi.org/10.1021/j100691a005>



Magnetic Nanoparticles Synthesized By Green Chemistry and Investigation of Its Application in the Material Industry

Melise KARATAY KUTMAN^{1*}, F. Zumrut BIBER MUFTULER¹, Ozge KOZGUS GULDU¹, Coşkun HARMANSAH²

¹ Ege University, Department of Nuclear Applications, Institute of Nuclear Sciences, Bornova-IZMIR, TURKEY,

² Ege University, Ege Vocational School, Bornova-IZMIR, TURKEY

* Corresponding Author : melisekaratay35@gmail.com

ORCID: 0000-0002-6057-7552

Article Info:

DOI: 10.22399/ijcesen.733423

Received : 07 May 2020

Accepted : 15 November 2020

Keywords

Green tea

Iron nanoparticles

Non Destructive Testing (NDT)

Abstract:

In the past decade, the use of plants for synthesis of nanoparticles has been intensively studied. Various plants have been employed to synthesize nanomaterials in all fields of science and industry. Particularly, magnetic nanoparticles (MNPs) are emerging as new subjects of research for their application in different fields of industry. Conventional techniques for nanoparticles synthesis require hazardous chemicals that have many risks due to their toxicity and serious concerns for environment and health. On the other hand, plant-mediated synthesis of nanoparticles seems to be having an effective way in developing inexpensive, nontoxic and eco-friendly materials.

The aim of this study is to examine the use of iron magnetic nanoparticles synthesized by green chemistry as a liquid penetrant for investigating potential of detection micro surface flaws on industrial materials. For this purpose, green tea extract (GTE) was used as a reduction agent for synthesis of iron (Fe_3O_4) nanoparticles. GTE has high concentration phenolic and carbonyl groups of polyphenol compounds can be responsible for the formation Fe_3O_4 nanoparticles. The synthesized nanoparticles (Fe_3O_4 -GTE NPs) were characterized by X-ray Photoelectron Spectroscopy (XPS), Transmission Electron Microscopy (SEM) and Vibrating-Sample Magnetometer (VSM). The experimental results showed that plant-mediated iron nanoparticles have great potential as a new penetrant for fluorescent penetrant inspection (FPI) applications.

1. Introduction

Recent advancements of green nanotechnology have been changing most of the existing processes and products. This transformation is making a remarkable impact on diverse science, engineering, industry, and commercial sectors. The unique physical and chemical properties of the nanoparticles can lead to significant enhancements in conductivity, mechanical strength, and optical sensitivity. Their unique properties are enables to use of advanced materials and sensors for engineering applications in industry. The use of metal nanoparticles and nanocomposites in various applications such as electronics, biology,

biomedical applications, and material science depends on its features such as size, shape and composition [1-3].

Nondestructive testing (NDT) is the process of inspecting and evaluating parts or components for discontinuities, or differences in characteristics without destroying the serviceability of the part or system. In other words, when the inspection is finished, the parts can still be reused. Magnetic particle inspection (MPI) is a common NDT technique for detecting flaws on the surface or subsurface of the ferromagnetism material. MPI is an industry standard used extensively from raw to processed materials. Inspection of surface and subsurface crack using magnetic particle has been

widely used in the field of railroad, metallurgy, automobile and aircraft [4]. It is used for the detection of surface defects to evaluated according to predefined quality standards. This method aims at verifying the structure of a part without any damage [5]. The increase of small and micro scale manufacturing has increased the need for advanced NDT techniques. From this perspective, aim of our study is to develop herbal synthesized magnetic nanoparticle penetrant which can be used in NDT. Thus, the use of plant-based nanoparticle applications particularly will be increased its application in the field of NDT.

2. Materials and methods

2.1 Magnetic Nanoparticles Synthesized by Green Chemistry

The Green tea leaves were washed with double-distilled water. Dry tea residue was added to a solution of distilled water, and $\text{FeCl}_3 \cdot 6\text{H}_2\text{O}$ was dissolved in it by stirring for 4 h and then left overnight. By filtration, $\text{FeCl}_3 \cdot 6\text{H}_2\text{O}$ -treated tea residue was obtained and was dried in an oven. Then, in a muffle furnace, it was heated for 6 h at 450°C , washed, and dried. The resultant product was a crystal structure of Fe_3O_4 (magnetite) [6]. FITC-labeled Fe_3O_4 -GTE NPs as penetrant was applied to the surface of the test material. The synthesis of Fe_3O_4 -GTE NPs was performed as shown in Figure 1.



Figure 1. Synthesis of Fe_3O_4 -GTE NPs.

2.2 Magnetic Particle Test Bar

The Magnaflux Magnetic Particle Test Bar is a test piece with artificial flaws, to establish field direction and determine adequate current levels using AC or DC currents in wet horizontal magnetic particle bench units. The bar contains both fine and coarse defects, surface and sub-surface defects and longitudinal and transverse indications [7]. Magnetic Particle Test Bar specifications are given in Table 1.

2.3 Application of Penetrant on Magnetic Particle Test Bar

FITC-labeled Fe_3O_4 -GTE NPs as penetrant was

Table 1. Specifications of the magnetic test bar.

Dimesions	10"31m x 10mm
Weight	5 lbs.
Magnaflux Part #	- MT-MX-189838
MX Industrial (equivalent to Magnaflux's MPI Test Bar) Part #	- MT-MXI-MX3508 x 1.25" x ³ / ₈ " (approx. 254mm x

applied to the surface of the test material. The synthesized penetrant application is shown in Figure 2. We did our experimental work at Ege University, Aviation Higher Vocational School.

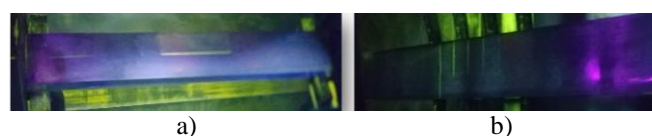


Figure 2. Application of penetrant on test material; a) Horizontal cracks, b) Vertical cracks.

The experimental results showed that plant-mediated iron nanoparticles have great potential as a new penetrant for fluorescent magnetic particle inspection (MPI) applications. Experimental results showed that cracks ranging 254 mm x 31 mm x 10 mm in test block test materials were successfully identified.

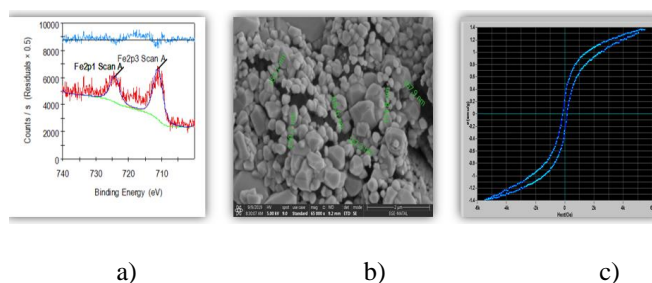


Figure 3. Characterization of a) XPS spectrum related to the elemental survey scan of Fe_3O_4 -GTE NPs, b) SEM images of Fe_3O_4 -GTE NPs, c) The measured magnetic hysteresis of the MNPs by VSM.

2.4 Characterization of Fe_3O_4 -GTE NPs

The synthesized nanoparticles were characterized by X-ray Photoelectron Spectroscopy (XPS), Transmission Electron Microscopy (SEM) and Vibrating-Sample Magnetometer (VSM) in Figure 3.

According to the results of XPS analysis, percentage values of iron, carbon and oxygen in the green tea extract were found 6.64%, 21.31% and 48.76%, respectively. This result shows us that we synthesized Fe_3O_4 nanoparticles with a green

synthesis. The Fe₃O₄@GTE NPs morphological structure was examined using SEM. Fig. 3b shows nanoparticle in the sample at 65000 x magnification under scanning electron microscopy. The size of Fe NPs synthesized using green tea extracts was found to be around 150 and 210 nm, as detected from SEM images. To better understand the magnetic properties of nanoparticles we tested magnetization measurements by using Vibrating Sample Magnetometer (VSM). The hysteresis loop of Fe₃O₄-GTE NPs magnetic behaviors is illustrated in Fig. 3c. VSM measurement showed that synthesized Fe₃O₄-GTE NPs nanoparticles exhibit soft magnetic behavior at room temperature. The Fig. 3c shows the saturation magnetization (Ms) and intrinsic coercivity (jHc) values have been measured 1.37 emu/g and 147.82 Oe respectively.

Conclusion

The synthesized magnetic particle has been developed and tested on a magnetic particle test bar. The preliminary studies demonstrate the usability of the synthesized penetrant. Our result shows that if the synthesized penetrant is optimized, it may be used in MPI applications. The study findings provide a new perspective on the development of a plant-based penetrant to be used in magnetic particle inspection.

References

- [1] H. Duan, D. Wang and Y. Li, Green chemistry for nanoparticle synthesis, *Chem. Soc. Rev.*, 44(16): 5778–5792. DOI: 10.1039/c4cs00363b, 2015.
- [2] J. Virkutyte and R.S. Varma, Green synthesis of metal nanoparticles: Biodegradable polymers and enzymes in stabilization and surface functionalization, *Chem. Sci.*, 2(5): 837–846, DOI: 10.1039/c0sc00338g, 2011.
- [3] W.J. Stark, P.R. Stoessel, W. Wohlleben and A. Hafner, Industrial applications of nanoparticles, *Chem. Soc. Rev.*, 44, 5793-5805, DOI:10.1039/C4CS00362D, 2015.
- [4] J. Zhao, Y. Mi, K. Wang, Y. Ma and J. Yang, Fluorescence Magnetic Particle Flaw Detecting System Based on Low Light Level CCD., *Int. 16th World Conference NDT Proceeding*, pp 1–7, 2004.
- [5] The American Society for Nondestructive Testing, (access time: 20 Sep. 2019) <https://www.asnt.org/MinorSiteSections/AboutASNT/Intro-to-NDT>.
- [6] M.F. Heba, M.M. Fatma, M.H. Marzouq, A.B. Mustafa, A.M. Alsoudi, O.A. Ali, M. Mohamed, F.A. Mahmoud, Review of Green Methods of Iron Nanoparticles Synthesis and Applications, *BioNanoScience*, 8.2: 491-503, DOI: 10.1007/s12668-018-0516-5, 2018.
- [7] NDT Supply; (access time: 25 Sep. 2019), <https://ndtsupply.com/magnaflux-7-magnetic-particle-test-bar.html>.



Copyright © IJCESEN



ISSN: 2149-9144

Research Article

Characterization and Siderophores Production of *Rhizobium* spp. Isolated from wild Legumes

Hatice OGUTCU*, Hulya AVSAR

Ahi Evran University, Faculty of Agriculture, Department of Field Crops, Kırşehir, Turkey

* Corresponding Author : hogutcu@gmail.com

ORCID: 0000-0001-7100-9318

Article Info:

DOI: 10.22399/ijcesen.718084

Received : 10 April 2020

Accepted : 17 November 2020

Keywords:

Rhizobium spp.
Melilotus officinalis
Vicia cracca
Medicago sativa
Siderophore

Abstract:

Legume plants are very significant not only ecologically but also agriculturally because they are responsible for major change of nitrogen from atmospheric N₂ to ammonia. In this study, total 56 isolates of *Rhizobium* spp. which were previously isolated from wild legumes plant (*Melilotus officinalis*, *Medicago sativa* and *Vicia cracca*) existing in the central and the districts of Kırşehir province (Kaman, Mucur, Akpınar, Akçakent, Çiçekdağı, Boztepe). In order to characterize the isolates; YMA containing Bromothymol blue, Congo red, Gram stain reaction, movement, catalase and oxidase tests were evaluated. In addition, isolates of *Rhizobium* spp. (wild type) were screened for their ability to produce siderophores and it was determined that 50 of 56 isolates in total can produce siderophore.

1. Introduction

Legume crops play major role in sustainable agriculture in drought areas. Root nodule bacteria (*Rhizobium* spp.) are widely used in agriculture practice to increase the ability of legume plants to fix atmospheric nitrogen [1]. Nitrogen (N₂) is necessary nutrient for plant growth. Chemical fertilizers are used to achieve high yield in agricultural applications, but they are both expensive and have a significant detrimental effect on the environment. Therefore, environmentally friendly and sustainable agricultural practices have recently increased the interest in organic farming [2,3]. Expanding and increasing the use of bio-fertilizers (for example *Rhizobium* spp.) decreases need for chemical fertilizers, and also reduces the threatening effects of fertilizers on human, soil and the environment [4]. Nowadays, natural legumes plants and symbionts have attracted attention of ecologists due to their tolerance to extreme environmental conditions such as severe drought, high temperature and salinity [5,6,7].

Iron is necessary for all living organisms [8]. In environments where iron deficiency, bacteria supply

their iron requirement by iron-binding ligands called siderophores [9,10].

Siderophore (production and utilization) is specific attention in *Rhizobium* spp. owing to iron is required for nodule creation, leghemoglobin, nitrogenase, ferredoxin other electron transport, and symbiosis [9,11,12]. The objective of this study is to determine the phenotypic properties of natural *Rhizobium* spp. isolated from different ecological areas and their ability to produce siderophore.

2. Material and methods

2.1. Isolation of *Rhizobium* spp. and morphological, physiological, biochemical characterization

The isolates (from nodules of root) were sum up from natural vetch (*Vicia cracca*), yellow melilot (*Melilotus officinalis*) and alfalfa (*Medicago sativa*) plants existing which were previously isolated in the central and the districts of Kırşehir province (Kaman, Mucur, Akpınar, Akçakent, Çiçekdağı, Boztepe), Turkey. The isolates of *Rhizobium* spp. is done on YEMA (Yeast Extract Mannitol Agar) media through streak plate method then plates were incubated at 28°C for 24-72 hours and colony growth

is followed. Single colonies were defined and controlled for purity on YEMA medium [13,14] and colony morphology, Congo red reaction, Gram-stain reaction. Colony property (color, mucosity, borders, transparency and elevation), movement, catalase, oxidase tests and acid / alkaline reaction were evaluated on YMA containing bromthymol blue (0.00125 mg kg⁻¹) as indicator [15]. All of isolates stored at -20°C in 25 % glycerol-YM broth.

2.2. Siderophore production

The experiment reported by Schwyn and Neilands [16] were applied for the qualitative detection of siderophore production (Chrome Azurol S Dye (CAS) Agar) in different strains. A loop was obtained from 7 day old YMA plaques were infected into the middle of the CAS medium and were incubated for 5-7 days at 30 °C. The colony dia was observed and the halo region formed around the colony was measured as defined by Van-Rossum et al. [8,17].

3. Results and discussion

3.1. Morpho-physiological, biochemical characterization

In this study, it was determined that all of the 56 isolates tested had normal colonies, producing creamy, medium to high mucus. When all 56 samples showing the presence of Rhizobia were subjected to Gram staining all isolates were found to be Gram negative, because the cells appeared pink. After 3 to 5 days of growth at 28°C in YMA, all isolates acidified medium (as shown by bromothymol blue). With respect to biochemical characterization, all the isolates showed positive for catalase and oxidase as reported in the Bergey's Manual Systematic Bacteriology (Table1) [16,17,6,18]. Similarly, Prajapati et al., (2018) reported that *Rhizobium* spp. isolates were positive for oxidase and catalase test [19].

3.2. Production of siderophores

The detection of siderophores utilizing the Chrome Azurol S (CAS) agar plaques was based on capacity of the siderophores to act as chelating agents with changing affinity for iron. Presence of iron chelator is shown by coloring the blue colored ferric CAS complex and this is determined by the formation of an orange halo around the colonies in the CAS plates. In this work, siderophore produce ability of 56 isolates were tested and 50 of them were positive and 6 were negative on CAS agar.

Table 1. Morpho-physiological, biochemical characteristics of *Rhizobium* spp.

Isolate No.	Brom th. blue	Cong o red	Cell mor	Gram react	Move	Catal	Oxid
HR 1	yellow	white	rod	-	+	+	+
HR 2-1	yellow	white	rod	-	+	+	+
HR 2-2	yellow	white	rod	-	+	+	+
HR4	yellow	white	rod	-	+	+	+
HR 7a	yellow	white	rod	-	+	+	+
HR 7b	yellow	white	rod	-	+	+	+
HR 14	yellow	white	rod	-	+	+	+
HR 16-1	yellow	white	rod	-	+	+	+
HR 16-2	yellow	white	rod	-	+	+	+
HR 19	yellow	white	rod	-	+	+	+
HR 28	yellow	white	rod	-	+	+	+
HR 29	yellow	white	rod	-	+	+	+
HR 31	yellow	white	rod	-	+	+	+
HR 33-2a	yellow	white	rod	-	+	+	+
HR 33-2b	yellow	white	rod	-	+	+	+
HR 33-3aA	yellow	white	rod	-	+	+	+
HR 36-1	yellow	white	rod	-	+	+	+
HR 36-2	yellow	white	rod	-	+	+	+
HR 37	yellow	white	rod	-	+	+	+
HR 38-1a	yellow	white	rod	-	+	+	+
HR 38-2	yellow	white	rod	-	+	+	+
HR 40-1a	yellow	white	rod	-	+	+	+
HR 40-1b	yellow	white	rod	-	+	+	+
HR 40-2	yellow	white	rod	-	+	+	+
HR 41-1	yellow	white	rod	-	+	+	+
HR 41-2	yellow	white	rod	-	+	+	+
HR 42	yellow	white	rod	-	+	+	+
HR 43-2	yellow	white	rod	-	+	+	+
HR 45-1	yellow	white	rod	-	+	+	+
HR 48-1	yellow	white	rod	-	+	+	+
HR 48-2	yellow	white	rod	-	+	+	+
HR 49	yellow	white	rod	-	+	+	+
HR 50-1	yellow	white	rod	-	+	+	+
HR 50-2	yellow	white	rod	-	+	+	+
HR 51	yellow	white	rod	-	+	+	+
HR 52-2	yellow	white	rod	-	+	+	+
HR 59-1a	yellow	white	rod	-	+	+	+
HR 59-1b	yellow	white	rod	-	+	+	+
HR 59-2	yellow	white	rod	-	+	+	+
HR 102-1	yellow	white	rod	-	+	+	+
HR 102-2	yellow	white	rod	-	+	+	+
HR 103	yellow	white	rod	-	+	+	+
HR 104-2b	yellow	white	rod	-	+	+	+
HR 105-2	yellow	white	rod	-	+	+	+
HR 106-1	yellow	white	rod	-	+	+	+
HR 106-2	yellow	white	rod	-	+	+	+
HR 107	yellow	white	rod	-	+	+	+
HR 109	yellow	white	rod	-	+	+	+

HR 111	yellow	white	rod	-	+	+	+
HR 123	yellow	white	rod	-	+	+	+
HR 124	yellow	white	rod	-	+	+	+
HR 125	yellow	white	rod	-	+	+	+
HR 132-2a	yellow	white	rod	-	+	+	+
HR 138-1	yellow	white	rod	-	+	+	+
HR 143-1	yellow	white	rod	-	+	+	+
HR 143-2	yellow	white	rod	-	+	+	+

Table 2. Siderophore production (halozone- mm) by different *Rhizobium* spp. on CAS agar plate

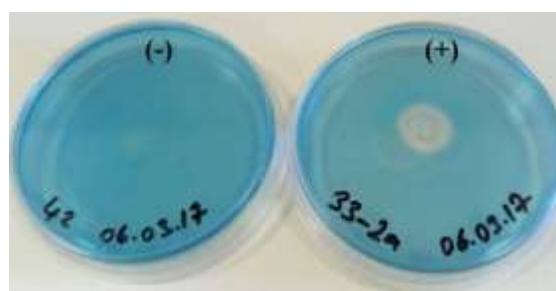
Isolate No	Halozone (mm)	Isolate No	Halozone (mm)
HR 1	12	HR 45-1	9.5
HR 2-1	-	HR 48-1	10.5
HR 2-2	11.5	HR 48-2	-
HR 4	11.5	HR 49	11
HR 7a	10	HR 50-1	12
HR 7b	10	HR 50-2	12.5
HR 14	11	HR 51	10.5
HR 16-1	12	HR 52-2	8.5
HR 16-2	12	HR 59-1a	10.5
HR 19	10	HR 59-1b	12
HR 28	9.5	HR 59-2	11.5
HR 29	9.5	HR 102-1	12
HR 31	12	HR 102-2	11
HR 33-2a	12	HR 103	9
HR 33-2b	10.5	HR 104-2b	-
HR 33-3a A	9	HR 105-2	9
HR 36-1	11.5	HR 106-1	10
HR 36-2	10.5	HR 106-2	10.5
HR 37	9.5	HR 107	11.5
HR 38-1a	11	HR 109	10
HR 38-2	10.5	HR 111	9.5
HR 40-1a	11.5	HR 123	9.5
HR 40-1b	12.5	HR 124	9.5
HR 40-2	10	HR 125	-
HR 41-1	9.5	HR 132-2a	-
HR 41-2	9.5	HR 138-1	10
HR 42	-	HR 143-1	12
HR 43-2	9	HR 143-2	9.5

Table 2 and Figure 1 show the production of siderophore of different *Rhizobium* spp. isolates on CAS agar plates. All isolates were to produce siderophore except for 6 isolates. Isolates HR 2-1, HR 42, HR 48-2, HR 104-2b, HR 125, HR 132-2a have not grown on the CAS agar plates. All of isolates showed ratio between 8.5mm to 12.5mm halo zone area. Similar results have been declared by Dhul et al. [8], Jossi et al. [12] and Harshitha et al. [20] in various *Rhizobium* spp.

4. Conclusions

When the studies carried out in recent years are examined, siderophores attract attention because of the emergence of different application areas (plant growth improvement, biocontrols, biosensors, bioremediation, chelation agents).

The results of this work showed that *Rhizobium* spp. isolated from wild legume plants secrete wide siderophores. The capacity to use siderophores enables natural *Rhizobium* spp. to grow better in iron limited conditions in the presence of those siderophores



(+): Positive controle (halo zone); (-): Negative control (halo zone)

Figure 1. Halo zone production by the isolates in CAS Agar

Acknowledgement

Authors thanks to This work was supported Ahi Evran Univ. BAP No: FEF.B2.16.004.

References

- [1] Teaumroong N., Boonkerd N., Detection of *Bradyrhizobium* spp. and *B. japonicum* in Thailand by primer-based technology and direct DNA extraction. *Plant Soil* 204:127-134, (1998).
- [2] Rigby D., Caceres D., Organic farming and the sustainability of agricultural systems. *Agricultural Systems* 68:21-40. (2001). DOI: 10.1016/S0308-521X(00)00060-3.
- [3] Lee J.Y. and Song S. H., Evaluation of groundwater quality in coastal areas: implications for sustainable agriculture. *Environmental Geology* 52:1231-1242, (2007). DOI: 10.1007/s00254-006-0560-2.
- [4] Ögütçü H., Algur O. F., Elkoca E., Kantar F. The determination of symbiotic effectiveness of *Rhizobium* strains isolated from wild chickpea collected from high altitudes in Erzurum. *Turkish Journal of Agriculture and Forestry* 32:241-248, (2008). DOI: 10.3906/tar-0904-34.
- [5] Zahran H.H., Rhizobia from wild legumes: diversity, taxonomy, ecology, nitrogen fixation and biotechnology. *Journal of Biotechnology* 91:143-

- 153, (2001). DOI: 10.1016/S0168-1656(01)00342-X.
- [6] Ögütçü H., Kasımoğlu C., Elkoca E., Effects of *Rhizobium* strains isolated from wild chickpeas on the growth and symbiotic performance of chickpea (*Cicer arietinum* L.) under salt stress. Turk J Agric For 34: 361-371, (2010). DOI: 10.3906/tar-0904-34.
- [7] Adıgüzel A., Ogutcu H., Baris O., Karadayi M., Gulluce M., Isolation and characterization of *Rhizobium* strains from wild vetch collected from high altitudes in Erzurum-Turkey. Romanian Biotechnological Letters 15(1) : 5017-5024, (2010).
- [8] Dhul M., Suneja S., Dadarwal K. R., Role of siderophores in chickpea (*Cicer arietinum* L.) – *Rhizobium* symbiosis. Microbiol. Res. 153:47-53, (1998). DOI: 10.1016/S0944-5013(98)80020-7.
- [9] Datta B., Chakrabartty P. K., Siderophore biosynthesis genes of *Rhizobium* spp. isolated from *Cicer arietinum* L. 3 Biotech 4:391–401,(2014). DOI 10.1007/s13205-013-0164-y.
- [10] Erdem B., Dayangaç A., Günaydin, M., Tulumoglu S., Yilmaz M., Effect of heavy metals and antibiotics on siderophores producing bacterial isolates. Acta Physica Polonica A 130:181-183, (2016). DOI: 0.12693/APhysPolA.130.181.
- [11] Guerinot M.L., Iron uptake and metabolism in the Rhizobia/ legume symbioses. Plant Soil 130:199–209, (1991).
- [12] Joshi F. R., Kholiya S. P., Archana G., Desai A. J. Siderophore cross-utilization amongst nodule isolates of the cowpea miscellany group and its effect on plant growth in the presence of antagonistic organisms. Microbiological Research 163: 564—570, (2008). DOI: 10.1016/j.micres.2006.08.004.
- [13] Vincent J.M., A Manual for the practical study of root nodule bacteria. Blackwell Scientific, Oxford, (1970).
- [14] Ögütçü H., Adıgüzel A., Güllüce M., Karadayı M., Şahin F. Molecular characterization of *Rhizobium* strains isolated from wild chickpeas collected from high altitudes in Erzurum-Turkey. Romanian Biotechnological Letters 14(2): 4294-4300, (2009).
- [15] Kantar F., Elkoca E., Ögütçü H., Algur Ö. F. Chickpea yields in relation to *Rhizobium* inoculation from wild chickpea at high altitudes. J Agronomy Crop Science 189: 291-297, (2003). DOI: 10.1046/j.1439-037X.2003.00046.x.
- [16] Schwyn B., Neilands J.B., Universal Chemical assay for the detection and determination of siderophores. Analytical Biochemistry 160: 47-56, (1987). DOI:10.1016/0003-2697(87)90612-9.
- [17] Van Rossum D., Muyotcha A., Van Verseveld H.W., Stouthamer A.H., Boogred F. C. Siderophore production by *Bradyrhizobium* spp. strains nodulating groundnut. Plant Soil 163: 177-187, (1994).
- [18] Tyagi A., Kumar V., Tomar P. and A. Isolation, Identification, biochemical and antibiotic sensitivity characterization of *Rhizobium* strains from *Vigna mungo* (L) Hepper, *Cicer arietinum* L. and *Vigna radiata* (L) R Wilczek in Muzaffarnagar, Uttar Pradesh, India. Int. J. Curr. Microbiol. App. Sci 6:2024-2035, (2017). DOI: 0.20546/ijcmas.2017.612.233.
- [19] Prajapati, S., Dadke, M. S., Surekha, S., Godika. and Krishna, V. P., Isolation and characterization of *Rhizobium meliloti* isolated from rhizosphere soil and roots of Fenugreek from different locations. Int. J. Curr. Microbiol. App. Sci., 7(6): 1460-1467, (2018).
- [20] Harshitha, B., A., Goudar, G., Krishnaraj, P. U., and Koti, R. V., Characterization of plant growth promoting rhizobial isolates for pigeon pea (*Cajanus cajan* [L.] Mill sp). Int. J. Curr. Microbiol. App. Sci., 9(7): 3776-3788, (2020). DOI: 10.20546/ijcmas.2020.907.442.



Determination of Liquefaction Resistance and Allowable Bearing Capacity of Soils Based on V_s (Shear wave) velocity; Case Study: Isparta Süleyman Demirel Industrial Region Waste Treatment Facility

Emre TİMUR, Coşkun SARI*

Dokuz Eylül University, Engineering Faculty, Department of Geophysical Engineering, İzmir-Turkey

* Corresponding Author : coskun.sari@deu.edu.tr

ORCID: 0000-0002-0192-9300

Article Info:

DOI: 10.22399/ijcesen.744183

Received : 28 May 2020

Accepted : 17 November 2020

Keywords

Bearing capacity
Liquefaction analysis
Seismic refraction
Isparta

Abstract:

It was a very common procedure to investigate liquefaction risk with standard penetration test (SPT). However, this method has been lost its importance after the developments of conic penetration method in 1971, Becker penetration method and S-wave velocity measurements. S-wave velocity measurements could be very reasonable alternatives in order to carry out penetration tests for the gravelly and unconsolidated overburden soil investigations. In this study, S-wave velocity values were used in order to determine liquefaction resistance and allowable bearing capacity of soil where two different methods were applied to S-wave velocity values and the results were also compared. All the application steps of the methods were defined. Data were collected along 4 profiles for the ground investigations carried out for the Isparta Süleyman Demirel Industrial Region Waste Treatment Facility.

1. Introduction

Soil liquefaction defines an event where a saturated or partially saturated soil layer suddenly loses strength in response to an applied stress. Generally the reason of the stress is a earthquake shaking which forces the layer to behave like a liquid. This behaviour of the ground causes the buildings to lean to one side or a total collapse. Consequently liquefaction analyses of the shallow layers are very important on ground investigations.

Determination of the liquefaction resistance of layers is an important feature in geotechnical explorations especially in seismically risky areas. First procedure was developed by [1] using the data from the standard penetration test (SPT) correlated with a parameter called the cyclic stress ratio. This procedure has been revised and updated by several geotechnicians in time [2, 3, 4, 5, 6, 7]. Another method based on the cone penetration test (CPT) was developed by [8] in 1985 which also has been examined and updated [9, 10, 11, 12, 13].

The use of S-wave (V_s) velocity as an index of liquefaction resistance is soundly based because both S-wave velocity liquefaction resistances are similarly influenced by many factors. Some advantages of using S-wave velocity [14, 15, 16, 17] are that (1) the measurements are possible in soils that are hard to sample, such as gravelly soils where penetration tests may be unreliable; (2) measurements can also be performed on small laboratory specimens, allowing direct comparisons between laboratory and field behaviour; (3) S-wave velocity is a basic mechanical property of soil materials, directly related to small stress-strain shear modulus G_{max} given by $G_{max} = \rho V_s^2$ where ρ is the mass density of soil, V_s is the S-wave velocity; (4) G_{max} or V_s is normally a required property in earthquake site response and soil-structure interaction analyses; and (5) S-wave velocity can be measured by the spectral analysis of surface waves (SASW) or multichannel analysis of surface waves (MASW) techniques at sites where borings may not be permitted.

Three concerns when using S-wave velocity to evaluate liquefaction resistance are that (1) no samples are routinely obtained as a part of the testing procedure for soil classification and identification of nonliquefiable materials; (2) thin, low S-wave velocity strata may not be detected if the measurement interval is too large; and (3) measurements are made at small strains, whereas pore water pressure buildup and liquefaction are medium to high strain phenomena [18, 19, 20].

Secondly, the ultimate bearing capacity of a particular soil, under a shallow footing, was investigated theoretically by Prandtl [21] and Reissner [22] using the concept of plastic equilibrium as early as in 1921. The formulation however is slightly modified, generalized, and updated later by Meyerhof [23], Hansen [24], De Beer [25], and Sieffert et al. [26].

S-wave velocity surveys, represent the actual ground conditions, are much more efficient and reliable than the shear strength parameters measured in laboratory. In addition to seismic refraction survey, there are several other techniques of measuring V_S at the investigation site as defined by Stokoe and Woods [27] and updated by Tezcan et al. [28]. The reason is in-situ measured S-wave velocity indicates the actual unchanged condition of the soil layers. V_S also enables the observer to determine the allowable bearing capacity (q_a), which is also an important parameter for defining ground conditions, in a reliable way.

In this study, it was intended to observe the ground condition using seismic refraction surveys in Isparta/Turkey. Data were collected along 4 profiles and procedures of liquefaction analysis and allowable bearing capacity were applied in order to determine risky soil layers.

2. Evaluation Procedure of Liquefaction Analysis

The evaluation procedure of determination of liquefaction resistance requires the calculation of three parameters; (1) The level of cyclic loading on the soil caused by the earthquake, expressed as a cyclic stress ratio (CSR) [1, 2] (Figure 1); (2) stiffness of the soil, expressed as an overburden stress-corrected shear wave velocity [3, 29, 30, 31]; and (3) resistance of the soil to liquefaction, expressed as a cyclic resistance ratio (CRR) [1, 3, 32, 33].

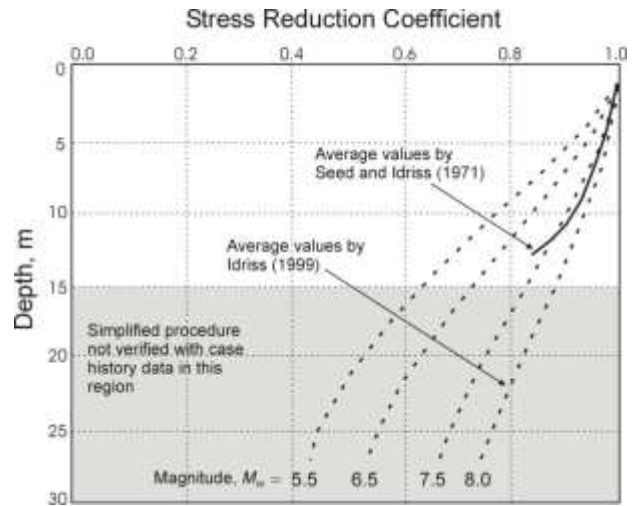


Figure 1. Shear Stress Reduction Factor used to adjust for flexibility in soil profiles during earthquake shaking [2].

The correction factor (K_c) is needed for high values of V_{S1} caused by cementation and aging. Figure 2 illustrates a method for estimating the value of K_c by using SPT blow counts. Figure 2a indicates the V_{S1} - $(N_1)_{60}$ correlation between silty sands implied by the recommended CRR- V_{S1} curves and CRR- $(N_1)_{60}$ curves [34]. The theoretical curves presented in Figure 2b were improved from them [3].

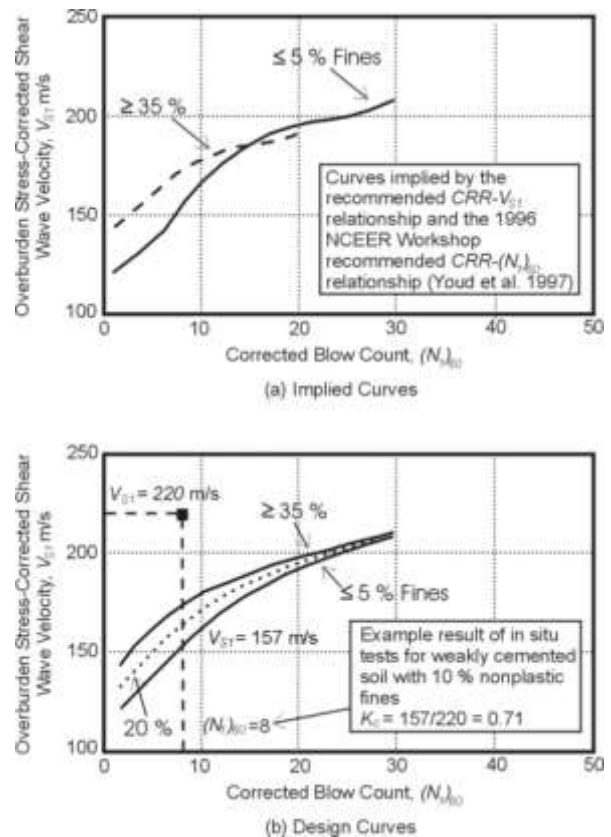


Figure 2. Correlations between V_{S1} and $(N_1)_{60}$ and an example for determining correction factor K_c [3].

In soils above the ground-water table, especially silty soils, negative pore pressures increase the effective state of stress and this effect should be considered in the estimation of σ'_v for correcting V_S and V_{S1} . The entire procedure is generally summarized in several steps in [3].

3. Evaluation Procedure of Allowable Bearing Capacity

The allowable bearing capacity, considering the limits for the parameters [35], can be calculated from the statements proposed by [34]. The change in allowable bearing capacity q_a , with respect to S-wave velocity V_S , is presented in Figure 3.

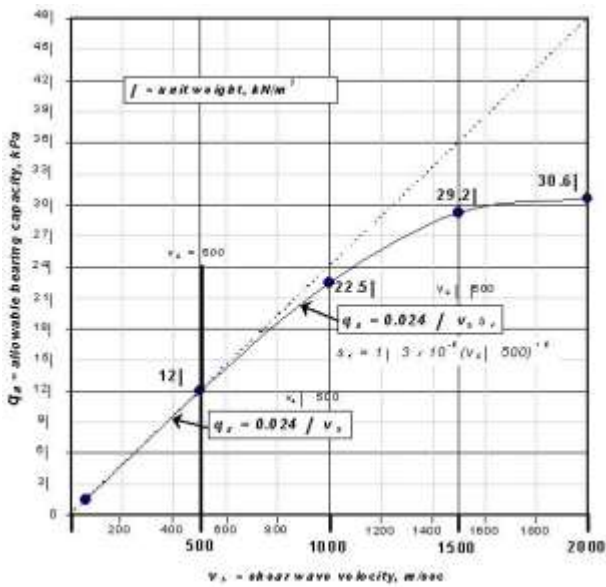


Figure 3. Allowable bearing capacity of soils based on S-wave velocity [41].

The P-wave velocity of a layer is influenced directly from the average unit weight γ . According to previous studies on this relationship, a corrected unit weight should be calculated by adding the effect of V_P [34, 36]. Also it can be clearly seen that the calculated unit weights are in consistency with the values measured in the laboratory (Figure 4).

4. Location and Geology of the Field

The survey area is located in the intersection point of the western and middle Taurus Mountains, near the Lakes (Göller) District of Turkey (Figure 5). The study area is located in the Gümüşgün resort in city of Isparta, on the crossroad of Ankara, Antalya and İzmir. It is 26 km from Isparta and 4 km from the local airport. It is planned to refine 4000-8000 m³ contaminated water each day in the purification site.

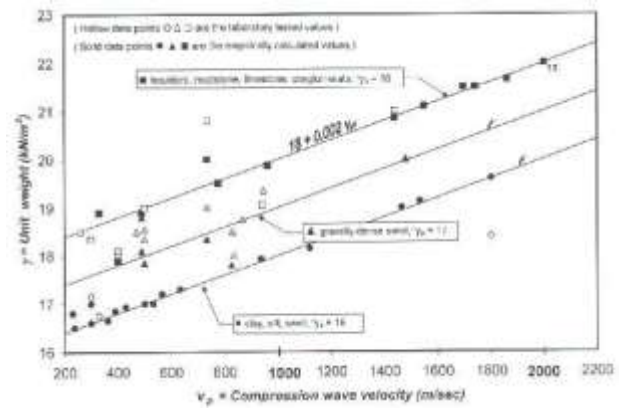


Figure 4. Unit weights based on S-wave velocities [34].

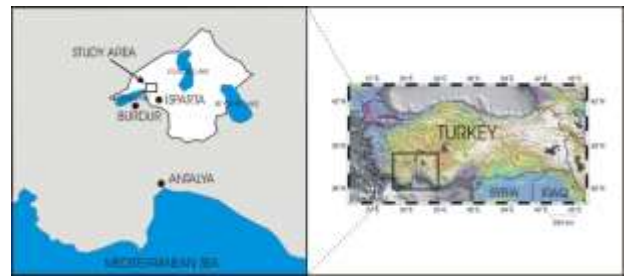


Figure 5. Location of the survey area.

This area is defined by the rocks of Miocene, Pliocene and Pleistocene in age at the higher reliefs. High altitude areas, where this system exists, are broken apart in several levels by the faults and rivers. Water drainage system of the area was usually presented in the Pliocene. This system which is well adjusted with the orogenic and structural features and connected with the closed basin is partially preserved nearby the northern and north-western part (Göller Region) of the survey area (Figure 6).

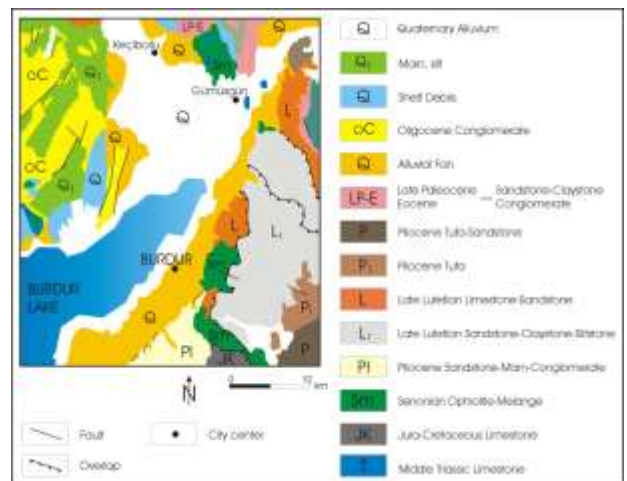


Figure 6. Geological map of the survey area.

5. The Principles of Seismic Near-Surface Investigations

It is hereby the traditional seismic refraction technique was applied for the geotechnical engineering purposes. Shallow refraction technique is considered as one of the most effective method, which can be used, for the engineering purposes. Determining depth to the bedrock, the depth to groundwater, types of lithology, the lateral and vertical changes in lithology and investigating structural features such as micro faults and cracks are the main targets of shallow refraction applications.

Traditional interpretation of seismic refraction data has used a concept of layered horizons or zones where each horizon has a discrete seismic velocity. Interpretation methods based on the refraction of the first portion of the seismic wave have been known for many years [37]. The advent of hand-held calculators in the 1970's and personal computers by the 1980's, as well as the development of practical seismographs for civil engineering use, has made seismic refraction a practical geotechnical exploration tool for more than two decades.

The seismic refraction method consists of measuring (at known points along the surface of the ground) the travel times of seismic waves either P- or S-wave velocities generated by an impulsive energy source. The energy is detected, amplified and recorded by special equipments (seismographs).

At the seismic refraction study, data acquisition was designed to make effective use of the advanced data processing techniques. The seismic field data were collected using a 12 channel named PASI (Italy) engineering seismograph for refraction investigation. Each seismic refraction spread (profile) consists of a series of 12 channel geophones placed along the line at a set distance or geophone interval. 14 Hz geophones were used. The average shot spacing (a sledge hammer of 8 kg as a surface impact source) was about 1-10 meter length. Generally, for shallow depth investigation the sledgehammer is suitable because it is easy to operate, cheap, highly portable and safe. In case of soft ground, an impact plate firmly embedded in the ground is usually used. The locations of the refraction lines are displayed in Figure 7. The geophones were spaced at 3 m interval with a 3 m nearest offset from the source.

6. Application of Liquefaction Resistance Analysis

The procedure of liquefaction resistance analysis is given by [3] as below:

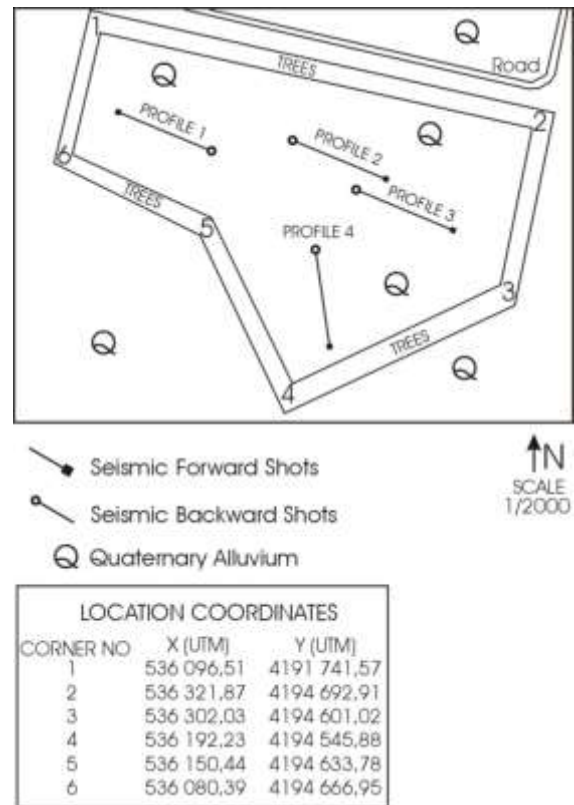


Figure 7. Locations of the seismic profiles and drillings.

1. Determination of S-wave velocity, fines content, densities (Table 1) and penetration resistance (if possible). Densities were calculated with the equation of Gardner et al. [38] $\rho = 0.31V_p^{0.25}$.

Table 1. S-wave velocities, fines contents and densities of layers

		V_s (m/sn)	Fines Content	ρ gr/cm ³
Profile 1	1. Layer	121,24	FC ≥ 35%	1,30
	2. Layer	222,27	FC ≥ 35%	1,48
	3. Layer	425,35	FC ≥ 35%	1,69
Profile 2	1. Layer	134,56	FC ≥ 35%	1,26
	2. Layer	231,08	FC ≥ 35%	1,46
	3. Layer	464,74	FC ≥ 35%	1,82
Profile 3	1. Layer	134,04	FC ≥ 35%	1,22
	2. Layer	249,62	FC ≥ 35%	1,45
	3. Layer	347,71	FC ≥ 35%	1,78
Profile 4	1. Layer	113,8	FC ≥ 35%	1,26
	2. Layer	251,58	FC ≥ 35%	1,45
	3. Layer	498,53	FC ≥ 35%	1,80

2. Determination of water table, besides nothing of seasonal differences and pressures of artesian wells. As a result of insufficient data of water table, water level is assumed to be at the surface.
3. Determination of σ_v in all depths from the seismic data.

$$\begin{aligned}\sigma_V &= \gamma \cdot z \\ \sigma'_V &= \sigma_V - u \quad (1) \\ u &= \gamma_d \cdot z\end{aligned}$$

where z is the liquefaction depth, γ is the density, u is the pore water pressure, σ'_V is the initial effective vertical (overburden) stress at the depth in question, σ_V is the total overburden stress at the same depth [39]. Vertical stresses can be calculated from these equations (Table 2). However it could also be better to use the penetration tests to achieve better results, if possible.

Table 2. Calculated vertical stresses.

		σ_V (kg/cm ²)	σ'_V (kg/cm ²)
Profile 1	1. Layer	0,239	0,101
	2. Layer	1,065	0,444
	3. Layer	1,858	0,785
Profile 2	1. Layer	0,298	0,126
	2. Layer	1,260	0,53
	3. Layer	2,002	0,844
Profile 3	1. Layer	0,169	0,076
	2. Layer	1,001	0,451
	3. Layer	1,942	0,884
Profile 4	1. Layer	0,184	0,078
	2. Layer	1,045	0,456
	3. Layer	1,942	0,86

4. Correction of S-wave velocity measurements with C_V stress parameter. This parameter is accepted as 1.4 for surface layers.

$$V_{S1} = V_S C_V = V_S \left(\frac{P_a}{\sigma'_V} \right)^{0.25} \quad (2)$$

where $P_a = 100 \text{ kPa}$

for profile 1 and layer 2,

$$\sigma'_V = 1.065 \text{ kg/cm}^2 = 104.4408 \text{ kPa}$$

$$V_{S1} = 222.27 \times (100/104.4408)^{0.25} = 219.87 \text{ m/s}$$

All of the values are calculated in Table 3.

5. Determination of V_{S1}^* according to fines content. If fines content is not known than it is assumed to be 215 m/s. Fines content is greater than 35% in all layers ($FC \geq 35\%$). Thus $V_{S1}^* = 200 \text{ m/s}$.

Table 3. C_V and V_{S1} values.

		V_S	σ_V (kg/cm ²)	σ'_V (kPa)	C_V	V_{S1}
Profile 1	1. Layer	121,2	0,23	23,43	1,4	169,7
	2. Layer	222,2	1,06	104,44	0,99	219,8
	3. Layer	425,3	1,85	182,20	0,9	382,8
Profile 2	1. Layer	134,5	0,29	29,22	1,4	188,3
	2. Layer	231,0	1,26	123,56	0,94	219,1
	3. Layer	464,7	2,00	196,32	0,9	418,2
Profile 3	1. Layer	134,0	0,16	16,57	1,4	187,6
	2. Layer	249,6	1,00	98,16	1,0	250,7
	3. Layer	347,7	1,94	190,44	0,9	312,9
Profile 4	1. Layer	113,8	0,18	18,04	1,4	159,3
	2. Layer	251,5	1,04	102,47	0,99	250,0
	3. Layer	498,5	1,94	190,44	0,9	448,6

6. Determination of K_c . If the soil is uncemented and <10.000 years old, than it is 1. If the condition is not known than it is 0.6 (Table 4).

If there is an abnormal increase in V_S of the third layer it makes appropriate to apply K_c correction. Also it is known that the bottom layers are of the Pliocene.

Table 4. K_c , age corrected velocities and CRR values

		K_C	V_{S1age}	CRR
Profile 1	1. Layer	-	-	-
	2. Layer	0,8	175,896	0,143183
	3. Layer	0,7	267,9705	0,117173
Profile 2	1. Layer	-	-	-
	2. Layer	0,75	164,3807	0,141423
	3. Layer	0,7	292,7862	0,164634
Profile 3	1. Layer	-	-	-
	2. Layer	0,75	188,084	0,340638
	3. Layer	0,75	234,7043	0,030219
Profile 4	1. Layer	-	-	-
	2. Layer	0,75	187,5332	0,328283
	3. Layer	0,65	291,6401	0,162523

7. Determination of earthquake plan and estimation of a_{max} .

Although a_{max} is not known it is possible to estimate a value from Esteva's maximum horizontal ground surface acceleration diagram (Figure 8).

It is assumed that the magnitude is 7.0, and also the seismic risk is assumed as maximum so epicenter distance is taken 0.

$$\text{So } a_{max} = 532.2 \text{ cm/s}^2.$$

$$a_{max} = 532,2 \text{ cm/s}^2 = 5,322 \text{ m/s}^2 = 0,543 \text{ g} \Rightarrow M_w = 7.0$$

8. Determination of CSR of all layers under the water table.

r_d can be calculated from the figure of [1] (Figure 1).

$$CSR = 0.65(\alpha_{max}/g)(\sigma_v/\sigma_v')r_d$$

As an example for Profile 1 and 1. Layer; for 1.38 m $r_d=0.98$ (from Figure 8).

$CSR = 0.65(5.322/9.81)(0.239/0.101)0.98 = 0,8185$ can be found. Table 5 indicates all the profiles and layers.

Table 5. r_d and CSR values.

		r_d	CSR
Profile 1	1. Layer	0,98	0,8185
	2. Layer	0,90	0,7619
	3. Layer	0,80	0,6683
Profile 2	1. Layer	0,96	0,8014
	2. Layer	0,88	0,7384
	3. Layer	0,76	0,6363
Profile 3	1. Layer	0,99	0,7770
	2. Layer	0,91	0,7129
	3. Layer	0,79	0,6125
Profile 4	1. Layer	0,97	0,8076
	2. Layer	0,89	0,7199
	3. Layer	0,78	0,6217

9. Calculating (Table 6) and plotting V_{S1} and CRR liquefaction resistance curves (Figure 9).

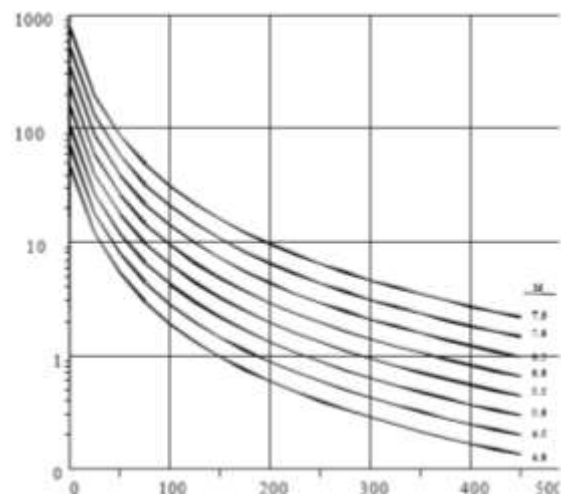
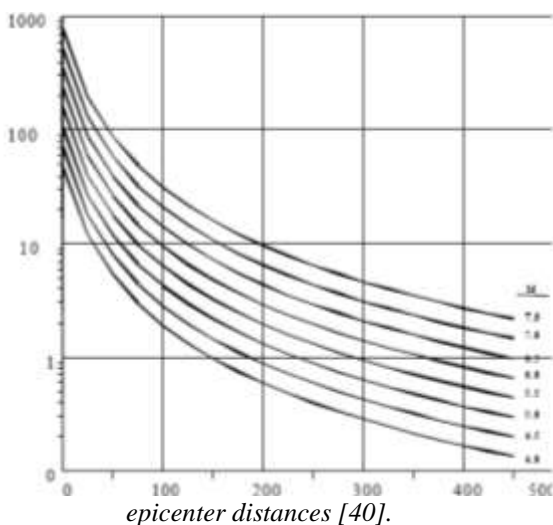
Table 6. CRR values.

		V_S	V_{S1}	V_{S1age}	CRR
Profile 1	1. Layer	121,24	169,736	No Correction	0,161768
	2. Layer	222,27	219,87	175,896	0,143183
	3. Layer	425,35	382,815	267,9705	0,117173
Profile 2	1. Layer	134,56	188,384	No Correction	0,347839
	2. Layer	231,08	219,1743	164,3807	0,141423
	3. Layer	464,74	418,266	292,7862	0,164634
Profile 3	1. Layer	134,04	187,656	No Correction	0,330946
	2. Layer	249,62	250,7787	188,084	0,340638
	3. Layer	347,71	312,939	234,7043	0,030219
Profile 4	1. Layer	113,8	159,32	No Correction	0,126166
	2. Layer	251,58	250,0442	187,5332	0,328283
	3. Layer	498,53	448,677	291,6401	0,162523

10. Determination of FS. If $FS > 1$ than there is no liquefaction, if $FS \leq 1$ than there is liquefaction.

FS is less than 1 in first layers of profile 1 and 4, and second layer of Profile 2. So liquefaction risk is unimportant.

Figure 8. Esteva's maximum acceleration diagram for



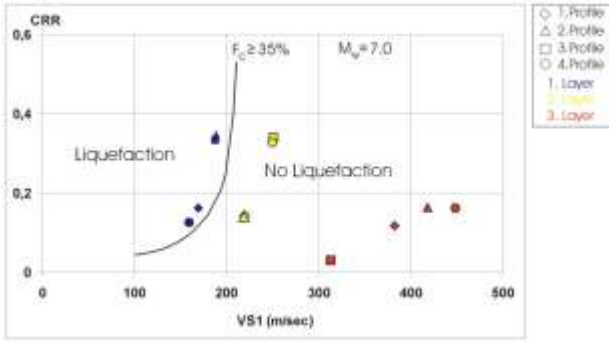


Figure 9. Liquefaction result curve for the study field.

7. Application of Bearing Capacity Analysis

The allowable bearing capacity, q_a , under a shallow foundation in units of kPa, may be obtained from the following empirical expressions:

$$\begin{aligned}
 q_a &= 0.024\gamma V_s \\
 q_a &= 2.4(10^{-4})\rho V_s^2
 \end{aligned}
 \tag{3}$$

where γ is the unit weight (kN/m^3), ρ is the mass density (kg/m^3), and V_s is the shear(S-) wave velocity (m/sec). There is a direct relationship between the average unit weight γ , and the P-wave velocity of a soil layer. Based on extensive case histories of laboratory testing, a convenient empirical relationship in this regard, is proposed in detail by [36] as follows;

$$\gamma_p = \gamma_0 + 0.002V_p \tag{4}$$

P- and S- wave velocity values of the media were obtained from the refraction seismic data of 4 profiles carried out at the survey area using the 12 channel PASI (Italy) seismic refraction equipment. Seismic velocities vary as 235-311 m/s, 477-532 m/s and 893-1184 m/s for the top, middle and bottom layers respectively for the P-wave, whereas these vary as 113-134 m/s, 222-251 m/s and 347-498 m/s for the S-wave. All the layers have very close velocity values within themselves. This signifies that these layers have homogeneous lithologies. Equations 3 and 4 were used in order to calculate the unit weights and allowable bearing capacities of the layers in the survey area. Obtained results were given in Table 7. Since S-wave velocity is less than 500 m/s, equation 3 was used for the allowable bearing capacity calculations. The graphics of the obtained allowable bearing capacity, q_a – S-wave velocity, S-wave velocities were given in Figure 10. As it was observed in the q_a - S-wave velocity profile, the allowable bearing capacity q_a Show s linear variation with the shear wave velocity, S-wave velocity and this is increased with depth.

Table 7. Unit weights and allowable bearing capacities of the layers in the survey area.

		V_S (m/sec)	V_P (m/sec)	Unit Weight (kN/m^3)	Allowable Bearing Capacity, (kPA)
Profile 1	1. Layer	121	311	16.62	48.27
	2. Layer	222	532	17.06	90.91
	3. Layer	425	893	17.78	181.41
Profile 2	1. Layer	135	276.5	16.55	53.63
	2. Layer	231	497	16.99	94.21
	3. Layer	465	1185	18.3	205.00
Profile 3	1. Layer	134	235	16.47	52.96
	2. Layer	250	478	16.95	101.73
	3. Layer	348	1088	18.17	151.80
Profile 4	1. Layer	114	276	16.55	45.28
	2. Layer	252	479	16.95	102.56
	3. Layer	499	1143	18.28	218.99

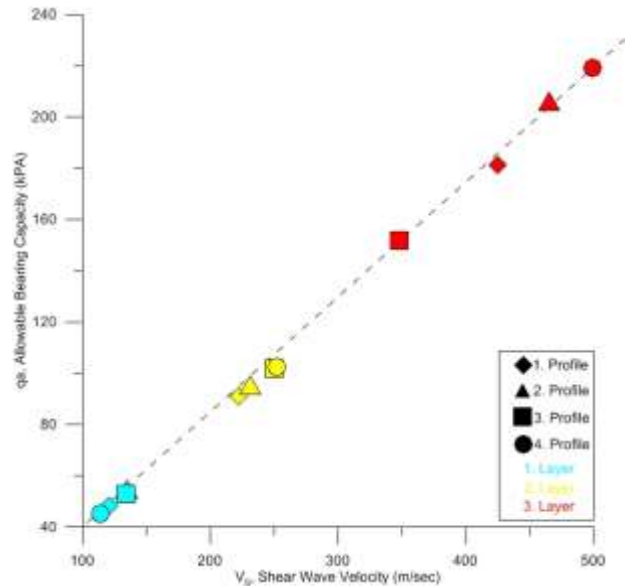


Figure 10. Allowable bearing capacity of soils based on S-wave velocity.

8. Conclusion

In-situ seismic refraction studies were carried out in order to determine liquefaction risk in Isparta Industrial Region Waste Treatment Facility. Seismic P-wave and S-wave velocities were defined to calculate liquefaction resistance and allowable bearing capacity parameters. According to Figure 9, it was observed that all of the first layers of the refraction models have liquefaction risk. Besides the variation of S-wave values between 114-135 m/sec

can be concerned with the relationship between liquefaction risk and S-wave velocity values. Climatic changes and annual average rain amounts should also be considered while determining the liquefaction risk of these first layers. Although a measurement value is in the liquefaction zone on the Nomogram, it was determined that there is no liquefaction risk if CRR value is more than 0.2 in silty and clayed medium. As a result, there is no liquefaction risk for the data which are in the liquefaction zone and have a CRR value greater than 0.2 at the same time in Figure 9. Also first layers of profiles 1 and 4 have less allowable bearing capacity than other two profiles' first layers. So it can be said that allowable bearing capacity and liquefaction analyse result support each other. Risky areas should be considered during the construction of the buildings by choosing appropriate foundation type and possible excavation areas.

Acknowledgements

The authors are grateful to Sumet Ltd. Co. in İzmir for permission of the seismic refraction data.

References

- [1] Seed H.B., I.M.Idriss "Simplified procedure for evaluating soil liquefaction potential" J. Soil Mech. and Found. Div. 97(9) (1971) 1249-1273
- [2] Andrus R.D., P.Paramanathan, S.E. Brian, Z. Jianfeng, J.C.Hsein "Comparing liquefaction evaluation methods using penetration- V_s relationships" Soil Dynamics and Earthquake Engineering. 24 (2004) 713-721
- [3] Andrus R.D., K.H.Stokoe "Liquefaction resistance of soils from shear-wave velocity" Journal of Geotechnical and Geoenvironmental Engineering. ASCE 126(11) (2000) 1015-1025
- [4] Seed H.B. "Soil liquefaction and cyclic mobility evaluation for level ground during earthquakes" Journal of the Geotechnical Engineering Division. ASCE 105(GT2) (1979) 201-255
- [5] Seed H.B., I.M.Idriss, Ground motions and soil liquefaction during earthquakes. Earthquake Engineering Research Institute Monograph, Oakland, California (1982)
- [6] Seed H.B., K.Tokimatsu, L.F.Harder, R.M.Chung "The influence of SPT procedures in soil liquefaction resistance evaluations" J. Geotech. Eng. ASCE 111(12) (1985) 1425-1445
- [7] Youd T.L., R.E.Kayen, J.K.Mitchell "Liquefaction criteria based on energy content of seismograms", Proc. NCEER Workshop on Evaluation of Liquefaction resistance of Soils, Nat. Ctr. for Earthquake Eng. Res., State Univ. of New York at Buffalo, pp. 217-224 (1997)
- [8] Robertson P.K., R.G.Campanella "Liquefaction potential in sands using the CPT" Journal of the Geotechnical Engineering Division. ASCE 111(3) 384-403 (1985)
- [9] Olsen R.S. "Cyclic liquefaction based on the cone penetration test", Proc. NCEER Workshop on Evaluation of Liquefaction Resistance of Soils. Nat. Ctr. for Earthquake Eng. Res., State University of New York at Buffalo, pp. 225-276 (1997)
- [10] Robertson P.K., C.E.Wride "Evaluating cyclic liquefaction potential using cone penetration test" Can. Geotech. J. 35(3) (1998) 442-459
- [11] Seed H.B., P.De Alba "Use of SPT and CPT tests for evaluating the liquefaction resistance of sands" SP Clemence Proceedings, in situ'86 Virginia Tech, Blacksburg, pp. 281-302 (1986)
- [12] Stark T.D., S.M.Olson "Liquefaction resistance using CPT and field case histories" J. Geotech. Eng. ASCE 121(12) (1995) 856-869
- [13] Youd T.L. "Liquefaction Resistance of Soils: Summary Report from The 1996 NCEER and 1998 NCEER/NSF Workshop on Evaluation of Liquefaction Resistance of Soils" J. Geotech. Geonviron. Eng., ASCE 127(10) (2001) 817-833
- [14] Dobry R., K.H.Stokoe II, R.S.Ladd, T.L.Youd "Liquefaction susceptibility from S-wave velocity. In situ testing to evaluate liquefaction susceptibility" ASCE, Geotechnical Engineering Division, New York, (1981) 1-15
- [15] Seed H.B., I.M.Idriss, I.Arango "Evaluation of liquefaction potential using field performance data" Journal of the Geotechnical Engineering Division. 109(3) (1983) 458-482
- [16] Stokoe K.H., S.Nazarian, G.J.Rix, I.Sanchez-Salinaro, J.C.Sheu, et al. "In situ seismic testing of hard to sample soils by surface wave method" In: Von Thun, J.L. (ed.) Earthquake Engineering and Soil Dynamics II-Recent advances in ground motion evaluation. Geotechnical Special Publication 20 Park City, Utah, pp. 264-278 (1988)
- [17] Tokimatsu K., A.Uchida "Correlation between liquefaction resistance and shear wave velocity" Soils and Found. 30(2) (1990) 33-42
- [18] Jamiolkowski M., D.C.F.Lo Presti "Correlation between liquefaction resistance and shear wave velocity" Soils and Found. 32(2) (1990) 145-148
- [19] Roy D., R.G.Campanella, P.M.Byrne, J.M.O. Hughes "Strain level and uncertainty of liquifaction related index tests" In: Shackelford, C.D., Nelson, P.P., Roth, M.J.S. (eds.) Uncertainty in the geologic environment: From theory to practice. Geotech. Spec. Publ. No: 58(2), ASCE New York, pp. 1149-1162 (1996)
- [20] Teachavorasinskun S., F.Tasuoka, D.C.F.Lo Presti "Effects of the cyclic prestaining on dilatancy characteristics and liquefaction strength of sand" In: Shibuya, S., Mitachi, T., Miura, S. (eds.) Pre-failure deformation of geomaterials, Balkema, Rotterdam, The Netherlands, pp. 75-80 (1994)
- [21] Prandtl L. Über die Eindringungsfestigkeit (Härte) plastischer Baustoffe und die Festigkeit von Schneiden. (On the penetrating strengths (hardness) of plastic construction materials and the strength of cutting edges). Zeit. Angew. Math. Mech. 1(1) 15-20 (1921)

- [22] Reissner H. "Zum Erddruckproblem" (Concerning the earth-pressure problem). Proc. 1st Int. Congress of Applied Mechanics. Delft, pp. 295-311 (1924)
- [23] Meyerhof G.G. "Penetration tests and bearing capacity of cohesionless soils" Proceedings ASCE, 82(SM1) pp. 1-19 (1956)
- [24] Hansen J.B. "A revised extended formula for bearing capacity" Danish Geotechnical Institute Bulletin. 28 (1968)
- [25] DeBeer E.E. "Experimental determination of the shape factors and the bearing capacity factors of sand" Geotechnique. 20 (1970) 387-411
- [26] Sieffert J.G., Ch Bay-Gress. "Comparison of the European bearing capacity calculation methods for shallow foundations" Geotechnical Engineering Institution of Civil Engineers. 143 (2000) 65-74
- [27] Stokoe K.H., R.D.Woods "Insitu shear wave velocity by cross-hole method" Journal of the Soil Mechanics and Foundation Divison, ASCE. 98(SM5) (1972) 443-460
- [28] Tezcan S.S., S.M.Erden, H.T.Durgunoğlu "Insitu measurement of shear wave velocity at Bosphorus (Boğaziçi) University Campus" Proceedings of the International Conference on Soil Mechanics and Foundation Engineering, Istanbul Technical University, Istanbul, 2 pp. 157-164 (1975)
- [29] Belloti R., J.Jamiolkowski, D.C.F.Lo Presti, , D.A.O'Neill "Anisotropy of small strain stiffness of Ticino sand" Geotechnique. 46(1) (1996) 115-131
- [30] Roesler S.K. "Anisotropic shear modulus due to stress anisotropy" Journal of the Geotechnical Engineering Division. ASCE 105(7) (1979) 871-880
- [31] Stokoe K.H., S.H.H.Lee, D.P.Knox "Shear moduli measurements under true triaxial stresses" Proc. Adv. in the Art of Testing Soil Under Cyclic Conditions. ASCE, New York, pp. 166-185 (1985)
- [32] Dobry R. "Some Basic aspects of soil liquefaction during earthquakes" Earthquake hazards and the design of constructed facilities in the eastern United States. In: Jacob, K.H., Turkstra, C.J. (eds.) Ann. of the New York Acad. of Sci., New York, 558 172-182 (1989)
- [33] Idriss I.M. "Presentation notes: An update of Seed-Idriss Simplified Procedure for Evaluating Liquefaction Potential" Proc. TRB Workshop on New Approaches to Liquefaction Anal. Publ. No. FHWA-RD-99-165. Washington DC Federal Highway Administration (1999)
- [34] Tezcan S.S., Z.Özdemir, A.Keçeli "Allowable Bearing Capacity of Shallow Foundations Based on Shear Wave Velocity". Geotechnical and Geological Engineering. CV-338 24 (2006) 203-218
- [35] Skempton A.W., D.H.MacDonald "Allowable settlement of buildings" Proceedings ICE, 5(3) pp. 727-768 (1956)
- [36] Tezcan S.S., Z.Özdemir, A.Keçeli, A.Erkali "A rapid technique to determine allowable bearing pressure" International Earthquake Symposium, Kocaeli pp. 234-241 (2007)
- [37] Jakosky J.J. "Exploration Geophysics" Time-Mirrors Press, Los Angeles (1940)
- [38] Gardner G.H.F., L.W.Garner, A.R.Gregory "Formation velocity and density-the diagnostic basics for stratigraphic traps" Geophysics. 39(6) (1974) 770-780
- [39] Yılmaz H.R. "Ground Mechanics-1 Lecture Notes" Aegean University Engineering Faculty Department of Civil Engineering. Unpublished (2001)
- [40] Uyanık O., Ph.D. Thesis, The Graduate School of Natural and Applied Sciences, Dokuz Eylül University, İzmir, Kayma Dalga Hızına Bağlı Potansiyel Sıvılaşma Analiz Yöntemi. 2002 (in Turkish).



Virtual Reality Applications in Industrial Automation Systems: Industrial Robot Station Application

Akın ARAS¹, Murat AYAZ^{2*}, Engin ÖZDEMİR³, Nurettin ABUT¹

¹Kocaeli University, Engineering Faculty, Electrical Engineering Department, 41050, Kocaeli-Turkey

²Kocaeli University, Uzunciftlik Nuh Cimento VS, Electric and Energy Department, 41380, Kocaeli-Turkey

³Kocaeli University, Technology Faculty, Energy Systems Engineering Department, 41050, Kocaeli-Turkey

* Corresponding Author : murat.ayaz@kocaeli.edu.tr

ORCID: 0000-0001-9839-3970

Article Info:

DOI: 10.22399/ijcesen.764365

Received : 05 July 2020

Accepted : 19 November 2020

Keywords

Virtual reality
Robotics
Robot programming
Industrial automation systems

Abstract:

Throughout the history of technological development, production is expected to bring more output with less cost perpetually. In order to compete in ever-changing market conditions, it is an inevitable requirement to increase productivity and reduce costs. As a result of the efforts to respond to this need, industrial robots emerged in the production systems. The aim of this contribution is to give a focus on the virtual reality technology usage with offline robot programming and to emphasize its advantages on design, programming and commissioning phases of robotic production lines. This paper presents application of a virtual reality tool in aid of robot programmer in industrial robot station environment. The proposed system aims to provide information in industrial robot station as well as to enhance the robot programmer concentration in the safety mechanisms in industrial workspace. The proposed virtual reality application in industrial robot station has been applied to a case study from the automation sector, resulting in enhanced robot programmer integration with the industrial environment.

1. Introduction

Industrial robots are basically designed to take people's places in the routine work that people do and increase productivity. The main advantages such as the ability of working under heavy weights, speed, high quality and long working times as long as periodic maintenance is done correctly, have made it possible for them to rapidly increase their usage areas in the industry. The robots have found a wide usage area in a variety of sectors in our country and in the world. In automotive sector such as welding, paint, assembly, quality control; in FMCG sector such as production, packaging, quality control and similar fields in pharmaceutical sector are also examples of this.

With offline robot programming, robotic production lines can be designed and simulated before the line is physically established. [1] In this way, the design errors and the improvement opportunities can be

observed before making any investment. Besides, offline robot programming can be used as an effective training tool for maintenance people and students. When the online robot programming method was used in the past, the robot and so the production had to be stopped for a long time. In offline robot programming, robotic production lines can be designed, programmed, and simulated in a computer in the office environment. Today, robotic production lines are first designed and programmed in the computer environment, then the line is physically installed and the robot programs are fine-tuned. In actively working production lines, cycle time improvement projects are designed, programmed and simulated in the office environment without stopping the production for a long time, and then the improved program can be commissioned during scheduled maintenance periods.

In the literature search for offline robot programming, the use of ABB RobotStudio software

for offline robot programming [2-6], arc welding application in RobotStudio software [7], palletizing application in RobotStudio software [8], an application with an imported CAD model into RobotStudio software [9] were observed. In the literature search for virtual reality technology, a study on historical development of virtual reality [10], application fields of virtual reality [11], virtual reality applications in education sector [12-14], virtual reality applications in tourism sector [15], virtual reality applications in clinical therapy [16], comparison of virtual reality and augmented reality in technological aspect [17-18] were observed.

This study aims to examine the use of virtual reality technology in order to improve the design and programming processes of robotic production lines in terms of time, cost and work safety. In this context, in the first part of this study, the use of ABB RobotStudio software was examined, and then gripper robot application, which is used extensively in the automotive sector, was programmed and simulated. In the last part of the study, the simulation prepared in RobotStudio software was experienced with HTC Vive virtual reality system and the results were shared.

2. ABB RobotStudio

RobotStudio is software developed by ABB and is used for offline programming and simulating of robot stations. Its main advantages can be defined as follows:

- ✓ The behavior of the system can be observed by designing the station in the virtual environment before physically installing it and the system can be optimized in this stage.
- ✓ In cycle time improvement projects for production lines, program improvements can be done offline in the office environment without stopping the production.
- ✓ Technical skills such as the design of the robot station, programming of the robot, etc. can be achieved by project and maintenance teams with securing work safety and gaining experimentation as much as desired.

In order to experience the virtual reality technology with offline robot programming, a gripper robot application was designed and simulated in ABB RobotStudio. The aim of choosing gripper robot application is that it has a wide usage area in automotive and many other industries.

2.1 Gripper robot application

Gripper is a tool that is simply used to move a part from a place to another place. This is widely used in production lines, warehouses, logistics, etc. In order to design, program and simulate a gripper robot application, the process steps are defined as below respectively:

- Creating a station
- Adding a robot and setting up its system
- Designing a gripper and defining it as a mechanism
- Designing a table with suitable dimensions
- Designing the work piece to be gripped
- Adding the Smart Components
- Adding the necessary I/O signals in the robot system
- Configuring the Station Logic
- Defining the robot's path
- Program code writing in RAPID
- Simulating the program

In the sample application, an empty station was created and then IRB 140 model robot has been added in the station. After that, a system was installed in the robot. In order to utilize in the program, a PROFIBUS device has been selected in system configuration as well.

2.2 Designing a gripper and defining it as a mechanism

To design the gripper, as it is seen in Fig. 1, a base was first designed. It is important to position the midpoint of this part at the center of the coordinate system. Because this piece, which will later become the base of the gripper, will be connected from the center point while connected to the tip of the robot.

Then two pieces those are required to be opened sideways on the base were formed to be positioned on the base piece. After that, the parts to grip the work piece were designed and placed on the opening and closing parts. Subsequently, the "Union" command was used to connect the gripping part to the opening and closing part. The "Create Mechanism" selection under the "Modeling" tab should be made to convert this designed part into a moving mechanical object. When this selection is made, as it is seen in Fig. 2, a page titled "Create Mechanism" is opened. In this page, the settings of the mechanism were made. In this step, the links, joints and tool data are defined. After that, the home and end positions of the tool were defined. Home position is used when the gripper is closed and end

position is used when the gripper is open. Finally, the gripper tool definition was completed and the tool was attached to the robot. Considering the application, two tables and one work piece was designed and added in the station, as it can be seen in Fig. 3.

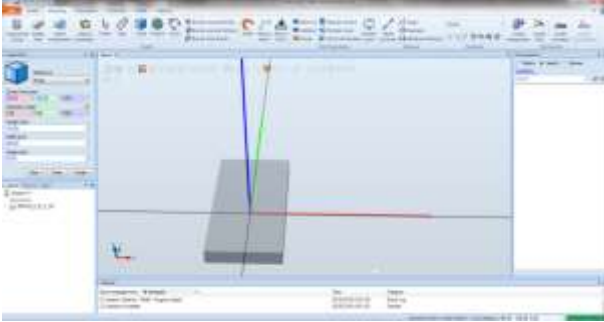


Figure 1. Creation of base for gripper

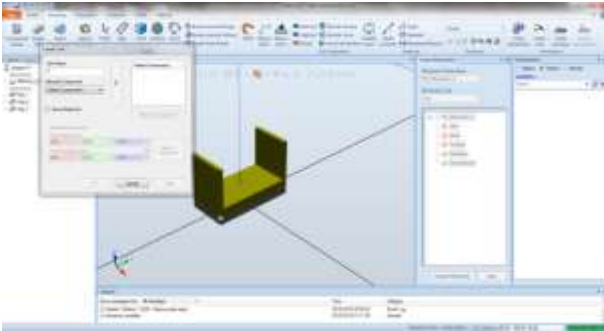


Figure 2. Definition of the mechanism



Figure 3. Designing the tables and the work piece

2.3 Adding the smart components

When parts are required to show complex behaviour other than routine movements, the "Smart Component" feature is used. In the gripper application, the work piece is waited to be sensed by a sensor on the gripper, then to be attached and to be travelling with the gripper. In order to manage the open and close actions of the gripper, "JointMover" was used. In order for the work piece to be sensed by the gripper, "LineSensor" was used. In order to attach the work piece to the gripper when the sensor senses it, "Attacher" was used. In order to detach

the work piece from the gripper when the sensor does not sense it, "Detacher" was used. In order to use in the block diagram, "NOT" and "LogisSRLatch" gates were used. After that, in the "Design" tab of the SmartComponent, input and output signals were defined. The input signal was named as "GrpAlBirak" and the output signal was named as "ParcaBagli". After making the necessary connections in the "Design" tab, the situation has been achieved as it can be seen in Fig. 4.



Figure 4. Completion of SmartComponent block diagram



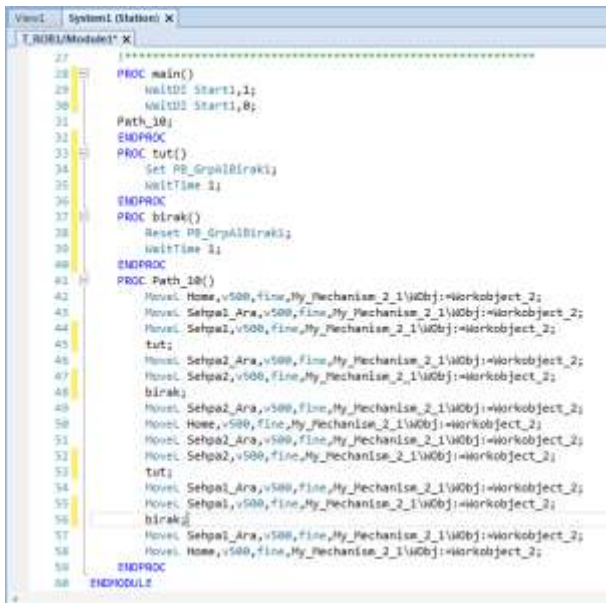
Figure 5. Completion of Station Logic block diagram

A new PROFIBUS card has been defined in the system so that the signals defined to be uses in the program could be collected on a separate card. At first, the PROFIBUS card with the name "Kart1" was defined. Then a warm restart was performed in order to complete the new card definition in the system. After that, an output signal with the name "PB_GrpAlBirak" and an input signal with the name "PB_SmartComponent" were defined in the "Kart1". Besides, an additional input signal with the name "Start" was defined in the "Kart1" as well. In order for the changes to be valid and active, a warm restart was performed again. Then, on the "StationLogic" screen that can be seen in Fig. 5, the necessary connections were made between the signals. In this configuration, the system's "PB_GrpAlBirak" output signal was connected to the SmartComponent's "GrpAlBirak" input signal. Then the SmartComponent's "ParcaBagli" output signal was connected to the system's

“PB_SmartComponent” input signal. The system’s “Start” input signal was then used in RAPID code page. After that, the target points were added and then the robot path was defined.

2.4 Program code writing in rapid and simulating

RAPID is the ABB robot programming language. In the next stage of the program, the necessary codes were written in the RAPID code editor. The main program was started under "main". In order to start the cycle, input signal "Start1" should be set to 1 and then to "0" with the push button algorithm. The commands "WaitDI Start1,1;" and then "WaitDI Start1,0;" were used for this. The commands "Set PB_GrpAlBirak1;" for the grip program and "Reset PB_GrpAlBirak1;" for the release program have been used. The "WaitTime 1;" command was used after the set and reset commands to wait 1 second when the gripper is opened and closed. Then grip and release programs were added in the required locations under “Path_10”. The screenshot of the program in this phase is seen in Fig. 6. When "Kart1" was selected in the "Device" tab of the "I/O Simulator" screen, it was observed that the I/O signals that have been defined on Kart1 were filtered out. After that, the "Play" key under the "Simulation" tab was pressed and the simulation was started. Then, it was observed that the program was running when the "Start1" signal was turned 1 and then 0.



```

27  |]
28  |PROC main()
29  |  WaitDI Start1,1;
30  |  WaitDI Start1,0;
31  |  Path_10;
32  |ENDPROC
33  |PROC tut()
34  |  Set PB_GrpAlBirak1;
35  |  WaitTime 1;
36  |ENDPROC
37  |PROC birak()
38  |  Reset PB_GrpAlBirak1;
39  |  WaitTime 1;
40  |ENDPROC
41  |PROC Path_10()
42  |  MoveL Home,v500,Line,My_Mechanism_2_1\WObj:=Workobject_2;
43  |  MoveL Selpa1_Ara,v500,Line,My_Mechanism_2_1\WObj:=Workobject_2;
44  |  MoveL Selpa2,v500,Line,My_Mechanism_2_1\WObj:=Workobject_2;
45  |  tut;
46  |  MoveL Selpa2_Ara,v500,Line,My_Mechanism_2_1\WObj:=Workobject_2;
47  |  MoveL Selpa2,v500,Line,My_Mechanism_2_1\WObj:=Workobject_2;
48  |  birak;
49  |  MoveL Selpa2_Ara,v500,Line,My_Mechanism_2_1\WObj:=Workobject_2;
50  |  MoveL Home,v500,Line,My_Mechanism_2_1\WObj:=Workobject_2;
51  |  MoveL Selpa1_Ara,v500,Line,My_Mechanism_2_1\WObj:=Workobject_2;
52  |  MoveL Selpa2,v500,Line,My_Mechanism_2_1\WObj:=Workobject_2;
53  |  tut;
54  |  MoveL Selpa1_Ara,v500,Line,My_Mechanism_2_1\WObj:=Workobject_2;
55  |  MoveL Selpa1,v500,Line,My_Mechanism_2_1\WObj:=Workobject_2;
56  |  birak;
57  |  MoveL Selpa1_Ara,v500,Line,My_Mechanism_2_1\WObj:=Workobject_2;
58  |  MoveL Home,v500,Line,My_Mechanism_2_1\WObj:=Workobject_2;
59  |ENDPROC
60  |ENDMODULE
  
```

Figure 6. The program code in RAPID code editor

3. Virtual Reality Application

ABB RobotStudio software is compatible with the HTC Vive virtual reality system. Thus, a simulation

prepared in this software can be experienced in 3D by connecting the HTC Vive virtual reality system. HTC Vive system provides virtual reality experience with the compatible software's. HTC Vive VR system consists of main stations, controllers and headset as shown in Fig. 7. The headset and the hand controllers are tracked devices. With the help of the main stations, they can locate themselves in the virtual world [1].

In order to be able to display with the virtual reality set, it is necessary to create a station viewer application from the station. At the same time, Station Viewer provides the ability to view the designed robot station and simulation even on computers without the Robot Studio software installed. In order to create the Station Viewer application of the designed robot station, the "Save Station as Viewer" must be selected in the "Share" section under the "File" tab. The screen image of the Station Viewer application which is saved on the desktop can be seen in Fig. 8.



Figure 7. HTC Vive main components [19]

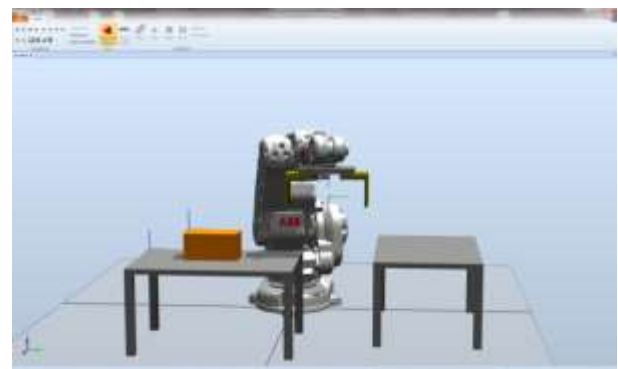


Figure 8. Station Viewer screenshot

"Virtual Reality" button can be seen under "Home" tab. When the HTC Vive virtual reality system was connected to the computer, the button had been activated. Then, when this button was clicked and HTC Vive headset was worn, the virtual environment was experienced as it can be seen in Fig. 9. However, when any point was marked with the sensors in the hands, the user was teleported to

that point in the virtual environment and observed the station from that point, as seen in Fig. 10.



Figure 9. Watching robot simulation with HTC Vive VR – 1

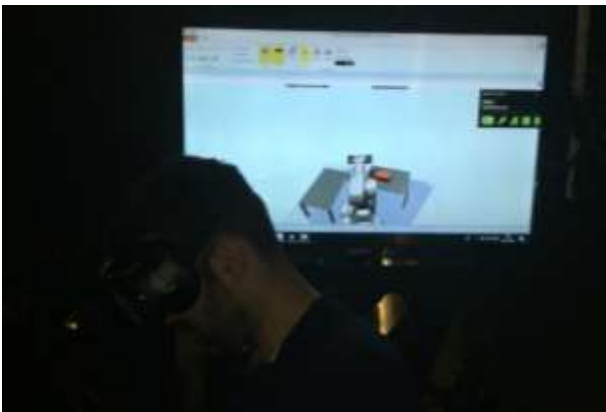


Figure 10. Watching robot simulation with HTC Vive VR – 2

4. Conclusion

Robotic production lines are very expensive investments. For this reason, all stage from project design phase to commissioning and also prototype and serial production stages are conducted under great cost and time pressure. It is expected that the line installation will be completed as quickly as possible and the outputs will be achieved at the desired quality level. In this study, it was preferred to use virtual reality to improve the offline robot programming process. First of all, a robot application which is used extensively in the automotive sector was programmed and simulated in ABB RobotStudio software. Then this simulation was experienced with the HTC Vive virtual reality system and it was confirmed that the program works as desired.

It was observed that the biggest advantage of using virtual reality technology was to be able to enter into the designed system almost as if it was in the real world and to examine the virtual system from any

desired direction. In this way, the designed system behaviour was observed much more clearly. This has been confirmed to have a positive impact on the duration and quality of offline robot programming. Virtual reality technology is foreseen to be used more intensively in the upcoming years to improve the offline robot programming processes, to respond effectively to the training needs of maintenance staff, and to improve robotic sales and marketing processes. In the future, it is emphasized the importance of focusing on integrating augmented reality technology into robot programming and even into robot maintenance processes as well.

References

- [1] A. Aras, M. Ayaz, E. Özdemir, N. Abut, "Investigation on Industry 4.0 and Virtual Commissioning", *International Journal of Engineering and Technologies - IJET*, vol. 4, no. 2, pp. 107-113, 2018.
- [2] M. F. Silva, "World Model Creation in ABB RobotStudio 5.15.02", ISEP - Instituto Superior de Engenharia do Porto, Project: ROBIN - Simulation and Offline Programming of Industrial Robots, 2016.
- [3] M. F. Silva, "Targets Creation in ABB RobotStudio 5.15.02", ISEP - Instituto Superior de Engenharia do Porto, Project: ROBIN - Simulation and Offline Programming of Industrial Robots, 2016.
- [4] M. F. Silva, "Program Creation in ABB RobotStudio 5.15.02", ISEP - Instituto Superior de Engenharia do Porto, Project: ROBIN - Simulation and Offline Programming of Industrial Robots, 2016.
- [5] M. F. Silva, "Simulation of the Robot Program in the Virtual Controller," ISEP - Instituto Superior de Engenharia do Porto, Project: ROBIN - Simulation and Offline Programming of Industrial Robots, 2016.
- [6] M. F. Silva, "Mechanism Creation in ABB RobotStudio 5.15.02", ISEP - Instituto Superior de Engenharia do Porto, Project: ROBIN - Simulation and Offline Programming of Industrial Robots, 2016.
- [7] V. Cohal, "A Welding Technology Using RobotStudio," in *21st Innovative Manufacturing Engineering & Energy International Conference – IManE&E 2017*, Iasi, Romania, 2017, pp. 1-6.
- [8] F. M. Moura, M. Silva, "Application for Automatic Programming of Palletizing Robots," in *18th IEEE International Conference on Autonomous Robot Systems and Competitions*, Torres Vedras, Portugal, 2018, pp. 1-5.
- [9] R. Holubek, P. Košťál, D. R. D. Sobrino, R. Roman, "Offline Programming of an ABB Robot Using Imported CAD Models in the RobotStudio Software Environment," *Applied Mechanics and Materials*, vol. 693, pp. 62-67, 2014.
- [10] C. Şekerci, "Sanal Gerçeklik Kavramının Tarihiçesi," *Uluslararası Sosyal Araştırmalar Dergisi*, c. 10, s. 54, ss. 1126-1133, 2017.

- [11] E. Bayraktar, F. Kaleli, “Sanal Gerçeklik ve Uygulama Alanları,” Akademik Bilişim Konferansı, Kütahya, Türkiye, 2007, ss. 1-6.
- [12] T. Tepe, D. Kaleci, H. Tuzun, “Eğitim Teknolojilerinde Yeni Eğilimler: Sanal Gerçeklik Uygulamaları,” 10th International Computer and Instructional Technologies Symposium, Rize, Türkiye, 2016, ss. 1-5.
- [13] Ç. Erbaş, V. Demirer, “Eğitimde Sanal ve Artırılmış Gerçeklik Uygulamaları,” Eğitim Teknolojileri Okumaları 2015, 1. baskı. Ankara, Türkiye: The Turkish Online Journal of Educational Technology, 2015, böl. 7, ss. 131-148.
- [14] S. Gökoğlu, M. Öztürk, F. Erdoğan, Ü. Çakıroğlu, “Öğrenme Ortamlarında Sanal Dönüşümler: Sanal Gerçeklik Yaklaşımı,” Eğitim Teknolojileri Okumaları 2017, 1. baskı. Ankara, Türkiye: The Turkish Online Journal of Educational Technology, 2017, böl. 23, ss. 423-434.
- [15] R. Ekici, A. Güven, “Sanal Gerçeklik Teknolojisinin Turizm Endüstrisindeki Rolü,” Avrasya Bilimler Akademisi Sosyal Bilimler Dergisi, c. 2017, s. UTKM, ss. 403-418, 2017.
- [16] E. Üzümcü, B. Akın, H. Nergiz, M. İnözü, U. Çelikcan, “Anksiyete Bozukluklarında Sanal Gerçeklik,” Psikiyatride Güncel Yaklaşımlar, c. 10, s. 1, ss. 99-117, 2018.
- [17] G. C. Quinn, A. Galeazzi, C. Gengnagel, “Augmented and Virtual Reality Structures,” in Proceedings of the IASS Annual Symposium 2017: Interfaces: architecture, engineering, science, Hamburg, Germany, 2017, pp. 1-8.
- [18] D. Yengin, “Virtual Reality as Technology,” in Communication and Technology Congress – CTC 2017, Istanbul, Turkey, 2017, pp. 57-68.
- [19] Anonim, (15 March 2018). [Online]. Erişim: <https://www.usgamer.net/articles/htc-vive-virtual-reality-systemdeluxe-audio-strap-549-black-friday-sale>



Power Research Technique of A Thermomechanical Condition of A Rod of Restricted Length, Variable Section at Influence of Heterogeneous Types of Sources of Heat

Anarbay Kudaykulov^{1*}, Azat Tashev¹, Mukaddas Arshidinova^{1,2}, Kalamkas Begaliyeva^{1,2}

¹ Institute of Information and Computing Technologies CS MES RK, Almaty, Kazakhstan

² Al-Farabi Kazakh National University, Almaty, Kazakhstan

* Corresponding Author : kudaykulov2006@mail.ru

ORCID: 0000-0002-5247-7850

Article Info:

DOI: 10.22399/ijcesen.539656

Received : 14 March 2019

Accepted : 22 November 2020

Keywords

Lengthening, axial force, section, temperature, deformation.

Abstract:

In this work on the basis of energy conservation laws with use square the spline of functions in the local system of coordinates is in number investigated thermo - the intense deformed condition of a horizontal rod of variable section and limited length. At the same time on the areas of transverse sections of two ends of a the rod heat fluxes of identical intensity are brought. Through lateral areas middle (1/3) parts of a the rod there is a heat exchange to a surrounding medium. Other parts of a lateral area are heat-insulated. Distribution laws of temperatures, all being deformations and tension, movements, and also sizes of thermal lengthening and the arising squeezing axial force are defined. Particular regularities are revealed.

1. Introduction

The bearing elements of the modern producer power stations, jet and hydrogen engines, nuclear and thermal power plants, and also technological lines of processing industry are rod stock of variable section. Most of them work at simultaneous influence of diverse types of sources of heat. In this regard reliable work of the above-stated installations and inventories will be depends on thermodurability of the used rod elements of variable section and limited length. Therefore a research thermo - an intense strained state of the rod of variable section and limited length taking into account simultaneous existence of diverse types of sources of heat, local thermal insulations and physicommechanical properties of materials of the rod stock are a relevant task. At the same time the received decisions have to be reliable at the level of fundamental laws of conservation of energy [1,2].

2. Formulation of the problem an methods

The horizontal rod of variable section and limited length of L [cm] is considered. The horizontal axis ox coincides with a rod axle. The transverse section of the considered rod is a circle.

The rod section radius on coordinate changes linearly under the where and a and b constant. At this b—the radius of a transverse section of the left-hand end.

The cross-sectional area of the rod varies according to the formula

$$F(x) = \pi r^2 = \pi(a^2 x^2 + 2abx + b^2), (0 \leq x \leq L)$$

Physicommechanical and thermal properties of material of a the rod it is characterized by a material elastic modulus, $E[\frac{kG}{cm^2}]$ thermal

expansion coefficients, $\alpha[\frac{1}{K}]$ and heat

conductivity $K_{xx}[\frac{Watt}{cm^0 K}]$. On the area of transverse

sections of two ends of the studied rod it is brought heat fluxes with identical intensity $q[\frac{Watt}{cm^2}]$.

Lateral areas the first ($0 \leq x \leq l$), $l = \frac{L}{3}$ [cm], and third ($2l \leq x \leq 3l = L$) (1/3) parts of a the rod are heat-insulated.

Through a lateral area of average (1/3) parts ($l \leq x \leq 2l$) happen heat exchange to a surrounding medium. At the same time heat exchange coefficient, and environment temperature of $h[\frac{Watt}{cm^2 \cdot K}]$. Here it should be noted that. The

settlement scheme of a task is provided in the Figure 1. It is required: to construct approximating square a function spline in a local frame; to formulate a task at the level of the law of conservation of energy in the form of a functional of the total thermal energy for definition the field of temperatures; to define the integrated type of a functional of the total thermal energy; to construct the allowing system of the simple algebraic equations taking into account natural boundary conditions for definition the field of temperatures; In case one end of the studied rod rigid is jammed, and another is free it is necessary to determine the size of its lengthening taking into account simultaneous existence of local thermal insulations, heat exchange, heat fluxes, thermal properties of material of a the rod and its geometry; it is necessary to calculate values of the arising squeezing axial force taking into account geometry and physicomechanical and thermal properties of material of a rod and also existence of diverse types of sources of heat and local thermal insulations in case of jamming of two ends of the considered rod; to define the field of temperature, thermoelastic, temperature and elastic components of deformations and tension; to write a functional potential to energy of elastic deformation taking into account existence the field of temperature for definition the field of movement on the basis of the law of conservation of energy; to define the integrated type of a functional of a potential energy resilient deformations taking into account existence the field of temperature; o construct the allowing system of the simple algebraic equations taking into account natural boundary conditions; to build the field of movement taking into account is jammed of two ends of the studied rod of variable section and limited length.

3. Construction Spline of Functions and of a Functional of Energy

Let's consider one discrete site of a the rod length of l [cm]. The field of temperature longwise of a the

rod, we approximate the complete polynom of the second order.

$$T(x) = c_1 x^2 + c_2 x + c_3 = \phi_i(x) \cdot T_i + \phi_j(x) \cdot T_j + \phi_k(x) \cdot T_k, \quad 0 \leq x \leq l \tag{1}$$

$$\begin{aligned} \text{где } T_i &= T(x=0); & \phi_j(x) &= \frac{4lx - 4x^2}{l^2}; \\ \phi_k(x) &= \frac{2x^2 - lx}{l^2}; \end{aligned} \tag{2}$$

These functions we will call square a spline functions in a local frame ($0 \leq x \leq l$). With in rod length ($0 \leq x \leq l$) the gradient of temperature is defined from (1-2)

$$\frac{\partial T}{\partial x} = \frac{\partial \phi_i}{\partial x} T_i + \frac{\partial \phi_j}{\partial x} T_j + \frac{\partial \phi_k}{\partial x} T_k = \frac{4x - 3l}{l^2} T_i + \frac{4l - 8x}{l^2} T_j + \frac{4x - l}{l^2} T_k, \quad 0 \leq x \leq l \tag{3}$$

Using the law of conservation of energy, for the considered task we will write a functional of the total thermal energy [3]

$$\begin{aligned} J = \int_{F(x=0)} qT ds + \int_{V_1} \frac{K_{xx}}{2} \left(\frac{\partial T}{\partial x} \right)^2 dv + \int_{S(0 \leq x \leq 2l)} \frac{h}{2} (T - T_{oc})^2 ds + \int_{V_2} \frac{K_{xx}}{2} \left(\frac{\partial T}{\partial x} \right)^2 dv + \\ + \int_{V_3} \frac{K_{xx}}{2} \left(\frac{\partial T}{\partial x} \right)^2 dv + \int_{F(x=L)} qT ds \end{aligned} \tag{4}$$

where $F(x=0)$ and $F(x=L)$ - cross-sectional area of the two ends of the investigated rod; Wherein $F(x=0) \gg F(x=L)$ - V_1, V_2 and V_3 - volumes of three sections of the rod; For the 1st section ($0 \leq x \leq l$) considered rod

$$\begin{aligned} T_i &= T(x=0) = T_1; & T_j &= T(x = \frac{l}{2}) = T_2; \\ T_k &= T(x=l) = T_3; & \text{For the 2nd section} \\ (l \leq x \leq 2l) & \text{ respectively } T_i &= T(x=l) = T_3; \\ T_j &= T(x = \frac{3l}{2}) = T_4; & T_k &= T(x=2l) = T_5; \end{aligned}$$

Finally, for the third section ($2l \leq x \leq 3l = L$) will get

$$\begin{aligned} T_i &= T(x=2l) = T_5; & T_j &= T(x = \frac{5l}{2}) = T_6; \\ T_k &= T(x=3l=L) = T_7. \end{aligned}$$

At this designated after an integration (4) has an appearance:

$$\begin{aligned}
 J = & \pi \cdot b_1^2 \cdot q \cdot T_1 + \frac{\pi \cdot K_{xx}}{2} \left[\left(\frac{a^2 l}{5} + ab_1 + \frac{7b_1^2}{3l} \right) \cdot T_1^2 + \left(\frac{32a^2 l}{15} + \frac{16ab_1}{3} + \frac{16b_1^2}{3l} \right) \cdot T_2^2 + \right. \\
 & + \left(\frac{26a^2 l}{15} + \frac{a(11b_1 + 3b_2)}{3} + \frac{7(b_1^2 + b_2^2)}{3l} \right) \cdot T_3^2 - \left(\frac{4a^2 l}{5} + \frac{8ab_1}{3} + \frac{16b_1^2}{3l} \right) \cdot T_1 \cdot T_2 + \left(\frac{2a^2 l}{5} + \frac{2ab_1}{3} + \frac{2b_1^2}{3l} \right) \cdot T_1 \cdot T_3 - \\
 & - \left(\frac{52a^2 l}{15} + 8ab_1 + \frac{16b_1^2}{3l} \right) \cdot T_2 \cdot T_3 + \left(\frac{32a^2 l}{15} + \frac{16ab_2}{3} + \frac{16b_2^2}{3l} \right) \cdot T_4^2 + \left(\frac{26a^2 l}{15} + \frac{a(11b_2 + 3b_3)}{3} + \frac{7(b_2^2 + b_3^2)}{3l} \right) \cdot T_5^2 - \\
 & - \left(\frac{4a^2 l}{5} + \frac{8ab_2}{3} + \frac{16b_2^2}{3l} \right) \cdot T_3 \cdot T_4 + \left(\frac{2a^2 l}{5} + \frac{2ab_2}{3} + \frac{2b_2^2}{3l} \right) \cdot T_3 \cdot T_5 - \left(\frac{52a^2 l}{15} + 8ab_2 + \frac{16b_2^2}{3l} \right) \cdot T_4 \cdot T_5 + \\
 & + \left(\frac{32a^2 l}{15} + \frac{16ab_3}{3} + \frac{16b_3^2}{3l} \right) \cdot T_6^2 + \left(\frac{23a^2 l}{15} + \frac{11ab_3}{3} + \frac{7b_3^2}{3l} \right) \cdot T_7^2 - \left(\frac{4a^2 l}{5} + \frac{8ab_3}{3} + \frac{16b_3^2}{3l} \right) \cdot T_5 \cdot T_6 + \quad (5) \\
 & + \left(\frac{2a^2 l}{5} + \frac{2ab_3}{3} + \frac{2b_3^2}{3l} \right) \cdot T_5 \cdot T_7 - \left(\frac{52a^2 l}{15} + 8ab_3 + \frac{16b_3^2}{3l} \right) \cdot T_6 \cdot T_7 \Big] + h \cdot \pi \cdot \left[\left(\frac{al^2}{60} + \frac{2b_2 l}{15} \right) \cdot T_3^2 + \right. \\
 & + \left(\frac{4al^2}{15} + \frac{8b_2 l}{15} \right) \cdot T_4^2 + \left(\frac{7al^2}{60} + \frac{2b_2 l}{15} \right) \cdot T_5^2 + \frac{2b_2 l}{15} \cdot T_3 \cdot T_4 - \left(\frac{al^2}{30} + \frac{b_2 l}{15} \right) \cdot T_3 \cdot T_5 + \left(\frac{2al^2}{15} + \frac{2b_2 l}{15} \right) \cdot T_4 \cdot T_5 + \\
 & + \left(\frac{al^2}{2} + b_2 l \right) \cdot T_0^2 - \frac{b_2 l}{3} \cdot T_3 \cdot T_0 - \left(\frac{2al^2}{3} + \frac{4b_2 l}{3} \right) \cdot T_4 \cdot T_0 - \left(\frac{al^2}{3} + \frac{b_2 l}{3} \right) \cdot T_5 \cdot T_0 + \pi(3al + b)^2 \cdot q \cdot T_7;
 \end{aligned}$$

Minimizing the last functional on nodal value of temperatures T1,T2,...,T7, we will receive the allowing system of the simple algebraic equations, natural boundary conditions are considered.

$$\begin{aligned}
 1) \frac{\partial J}{\partial T_1} = 0; & \Rightarrow \pi \cdot b_1^2 \cdot q + \frac{\pi K_{xx}}{2} \left[2 \cdot \left(\frac{a^2 l}{5} + ab_1 + \frac{7b_1^2}{3l} \right) \cdot T_1 - \left(\frac{4a^2 l}{5} + \frac{8ab_1}{3} + \frac{16b_1^2}{3l} \right) \cdot T_2 + \right. \\
 & \left. + \left(\frac{2a^2 l}{5} + \frac{2ab_1}{3} + \frac{2b_1^2}{3l} \right) \cdot T_3 \right] = 0; \\
 2) \frac{\partial J}{\partial T_2} = 0; & \Rightarrow \frac{\pi K_{xx}}{2} \left[2 \cdot \left(\frac{32a^2 l}{15} + \frac{16ab_1}{3} + \frac{16b_1^2}{3l} \right) \cdot T_2 - \left(\frac{4a^2 l}{5} + \frac{8ab_1}{3} + \frac{16b_1^2}{3l} \right) \cdot T_1 - \right. \\
 & \left. - \left(\frac{52a^2 l}{15} + 8ab_1 + \frac{16b_1^2}{3l} \right) \cdot T_3 \right] = 0; \quad (6)
 \end{aligned}$$

$$\begin{aligned}
3) \frac{\partial J}{\partial T_3} = 0; \Rightarrow & \frac{\pi K_{xx}}{2} \left[\left(\frac{2a^2l}{5} + \frac{2ab_1}{3} + \frac{2b_1^2}{3l} \right) \cdot T_1 - \left(\frac{52a^2l}{15} + 8ab_1 + \frac{16b_1^2}{3l} \right) \cdot T_2 + \right. \\
& + 2 \cdot \left(\frac{26a^2l}{15} + \frac{a(11b_1 + 3b_2)}{3} + \frac{7(b_1^2 + b_2^2)}{3l} \right) \cdot T_3 - \left(\frac{4a^2l}{5} + \frac{8ab_2}{3} + \frac{16b_2^2}{3l} \right) \cdot T_4 + \\
& \left. + \left(\frac{2a^2l}{5} + \frac{2ab_2}{3} + \frac{2b_2^2}{3l} \right) \cdot T_5 \right] + h\pi \left[2 \cdot \left(\frac{al^2}{60} + \frac{2b_2l}{15} \right) \cdot T_3 + \frac{2b_2l}{15} \cdot T_4 - \left(\frac{al^2}{30} + \frac{b_2l}{15} \right) \cdot T_5 - \right. \\
& \left. - \frac{b_2l}{3} \cdot T_0 \right] = 0;
\end{aligned}$$

$$\begin{aligned}
4) \frac{\partial J}{\partial T_4} = 0; \Rightarrow & h\pi \left[2 \cdot \left(\frac{4al^2}{15} + \frac{8b_2l}{15} \right) \cdot T_4 + \frac{2b_2l}{15} \cdot T_3 + \left(\frac{2al^2}{15} + \frac{2b_2l}{15} \right) \cdot T_5 - \right. \\
& \left. - \left(\frac{2al^2}{3} + \frac{4b_2l}{3} \right) \cdot T_0 \right] + \frac{\pi K_{xx}}{2} \left[2 \cdot \left(\frac{32a^2l}{15} + \frac{16ab_2}{3} + \frac{16b_2^2}{3l} \right) \cdot T_4 - \left(\frac{4a^2l}{5} + \frac{8ab_2}{3} + \frac{16b_2^2}{3l} \right) \cdot \right. \\
& \left. \cdot T_3 - \left(\frac{52a^2l}{15} + 8ab_2 + \frac{16b_2^2}{3l} \right) \cdot T_5 \right] = 0;
\end{aligned}$$

$$\begin{aligned}
5) \frac{\partial J}{\partial T_5} = 0; \Rightarrow & h\pi \left[2 \cdot \left(\frac{7al^2}{60} + \frac{2b_2l}{15} \right) \cdot T_5 - \left(\frac{al^2}{30} + \frac{b_2l}{15} \right) \cdot T_3 + \left(\frac{2al^2}{15} + \frac{2b_2l}{15} \right) \cdot T_4 - \right. \\
& \left. - \left(\frac{al^2}{3} + \frac{b_2l}{3} \right) \cdot T_0 \right] + \frac{\pi K_{xx}}{2} \left[\left(\frac{2a^2l}{5} + \frac{2ab_2}{3} + \frac{2b_2^2}{3l} \right) \cdot T_3 - \left(\frac{52a^2l}{15} + 8ab_2 + \frac{16b_2^2}{3l} \right) \cdot T_4 + \right. \\
& + 2 \cdot \left(\frac{26a^2l}{15} + \frac{a(11b_2 + 3b_3)}{3} + \frac{7(b_2^2 + b_3^2)}{3l} \right) \cdot T_5 - \left(\frac{4a^2l}{5} + \frac{8ab_3}{3} + \frac{16b_3^2}{3l} \right) \cdot T_6 + \\
& \left. + \left(\frac{2a^2l}{5} + \frac{2ab_3}{3} + \frac{2b_3^2}{3l} \right) \cdot T_7 \right] = 0;
\end{aligned}$$

$$\begin{aligned}
6) \frac{\partial J}{\partial T_6} = 0; \Rightarrow & \frac{\pi K_{xx}}{2} \left[2 \cdot \left(\frac{32a^2l}{15} + \frac{16ab_3}{3} + \frac{16b_3^2}{3l} \right) \cdot T_6 - \left(\frac{4a^2l}{5} + \frac{8ab_3}{3} + \frac{16b_3^2}{3l} \right) \cdot T_5 + \right. \\
& \left. - \left(\frac{52a^2l}{15} + 8ab_3 + \frac{16b_3^2}{3l} \right) \cdot T_7 \right] = 0;
\end{aligned}$$

$$\begin{aligned}
7) \frac{\partial J}{\partial T_7} = 0; \Rightarrow & \frac{\pi K_{xx}}{2} \left[2 \cdot \left(\frac{23a^2l}{15} + \frac{11ab_3}{3} + \frac{7b_3^2}{3l} \right) \cdot T_7 + \left(\frac{2a^2l}{5} + \frac{2ab_3}{3} + \frac{2b_3^2}{3l} \right) \cdot T_5 - \right. \\
& \left. - \left(\frac{52a^2l}{15} + 8ab_3 + \frac{16b_3^2}{3l} \right) \cdot T_6 \right] + \pi(3al + b)^2 \cdot q = 0.
\end{aligned}$$

Solving this system we define nodal values of temperatures T_1, T_2, \dots, T_7 . On them the distribution law of temperature longwise of each site of the studied rod is under construction. For the first site ($0 \leq x \leq l$) of a the rod it has the following appearance:

$$T^{(I)}(x) = \phi_i(x) \cdot T_1 + \phi_j(x) \cdot T_2 + \phi_k(x) \cdot T_3 \quad (7)$$

Similar to the field of temperatures longwise of the 2nd and 3rd sites of a the rod has an appearance:

$$T^{(II)}(x) = \phi_i(x) \cdot T_3 + \phi_j(x) \cdot T_4 + \phi_k(x) \cdot T_5 \quad (8)$$

$$T^{(III)}(x) = \phi_i(x) \cdot T_5 + \phi_j(x) \cdot T_6 + \phi_k(x) \cdot T_7 \quad (9)$$

If one end of a the rod it is rigidly jammed, and another is free, then because of existence of diverse types of sources of heat it is extended. The size of lengthening is defined on the basis of fundamental laws of an applied thermal physics.

$$\Delta L_T = \int_0^L \alpha \cdot T(x) dx. \quad (10)$$

In case of jamming of two ends of a the rod, the rod can't be extended, and owing to existence of diverse types of sources of heat there is axial R [kG] squeezing efforts. The size of this effort is defined from a consistency relation of deformation [4].

$$R = - \frac{E \cdot F_{av} \cdot \Delta L_T}{L} = - \frac{E \cdot F_{av}}{L} \int_0^L T(x) dx \quad (11)$$

where $F_{av} = \frac{1}{L} \int_0^L F(x) dx$ – average area of a transverse section.

In case of jamming of two ends of a the rod there is also a field of distribution of the being deformations and tension. The distribution law of a thermoelastic component of tension is defined according to a Hooke law [4].

$$\sigma(x) = \frac{R}{F(x)}, \quad 0 \leq x \leq l. \quad (12)$$

In compliance of a Hooke law it is also possible to construct the distribution law of a thermoelastic component of deformations $\varepsilon(x)$ [dimensionless]:

$$\varepsilon(x) = \frac{\sigma(x)}{E}, \quad 0 \leq x \leq l \quad (13)$$

In compliance the law of a thermal physics the field of distribution of a temperature component of deformations is under construction:

$$\varepsilon_T(x) = -\alpha T(x), \quad 0 \leq x \leq l \quad (14)$$

Then according to the generalized Hooke law the distribution law of a temperature component of tension is defined

$$\sigma_T(x) = E \cdot \varepsilon_T(x), \quad 0 \leq x \leq l \quad (15)$$

At last in compliance of the theory of a thermoelasticity it is possible to construct distribution laws of elastic components of deformations and tension

$$\begin{aligned} \varepsilon_x(x) &= \varepsilon(x) - \varepsilon_T(x), \\ \sigma_x(x) &= E \cdot \varepsilon_x(x) = \sigma(x) - \sigma_T(x), \quad 0 \leq x \leq l \end{aligned} \quad (16)$$

For definition the field of movement we will write a functional potential to energy of elastic deformation in the presence the field of temperatures for one discrete element:

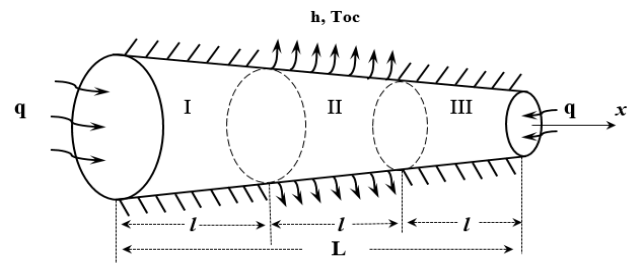


Figure 1. The settlement scheme of the considered task

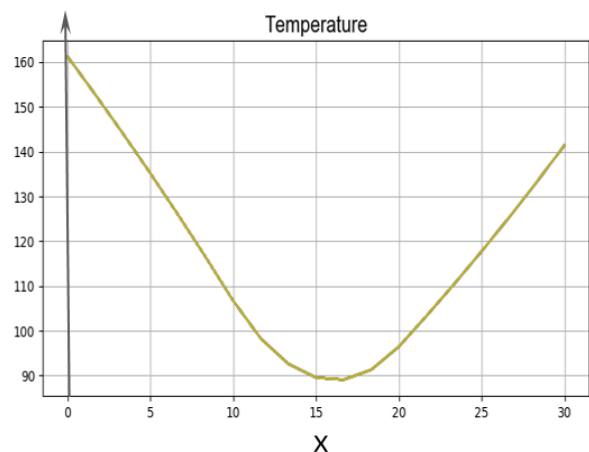


Figure 2. Dependences of temperature T the length of the rod

$$\begin{aligned} \Pi &= \int_V \frac{\sigma_x(x)}{2} \varepsilon_x(x) dv - \int_V \alpha E \cdot T(x) \cdot \varepsilon_x(x) dv = \frac{E}{2} \int_V \varepsilon_x^2 dv - \alpha E \int_V T(x) \cdot \varepsilon_x(x) dv = \\ &= \frac{E\pi}{2} \int_0^l F(x) \left(\frac{\partial U}{\partial x} \right)^2 dx - \alpha E \pi \int_0^l F(x) \cdot T(x) \frac{\partial U}{\partial x} dx = \frac{E\pi}{2} \int_0^l (a^2 x^2 + 2abx + b^2) \cdot \\ &\cdot \left[\frac{4x-3l}{l^2} U_i + \frac{4l-8x}{l^2} U_j + \frac{4x-l}{l^2} U_k \right]^2 dx - \alpha E \pi \int_0^l (a^2 x^2 + 2abx + b^2) \cdot \\ &\cdot \left[\frac{2x^2-3lx+l^2}{l^2} \cdot U_i \frac{4lx-4x^2}{l^2} \cdot U_j + \frac{2x^2-lx}{l^2} \cdot U_k \right] \cdot \left[\frac{4x-3l}{l^2} U_i + \frac{4l-8x}{l^2} U_j + \frac{4x-l}{l^2} U_k \right]^2 dx \quad (17) \end{aligned}$$

where $U(x) = \phi_i(x) \cdot U_i + \phi_j(x) \cdot U_j + \phi_k(x) \cdot U_k$, $0 \leq x \leq l$.

After an integration it has an appearance:

$$\begin{aligned} \Pi &= \frac{E\pi}{2} \left\{ \left[\left(\frac{a^2 l}{5} + ab_1 + \frac{7b_1^2}{3l} \right) \cdot U_1^2 - \left(\frac{4a^2 l}{5} + \frac{8ab_1}{3} + \frac{16b_1^2}{3l} \right) \cdot U_1 U_2 + \left(\frac{2a^2 l}{5} + \frac{2ab_1}{3} + \frac{2b_1^2}{3l} \right) \cdot U_1 U_3 + \right. \right. \\ &+ \left. \left(\frac{32a^2 l}{15} + \frac{16ab_1}{3} + \frac{16b_1^2}{3l} \right) \cdot U_2^2 - \left(\frac{52a^2 l}{15} + 8ab_1 + \frac{16b_1^2}{3l} \right) \cdot U_2 U_3 + \left(\frac{26a^2 l}{15} + \frac{a(11b_1 + 3b_2)}{3} + \right. \right. \\ &+ \left. \left. \frac{7(b_1^2 + b_2^2)}{3l} \right) \cdot U_3^2 \right] + \left[- \left(\frac{4a^2 l}{5} + \frac{8ab_2}{3} + \frac{16b_2^2}{3l} \right) \cdot U_3 U_4 + \left(\frac{2a^2 l}{5} + \frac{2ab_2}{3} + \frac{2b_2^2}{3l} \right) \cdot U_3 U_5 + \right. \\ &+ \left. \left(\frac{32a^2 l}{15} + \frac{16ab_2}{3} + \frac{16b_2^2}{3l} \right) \cdot U_4^2 - \left(\frac{52a^2 l}{15} + 8ab_2 + \frac{16b_2^2}{3l} \right) \cdot U_4 U_5 + \left(\frac{26a^2 l}{15} + \frac{a(11b_2 + 3b_3)}{3} + \right. \right. \\ &+ \left. \left. \frac{7(b_2^2 + b_3^2)}{3l} \right) \cdot U_5^2 \right] + \left[- \left(\frac{4a^2 l}{5} + \frac{8ab_3}{3} + \frac{16b_3^2}{3l} \right) \cdot U_5 U_6 + \left(\frac{2a^2 l}{5} + \frac{2ab_3}{3} + \frac{2b_3^2}{3l} \right) \cdot U_5 U_7 + \right. \\ &+ \left. \left(\frac{32a^2 l}{15} + \frac{16ab_3}{3} + \frac{16b_3^2}{3l} \right) \cdot U_6^2 - \left(\frac{52a^2 l}{15} + 8ab_3 + \frac{16b_3^2}{3l} \right) \cdot U_6 U_7 + \left(\frac{23a^2 l}{15} + \frac{11ab_3}{3} + \frac{7b_3^2}{3l} \right) \cdot U_7^2 \right] \\ &- \alpha E \pi \left[- \left(\frac{a^2 l^2}{60} + \frac{2ab_1 l}{15} + \frac{b_1^2}{2} \right) \cdot T_1 U_1 + \left(\frac{a^2 l^2}{15} + \frac{4ab_1 l}{15} + \frac{2b_1^2}{3} \right) \cdot T_1 U_2 - \left(\frac{a^2 l^2}{20} + \frac{2ab_1 l}{15} + \frac{b_1^2}{6} \right) \cdot T_1 U_3 - \right. \\ &- \left(\frac{a^2 l^2}{15} + \frac{2ab_1 l}{5} + \frac{2b_1^2}{3} \right) \cdot T_2 U_1 - \left(\frac{4a^2 l^2}{15} + \frac{8ab_1 l}{15} \right) \cdot T_2 U_2 + \left(\frac{a^2 l^2}{3} + \frac{14ab_1 l}{15} + \frac{2b_1^2}{3} \right) \cdot T_2 U_3 + \\ &+ \left. \left(\frac{a^2 l^2}{12} + \frac{ab_1 l}{5} + \frac{b_1^2}{2} \right) \cdot T_3 U_1 - \left(\frac{7a^2 l^2}{15} + \frac{16ab_1 l}{15} + \frac{2b_1^2}{3} \right) \cdot T_3 U_2 + \left(\frac{22a^2 l^2}{60} + \frac{11al(b_1 - b_2)}{15} + \right. \right. \end{aligned} \quad (18)$$

$$\begin{aligned}
 & + \frac{b_1^2 - 2b_2^2}{2} T_3 U_3 \Big] + \left[\left(\frac{a^2 l^2}{15} + \frac{4ab_2 l}{15} + \frac{2b_2^2}{3} \right) \cdot T_3 U_4 - \left(\frac{a^2 l^2}{20} + \frac{2ab_2 l}{15} + \frac{b_2^2}{6} \right) \cdot T_3 U_5 - \left(\frac{a^2 l^2}{15} + \frac{2ab_2 l}{5} + \right. \right. \\
 & \left. \left. + \frac{2b_2^2}{3} \right) \cdot T_4 U_3 - \left(\frac{4a^2 l^2}{15} + \frac{8ab_2 l}{15} \right) \cdot T_4 U_4 + \left(\frac{a^2 l^2}{3} + \frac{4ab_2 l}{15} + \frac{2b_2^2}{3} \right) \cdot T_4 U_5 + \left(\frac{a^2 l^2}{12} + \frac{ab_2 l}{5} + \frac{b_2^2}{6} \right) \cdot T_5 U_3 - \right. \\
 & \left. - \left(\frac{7a^2 l^2}{15} + \frac{16ab_2 l}{15} + \frac{2b_2^2}{3} \right) \cdot T_5 U_4 + \left(\frac{22a^2 l^2}{60} + \frac{al(13b_2 - 2b_3)}{15} + \frac{b_2^2 - b_3^2}{2} \right) \cdot T_5 U_5 \right] + \left[\left(\frac{a^2 l^2}{15} + \frac{4ab_3 l}{15} + \right. \right. \\
 & \left. \left. + \frac{2b_3^2}{2} \right) \cdot T_3 U_6 - \left(\frac{a^2 l^2}{20} + \frac{2ab_3 l}{15} + \frac{b_3^2}{6} \right) \cdot T_3 U_7 - \left(\frac{a^2 l^2}{15} + \frac{2ab_3 l}{5} + \frac{2b_3^2}{3} \right) \cdot T_6 U_5 - \left(\frac{4a^2 l^2}{15} + \frac{8ab_3 l}{15} \right) \cdot T_6 U_6 + \right. \\
 & \left. + \left(\frac{a^2 l^2}{3} + \frac{14ab_3 l}{15} + \frac{2b_3^2}{3} \right) \cdot T_6 U_7 + \left(\frac{a^2 l^2}{12} + \frac{ab_3 l}{5} + \frac{b_3^2}{6} \right) \cdot T_7 U_5 - \left(\frac{7a^2 l^2}{15} + \frac{16ab_3 l}{15} + \frac{2b_3^2}{3} \right) \cdot T_7 U_6 + \right. \\
 & \left. + \left(\frac{23a^2 l^2}{60} + \frac{13ab_3 l}{15} + \frac{b_3^2}{2} \right) \cdot T_7 U_7 \right] \Big\}.
 \end{aligned}$$

For determination of value of movement of sections we minimize a functional of a potential energy on nodal points:

$$\begin{aligned}
 1) \frac{\partial \Pi}{\partial U_1} = 0; & \Rightarrow \frac{E\pi}{2} \left[2 \cdot \left(\frac{a^2 l}{5} + ab_1 + \frac{7b_1^2}{3l} \right) \cdot U_1 - \left(\frac{4a^2 l}{5} + \frac{8ab_1}{3} + \frac{16b_1^2}{3l} \right) \cdot U_2 + \left(\frac{2a^2 l}{5} + \frac{2ab_1}{3} + \frac{2b_1^2}{3l} \right) \cdot \right. \\
 & \left. U_3 \right] - \alpha E\pi \left[- \left(\frac{a^2 l^2}{60} + \frac{2ab_1 l}{15} + \frac{b_1^2}{2} \right) \cdot T_1 - \left(\frac{a^2 l^2}{15} + \frac{2ab_1 l}{5} + \frac{2b_1^2}{3} \right) \cdot T_2 + \left(\frac{a^2 l^2}{12} + \frac{ab_1 l}{5} + \frac{b_1^2}{6} \right) \cdot T_3 \right] = 0; \\
 2) \frac{\partial \Pi}{\partial U_2} = 0; & \Rightarrow \frac{E\pi}{2} \left[- \left(\frac{4a^2 l}{5} + \frac{8ab_1}{3} + \frac{16b_1^2}{3l} \right) \cdot U_1 + 2 \left(\frac{32a^2 l}{15} + \frac{16ab_1}{3} + \frac{16b_1^2}{3l} \right) \cdot U_2 - \left(\frac{52a^2 l}{5} + 8ab_1 + \right. \right. \\
 & \left. \left. + \frac{16b_1^2}{3l} \right) \cdot U_3 \right] - \alpha E\pi \left[\left(\frac{a^2 l^2}{15} + \frac{4ab_1 l}{15} + \frac{2b_1^2}{3} \right) \cdot T_1 - \left(\frac{4a^2 l^2}{15} + \frac{8ab_1 l}{15} \right) \cdot T_2 - \left(\frac{7a^2 l^2}{15} + \frac{16ab_1 l}{15} + \frac{2b_1^2}{3} \right) \cdot T_3 \right] = 0; \\
 3) \frac{\partial \Pi}{\partial U_3} = 0; & \Rightarrow \frac{E\pi}{2} \left[\left(\frac{2a^2 l}{5} + \frac{2ab_1}{3} + \frac{2b_1^2}{3l} \right) \cdot U_1 - \left(\frac{52a^2 l}{15} + 8ab_1 + \frac{16b_1^2}{3l} \right) \cdot U_2 + 2 \left(\frac{26a^2 l}{15} + \frac{a(11b_1 + 3b_2)}{3} + \right. \right. \\
 & \left. \left. + \frac{7(b_1^2 + b_2^2)}{3l} \right) \cdot U_3 \right] - \alpha E\pi \left[- \left(\frac{a^2 l^2}{20} + \frac{2ab_1 l}{15} + \frac{b_1^2}{6} \right) \cdot T_1 + \left(\frac{a^2 l^2}{3} + \frac{14ab_1 l}{15} + \frac{2b_1^2}{3} \right) \cdot T_2 + \left(\frac{22a^2 l^2}{60} + \right. \right. \\
 & \left. \left. + \frac{al(13b_1 - 2b_2)}{15} + \frac{b_1^2 - b_2^2}{2} \right) \cdot T_3 - \left(\frac{a^2 l^2}{15} + \frac{2ab_2 l}{5} + \frac{2b_2^2}{3} \right) \cdot T_4 + \left(\frac{a^2 l^2}{12} + \frac{ab_2 l}{5} + \frac{b_2^2}{6} \right) \cdot T_5 \right] = 0;
 \end{aligned}$$

$$\begin{aligned}
 4) \frac{\partial \Pi}{\partial U_4} = 0; &\Rightarrow \frac{E\pi}{2} \left[- \left(\frac{4a^2l}{5} + \frac{8ab_2}{3} + \frac{16b_2^2}{3l} \right) \cdot U_3 + 2 \left(\frac{32a^2l}{15} + \frac{16ab_2}{3} + \frac{16b_2^2}{3l} \right) \cdot U_4 - 2 \left(\frac{52a^2l}{15} + 8ab_2 + \right. \right. \\
 &\left. \left. + \frac{16b_2^2}{3l} \right) \cdot U_5 \right] - \alpha E \pi \left[\left(\frac{a^2l^2}{15} + \frac{4ab_2l}{15} + \frac{2b_2^2}{3} \right) \cdot T_3 - \left(\frac{4a^2l^2}{15} + \frac{8ab_2l}{15} \right) \cdot T_4 - \left(\frac{7a^2l^2}{15} + \frac{16ab_2l}{15} + \frac{2b_2^2}{3} \right) \cdot T_5 \right] = 0; \\
 5) \frac{\partial \Pi}{\partial U_3} = 0; &\Rightarrow \frac{E\pi}{2} \left[\left(\frac{2a^2l}{5} + \frac{2ab_2}{3} + \frac{2b_2^2}{3l} \right) \cdot U_3 - \left(\frac{52a^2l}{15} + 8ab_2 + \frac{16b_2^2}{3l} \right) \cdot U_4 + 2 \left(\frac{26a^2l}{15} + \frac{a(11b_2 + 3b_3)}{3} + \right. \right. \\
 &\left. \left. + \frac{7(b_2^2 + b_3^2)}{3l} \right) \cdot U_5 - \left(\frac{4a^2l}{5} + \frac{8ab_3}{3} + \frac{16b_3^2}{3l} \right) \cdot U_6 + \left(\frac{2a^2l}{5} + \frac{2ab_3}{3} + \frac{2b_3^2}{3l} \right) \cdot U_7 \right] - \alpha E \pi \left[- \left(\frac{a^2l^2}{20} + \frac{2ab_2l}{15} + \frac{b_2^2}{6} \right) \cdot T_3 + \right. \\
 &\left. + \left(\frac{a^2l^2}{3} + \frac{14ab_2l}{15} + \frac{2b_2^2}{3} \right) \cdot T_4 + \left(\frac{22a^2l^2}{60} + \frac{al(13b_2 - 2b_3)}{15} + \frac{b_2^2 - b_3^2}{2} \right) \cdot T_5 - \left(\frac{a^2l^2}{15} + \frac{2ab_3l}{5} + \frac{2b_3^2}{3} \right) \cdot T_6 + \left(\frac{a^2l^2}{12} + \right. \right. \\
 &\left. \left. + \frac{ab_3l}{5} + \frac{b_3^2}{6} \right) \cdot T_7 \right] = 0;
 \end{aligned} \tag{19}$$

$$\begin{aligned}
 6) \frac{\partial \Pi}{\partial U_6} = 0; &\Rightarrow \frac{E\pi}{2} \left[- \left(\frac{4a^2l}{5} + \frac{8ab_3}{3} + \frac{16b_3^2}{3l} \right) \cdot U_5 + 2 \left(\frac{32a^2l}{15} + \frac{16ab_3}{3} + \frac{16b_3^2}{3l} \right) \cdot U_6 - \left(\frac{52a^2l}{15} + 8ab_3 + \right. \right. \\
 &\left. \left. + \frac{16b_3^2}{3l} \right) \cdot U_7 \right] - \alpha E \pi \left[\left(\frac{a^2l^2}{15} + \frac{4ab_3l}{15} + \frac{2b_3^2}{3} \right) \cdot T_5 - \left(\frac{4a^2l^2}{15} + \frac{8ab_3l}{15} \right) \cdot T_6 - \left(\frac{7a^2l^2}{15} + \frac{16ab_3l}{15} + \frac{2b_3^2}{3} \right) \cdot T_7 \right] = 0; \\
 7) \frac{\partial \Pi}{\partial U_7} = 0; &\Rightarrow \frac{E\pi}{2} \left[\left(\frac{2a^2l}{5} + \frac{2ab_3}{3} + \frac{2b_3^2}{3l} \right) \cdot U_5 - \left(\frac{52a^2l}{15} + 8ab_3 + \frac{16b_3^2}{3l} \right) \cdot U_6 + 2 \left(\frac{23a^2l}{15} + \frac{11ab_3}{3} + \frac{7b_3^2}{3l} \right) \cdot U_7 \right] - \\
 &- \alpha E \pi \left[- \left(\frac{a^2l^2}{20} + \frac{2ab_3l}{15} + \frac{b_3^2}{6} \right) \cdot T_5 + \left(\frac{a^2l^2}{3} + \frac{14ab_3l}{15} + \frac{2b_3^2}{3} \right) \cdot T_6 + \left(\frac{23a^2l^2}{60} + \frac{13ab_3l}{15} + \frac{b_3^2}{2} \right) \cdot T_7 \right] = 0;
 \end{aligned}$$

Solving this system we define values U1, U1,...,U7. Then the field of relocation longwise of each site of the studied rod are defined as follows:

$$\left. \begin{aligned}
 U^{(I)}(x) &= \phi_i(x) \cdot U_1 + \phi_j(x) \cdot U_2 + \phi_k(x) \cdot U_3 \\
 U^{(II)}(x) &= \phi_i(x) \cdot U_3 + \phi_j(x) \cdot U_4 + \phi_k(x) \cdot U_5 \\
 U^{(III)}(x) &= \phi_i(x) \cdot U_5 + \phi_j(x) \cdot U_6 + \phi_k(x) \cdot U_7
 \end{aligned} \right\}, \quad 0 \leq x \leq l \tag{20}$$

$$l=30\text{cm}; \quad a = -\frac{1}{10}; \quad b = 12\text{cm}$$

4. Numerical Results

For approbation of the developed methods and algorithms we will solve the formulated problem at the following input data:

$$\alpha = 0,0000125 \frac{1}{^{\circ}K}; \quad E = 2 \cdot 10^6 \frac{\kappa G}{\text{cm}^2};$$

$$K_{xx} = 100 \frac{\text{Watt}}{\text{cm} \cdot ^{\circ}K}; \quad h = 10 \frac{\text{Watt}}{\text{cm}^2 \cdot ^{\circ}K};$$

$$T_{oc} = 40^{\circ}K; \quad q = -500 \frac{\text{Watt}}{\text{cm}^2};$$

The received decisions are provided on Figures 2-5.

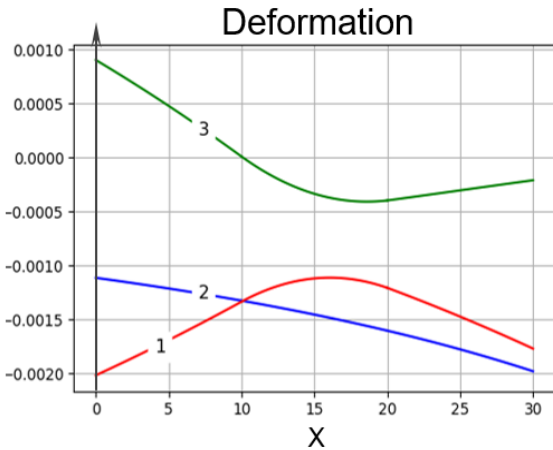


Figure 3. Dependences of deformation the length of the rod

$$1 - \varepsilon(x); 3 - \varepsilon_x(x); 2 - \varepsilon_T(x)$$

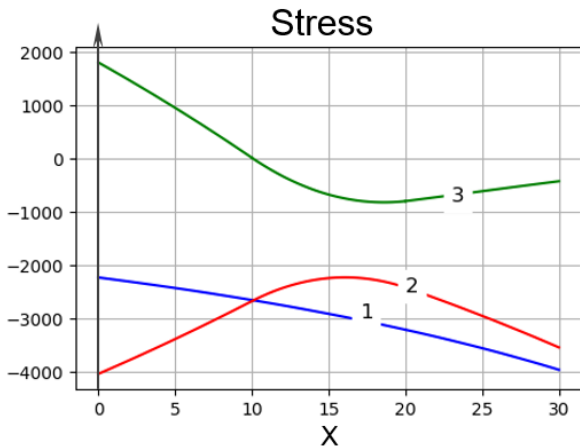


Figure 4. Dependences tension the length of the rod

$$1 - \sigma(x); 3 - \sigma_x(x); 2 - \sigma_T(x)$$

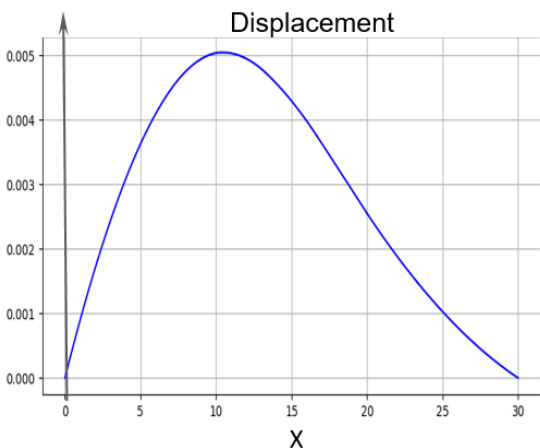


Figure 5. Dependences movement the length of the rod

For this example the sectional area of the left-hand end of a the rod is equal $F(x=0)=144\pi\text{cm}^2$ and right end $F(x=L)=81\pi\text{cm}^2$ it turns out $(x=0)=1,77 \cdot (F(x=L))$; From the Figure 2 it is visible that value of temperature on the left-hand end of $T(x=0)=161.23^\circ\text{K}$, at that time on the right end of $T(x=L)=141.453^\circ\text{K}$. It is caused by the fact that the sectional area of the right end on 1.777 times is less than left-hand. The value of temperature is equal $T(x = \frac{5l}{3}) = 89.08^\circ\text{K}$, in a point $x = \frac{5l}{3}$ it the least in all length of a the rod.

It is caused by the fact that through a lateral area of the site $(l \leq x \leq 2l)$ of a the rod there is a heat exchange to a surrounding medium, and variability of section. From the drawing it is visible that thermoelastic and temperature components of deformation on all length of a the rod have the squeezing character while resilient making character $\varepsilon_x(x)$ on the site $(0 \leq x \leq l)$ of a the rod has stretching, and in other sites the squeezing character. It is caused, the fact that the sectional area of the left-hand end of a the rod is maximal, and there brought a heat flux with intensity $q = -500 \frac{\text{Watt}}{\text{cm}^2}$.

The similar phenomena are observed also in the nature. The distribution law of movement is provided in the Figure 5. Where it is visible from the figure that all sections of a rod except jammed move at the left in the rights. At the same time maximal movements corresponds to section with

coordinate $x = \frac{4l}{3}$. This process is caused with a big sectional area of the left-hand end of a rod and existence of a heat flux constant intensity $q = -500 \frac{\text{Watt}}{\text{cm}^2}$.

Also this phenomenon is promoted by existence of heat exchange through side the surface of the site $(l \leq x \leq 2l)$. After calculation the field of temperatures is defined the size of lengthening of a the rod for a the rod of jamming of one end:

$$\Delta l_T = \int_0^L \alpha \cdot T(x) dx = 0,0432 \text{cm}.$$

In case of jamming of two ends of a rod there is a squeezing axial force which size equally:

$$R = -\frac{E \cdot F_{av} \cdot \Delta l_T}{L} = -1006573,377[kG].$$

5. Conclusion

The method and computing algorithm is developed of fundamental laws of conservation of energy, and also the program on Python allow to solve a class of tasks of definition established thermo - an intense strained state of a the rod of variable section at influence of diverse types of local sources of heat taking into account existence of thermal insulations, physicommechanical and thermal characteristics of material of a the rod, and also at its difficult geometrical sizes.

The received numerical results differ in a high precision and convergence. Besides the offered approach differs in the universality at the solution of relevant engineering tasks stationary thermoelasticities for the rod stock of variable section.

Acknowledgments

This work was supported by the Committee of Science by the Ministry of Education of the Republic of Kazakhstan in the framework of the grant project AP05131093.

References

- [1] G. Grimvall. Thermophysical Properties of Materials 1st Edition. – North Holland 1999. – 424 p.
- [2] Gaspar Jr., Moreira M.L., Desampaio P.A.B. Temperature Distribution Fuel Rods: A study on the Effect of Eccentricity in the Position of UO2 Pellets., 0-th International Conference «Nuclear Energy for New Europe», 2011.
- [3] Heat engineering / Shatrova M.G. M.: Academiya, 2011. – 288 p.
- [4] Timoshenko S., Goodyear J. N. Theory of Elasticity. – McGRAW-Hill. Book. Company. Inc., 1987. – 567 p.